X-ray Emission from a High-Atomic-Number z-Pinch Plasma Created from Compact Wire Arrays

T. W. L. Sanford, T. J. Nash, B. M. Marder, R. B. Spielman, J. F. Seamen,
J. S. McGurn, R. C. Mock, T. L. Gilliland, D. Jobe, and M. Vargas
Sandia National Laboratories, Albuquerque, NM 87185
D. Mosher
Naval Research Laboratory, Washington D. C. 20375
S. Maxon, J. H. Hammer, W. E. Alley, G. B. Zimmerman, J. L. Eddleman,
R. S. Thoe, J. Emig, C. Bruns, J. Hernandez, and P. T. Springer
Lawrence Livermore National Laboratory, Livermore, CA 94550
J. S. De Groot
University of California, Davis, CA 95616
D. R. Welch and K. Struve
Mission Research Corporation, Albuquerque, NM 87106

Abstract

Thermal and nonthermal x-ray emission from the implosion of compact tungsten wire arrays, driven by 5 MA from the Saturn accelerator, are measured and compared with LLNL Radiation-Hydro-Code (RHC) and SNL Hydro-Code (HC) numerical models. Multiple implosions, due to sequential compressions and expansions of the plasma, are inferred from the measured multiple x-radiation bursts. Timing of the multiple implosions and the thermal x-ray spectra measured between 1 and 10 keV are consistent with the RHC simulations. The magnitude of the nonthermal x-ray emission measured from 10 to 100 keV ranges from 0.02 to 0.08% of the total energy radiated and is correlated with bright-spot emission along the z-axis, as observed in earlier Gamble-II single exploding-wire experiments. The similarities of the measured nonthermal spectrum and bright-spot emission with those measured at 0.8 MA on Gamble-II suggest a common production mechanism for this process. A model of electron acceleration across magnetic fields in highly-collisional, high-atomic-number plasmas is developed, which shows the existence of a critical electric field, E_c, below which strong nonthermal electron creation (and the associated nonthermal x rays) do not occur. HC simulations show that significant nonthermal electrons are not expected in this experiment (as observed) because the calculated electric fields are at least one to two orders-of-magnitude below E_c. These negative nonthermal results are confirmed by RHC simulations using a nonthermal model based on a Fokker-Plank analysis. Lastly, the lower production efficiency and the larger, more irregular pinch spots formed in this experiment relative to those measured on Gamble II suggest that implosion geometries are not as efficient as single exploding-wire geometries for warm x-ray production.

Acknowledgments

Contents

Figures

6

8

X-ray Emission from a High-Atomic-Number z-Pinch Plasma Created From Compact Wire Arrays

I. Introduction

The generation of terawatt bursts of warm x rays (10 to 100 keV) are of interest for the study of in-depth material effects induced by nuclear radiation. Pulsed power bremsstrahlung generators with MeV electron-endpoint energies that utilize thin, reflexing converters have the potential of generating such bursts. However, the warm x-ray field is simultaneously accompanied by hard x rays, which mask the effects produced by the lower-energy photons.[1] Accordingly, bremsstrahlung generators are generally used to study hard-radiation effects. At the other end of the spectrum, the plasma radiation source (PRS), a high-atomic-number z-pinch formed from the radial implosion of an annular plasma, provides an excellent source of intense keV-energy x rays.[2] These x rays are generated by thermal processes when the imploding plasma stagnates on the axis of symmetry (z-axis), and its radial kinetic energy is converted into internal energy and radiation. On existing PRS drivers, of which Saturn is the highest-current example,[3] the efficiency of thermal radiation production drops rapidly for photon energies exceeding about 5 keV due to the low masses required for high temperature and the growth of instabilities.[2] The need for a practical, intense radiation source in the 10- to 100-keV regime between existing PRS and bremsstrahlung sources was thus the motivation for the present work.

In the 1970s, high-atomic-number z-discharge plasmas created by discharging 0.8 MA through single wires on the Gamble-II generator demonstrated matched-load behavior,[4] efficient conversion of coupled electrical energy into XUV radiation, about 10%-efficient production of x-ray lines and continuum in the keV-regime,[5-7] and more importantly for the present work, about 0.25%-efficient production of nonthermal, bremsstrahlung-like lines and continuum in the 5- to 100-keV regime.[8] Comparable performance was observed on the similar Physics International Co. Owl-II generator.[9] Experiments with wires of various metals demonstrated an atomic-number scaling of Z^2 for the nonthermal radiation yield. More recently, data from copper plasma annular implosions on Double Eagle at 3 MA and Saturn at 9 MA suggested an I^2 current scaling for the nonthermal K-line radiation yield.[10] These scalings suggest yields of 5- to 100-keV photons well in excess of those expected from the conventional PRS at high current and very-high Z, and motivated this Saturn experiment to measure and model the x-radiation from tungsten z pinches at order-of-magnitude higher currents than Gamble II.

The XUV and thermal keV x rays from the early experiments were in rough agreement with 1D (one dimensional) radiation hydrodynamic calculations,[4] but nonthermal-electron flow was required to explain the warm radiation component. The nonthermal

9

Gamble-II radiation required that about 1/3 of the discharge current be carried in a monotonically-decreasing spectrum of 10- to 100-keV electrons. A variety of other pinch plasmas also exhibit nonthermal x-ray emission.[2,11-14] In all cases, the hard x-ray emission appears to be associated with the formation of tight, x-ray-bright pinch spots. The dynamics of such pinch spots has been widely recognized as a possible source of electric fields that can accelerate electrons to the required nonthermal energies.[4] In the Gamble-II experiments, spots were observed to be strung along the pinch axis, each with dimensions of order 100 μm (the resolution of the camera) or smaller, separated by diffuse flares of plasma with dimensions of order 1 mm or larger. Each spot emitted 2- to 10-ns wide radiation pulses with 3 to 10 such spots emitting at the same time. Averaged over the discharge history, the pinch spots emitted a major portion of the total thermal and nonthermal radiation.

Based on the Gamble-II observations, a nonlinear, 2D theory for pinch spot formation driven by the radiation collapse of a sausage-unstable z-pinch was formulated.[15] This theory provided scaling laws for the generator loading of pinch spots and the associated inductive electric fields produced by their dynamics. The results of this analysis together with 1D and 2D numerical LLNL Radiation-Hydro-Code (RHC)[16] and SNL Hydro-Code (HC)[17] simulations are used in what follows to interpret the measurements of the Saturn experiment in comparison to those of Gamble II. The predicted electric fields from these computations are combined with a model of the collisional, cross-field acceleration of nonthermal electrons to establish if the pinch-spot environment can produce electron energies consistent with x-ray observations. A crucial feature of the modeled cross-field acceleration process is that collisional electron scattering occurs on a shorter time scale than collisional energy loss in high-atomic-number plasmas. Scattering of electrons across the azimuthal self-magnetic field therefore allows electrons to gain higher energies from the electric field than would be experienced in hydrogenic plasmas. Even so, the maximum electric fields predicted from the models and simulations do not produce electrons sufficiently energetic to satisfy nonthermal radiation observations.

The guiding principles of the present experiment were then to:

1. configure the load to resemble the single-wire plasmas of Gamble-II experiments producing maximum nonthermal yield,

2. maintain a low-inductance load geometry to couple efficiently to the Saturn pulse line, and

3. satisfy predicted nonthermal scaling laws to maximize nonthermal production at high current.

In order to achieve (2), a wire array was used instead of single wires. The radius of the wire array was chosen such that implosions occurred early with respect to the time of nominal peak current, enabling the wires to form a sausage-unstable z-pinch so that pinch spots could be well established during the peak portion of the current pulse. For the masses suggested by the assumed nonthermal scaling, a 4-mm-diameter, annular wire array was the lowest-

inductance configuration that satisfied the timing requirement. The small initial annulus radius also insured that a compact pinch, as similar as possible to the Gamble-II single-wire pinches, would form.

The compact-pinch, studied for the first time on Saturn, is different from the conventional PRS and has a number of unique properties. Compared to PRS loads,[2] the Saturn compact pinch has an order-of-magnitude higher mass confined in a region of order-of-magnitude smaller radius and is therefore much denser and brighter. The higher density and correspondingly lower temperature produce x-ray spectra similar to those of single-wire discharges: most of the coupled electrical energy is radiated away below 1 keV. Also similar to single-wire discharges are the appearance of pinch spots along the axis of symmetry of the stagnated plasma and multiple radiation spikes in time. Both of these features are viewed as results of stagnation occurring before the time of peak discharge current. Early pinch formation provides time for instabilities to grow, and the multiple radiation spikes are inferred to be manifestations of multiple "bounces," i.e. compressions and expansions, of the plasma during the current pulse. Such bounces have been inferred previously in low-current neon implosions[18,19] and seen more recently in Al-wire array implosions at high current.[20] Thus, the pinch dynamics have a character between those of the PRS (bounce period > current-pulse duration) and single-wire discharge (bounce period << current-pulse duration).[4] Because of the unusual properties of the compact pinch, studying its dynamics is a secondary objective of the present work.

The experimental arrangement and the data collected are discussed in Section II. In this section, the data are compared with the numerical simulations, giving insight into the characteristics measured and credibility to the simulations. The details of the modeling and simulations important to the experiment are presented in Section III. There, insights into the dynamics and thermal radiation characteristics provided by the simulations are discussed and compared, demonstrating that the MHD (magnetohydrodynamic) characteristics of the measured plasma can be explained. The computations also provide predictions of the electric-field environment that are then compared with those required by nonthermal-electron-production models. As previously mentioned, the magnitude of the observed nonthermal radiation is not explainable by this method. The 2-dimensional arguments used to interpret the pinch-spot structure observed in the experiments are also discussed, along with differences between the Saturn and Gamble-II experiments that may explain their disparity in nonthermal yields. Section IV summarizes the major results.

Appendix I provides details about the fluorescent diagnostic used to measure the nonthermal component, while the other appendices provide details about the various modeling efforts supporting the experiment. Specifically, Appendix II describes the RHC simulations. Appendix III describes the HC fluid computations. And Appendix IV presents descriptions[8] of a fluid model and particle-in-cell (PIC) computations for the production of nonthermal electrons in collisional, high-atomic-number plasmas.

II. EXPERIMENT

A. Arrangement

1. Overview

The experimental arrangement, which uses current from the Saturn accelerator to implode an annular array of wires on the z axis, is shown in Fig. 1. In Saturn, a Lucite insulator stack at 1-m radius (Fig. 1A) separates the vacuum section from the water and oil sections containing the Marx generator, intermediate store, and pulse forming lines. At the stack, current is simultaneously fed into four parallel MITLs (magnetically-insulated transmission lines). The current from each MITL is added in an 8-post-hole convolute (Fig. 1B) and injected into a radial feed that delivers the summed current to the imploding load (Fig. 1C). Outside the load region, diagnostics are positioned in three vacuum line-of-sights at 35° with respect to the horizontal (Fig. 1D). Saturn is a low-impedance, low-inductance accelerator. As such, its vacuum-water interface is prone to flashover due to the large inductive voltage generated when the generator drives a high-inductance load such as a single wire mounted on axis.[17] To avoid this limitation, the rapid implosion of compact wire arrays was used in the present Saturn experiment instead of a single exploding wire on axis (as in the Gamble-II experiments). In this arrangement, the initial inductance of the wire array is kept low, preventing insulator flashover during the rise of the driving current pulse. The load comprised a 4-mm-diameter annular array of 2-cm-long wires (typically 20 in number) uniformly spaced in azimuth about the z axis (Fig. 1C). Eight current-return posts surrounded the load, enabling the radiation generated by the imploded-wire array to pass through and to be monitored.

2. Load

The parameter E/n represents a natural parameter to characterize conditions in the plasma conducive to nonthermal electron production (see Sec. IIIC), where E is the electric field and n is the ion density. Across a pinch spot, E/n is proportional to $I/\tau(m/\ell)$, where I is the total current flowing through the plasma load, τ is the dynamic time scale for pinch-spot collapse,[15] and m/ℓ is the mass per unit length of the load. The I/τ scaling assumes that the electric field is inductive in nature (concern about the inductive field assumption is discussed in Sec. III). The early Gamble-II data[8] for tungsten wire loads suggested that the conditions for maximizing nonthermal electron production and associated nonthermal radiation corresponded to a $I/(m/\ell)$ value of about 2 MA/(mg/cm). Assuming that for comparable pinch sizes and current pulse durations on Gamble II and Saturn that τ is also comparable, then for Saturn conditions (I > 4 MA, ℓ = 2 cm), this scaling suggested a mass in the neighborhood of 4 mg. In the Saturn experiment, the mass of the tungsten loads used was varied in factor-of-two steps from 1 to 16 mg. Additionally, the Gamble-II data showed a strong Z dependence of the nonthermal radiation. This dependence was checked by imploding 4-mg copper and aluminum arrays in addition to tungsten.

A.

C.

B.

D.
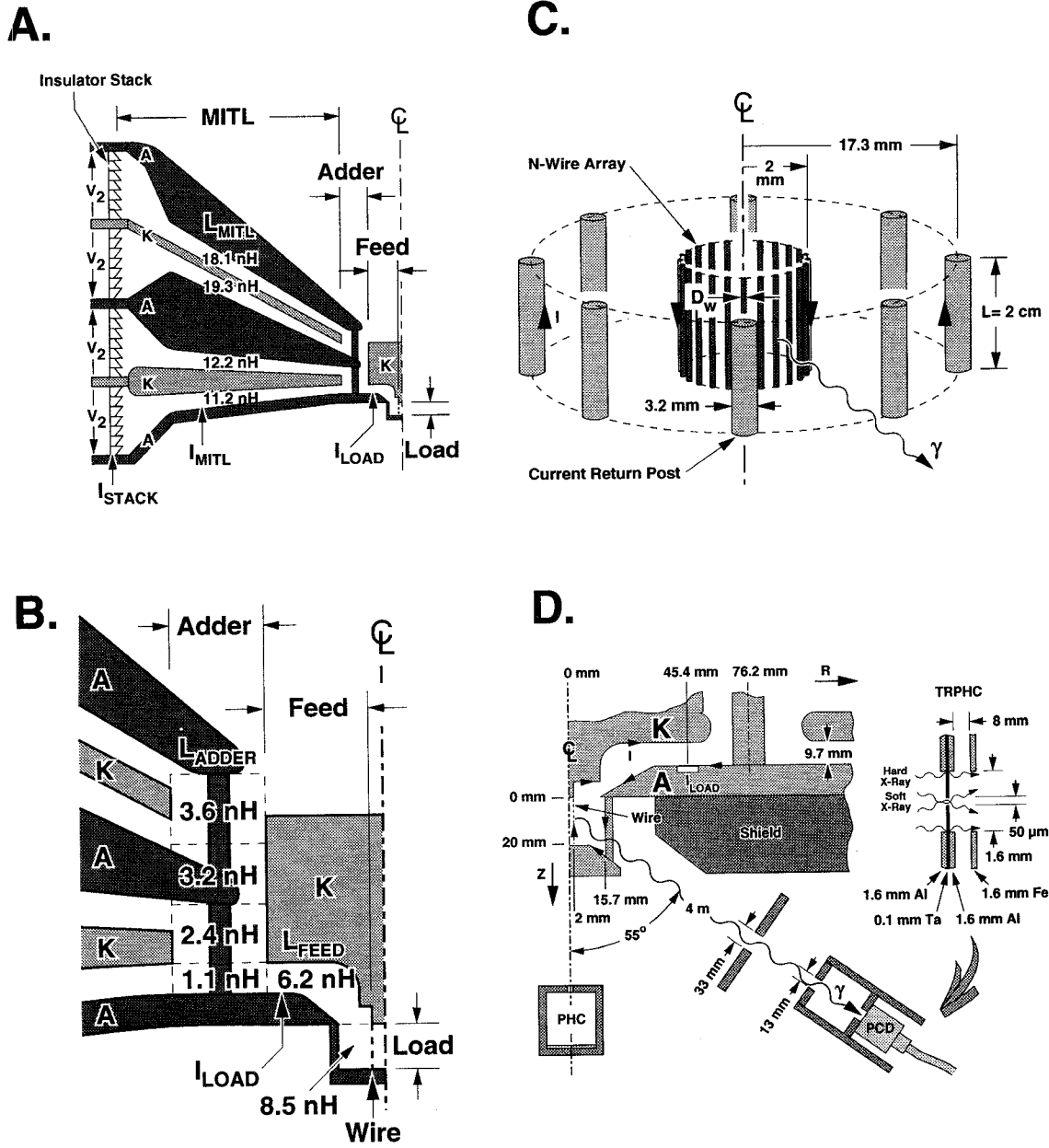
Figure 1A. Saturn configuration showing location of the current diagnostics I_{STACK}, I_{MITL}, I_{LOAD} with respect to the insulator stack, MITLs, Adder, Feed, and Load sections.

Figure 1B. Detail of Adder and Feed sections.

Figure 1C. Detail of Load section showing position of compact cathode wire array with respect to the eight anode current return posts.

Figure 1D. Experimental arrangement showing location of the radiation diagnostics with respect to the load section. PHC, PCD, and TRPHC refer to the time-integrated pinhole camera, photoconducting diode, and time-resolved pinhole camera, respectively.

The radius of the wire array was chosen such that implosions occurred early with respect to the time of nominal peak current, enabling the wires to form a z-pinch and permitting the sausage instability and associated pinch spots to be well established during the peak portion of the current pulse. For the above range of masses suggested by the $I/(m/\ell)$ scaling, a 4-mm-diameter array satisfied the timing requirement. Additionally, the small initial radius insured that a compact pinch, comparable to the Gamble-II single-wire pinches would form even with modest implosion compression ratios. It is important to note that the masses (radii) of these load configurations are higher (smaller) than those employed in conventional imploded plasma radiation sources designed to efficiently excite thermal K-line radiation.[2]

3. Current Diagnostics

Six B-dot monitors measured current in the lower MITL adjacent the insulator stack (I_{MITL} in Fig. 1A), and two B-dot monitors measured the total current in the radial feed adjacent the load (I_{LOAD} in Fig. 1A and 1D). The monitors were bench calibrated and intercalibrated with piezoelectric stress gauges to an accuracy of 5%, using low-inductance argon-gas-puff loads where current losses in the MITLs were negligible. The intercalibration permitted the total current near the insulator stack to be inferred from the MITL monitors.

Comparison showed a significant current loss between the two monitoring positions (Fig 2A). A SCREAMER model[21] of the current flow through the accelerator from the Marx generator to the imploding load is in agreement with this observation (Fig 2A). In SCREAMER, both MITL current loss and the effect of the increasing inductance of the imploding load are included. Space-charge-limited MITL losses occur in SCREAMER when the local cathode electric field exceeds 50 kV/cm and are turned off when the local magnetic field exceeds the magnetic insulation criterion, that is, when an electron cyclotron radius becomes smaller than the interelectrode gap. In SCREAMER, the z-pinch load is modeled as a magnetically-driven, radially-imploding annulus, which compresses to a fixed radius of $1/10^{th}$ its initial value. The currents calculated after this model-transition time are therefore only indicative of those actually flowing. The load B-dot monitors often flash near their peak values, yielding measurements that are similarly unreliable after this time. Thus, the disagreements between calculations and measurements shown in Fig. 2A at late times are not meaningful. The monitors therefore provide only an estimate of the current flowing prior to the first implosion providing that loses between the monitor and load are modest. For 4 mg loads, $I_{MITL} = 6.0 \pm 0.3$ MA and $I_{LOAD} = 4.8 \pm 0.5$ MA (where the uncertainties refer to the RMS shot-to-shot variation), which bound the calculated value of 5.1 MA.

During the rise of the current pulse, voltages across the MITL gaps reach MV levels and in particular, near the time of stagnation where the L-dot loading is high, high voltages are developed in the region of the load (Fig. 2B). These high voltages combined with electron current loss lead to the generation of hard bremsstrahlung x-radiation. This radiation represents a significant background to load radiation detectors. The dashed line in Fig. 2C shows this hard radiation background as measured by an open-ended cable and is compared

14
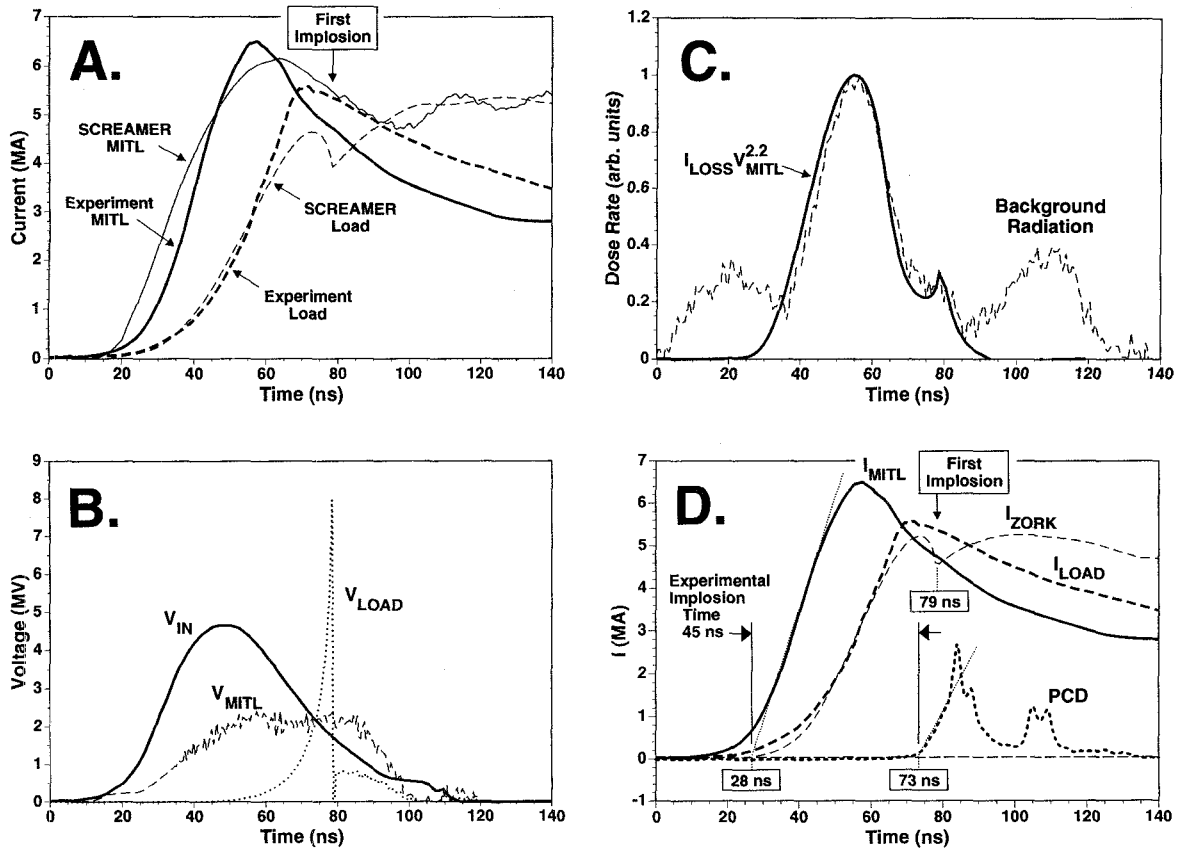
Figure 2A. Comparison of measured currents at I_{MITL} and I_{LOAD} (Figure 1A) with that modeled by SCREAMER for a 4-mg load.

Figure 2B. Comparison of voltages V_{MITL} and V_{LOAD} calculated at I_{MITL} in the MITL and across the wire load (Figure 1D) by SCREAMER, for a 4-mg load. Shown also is the input voltage, V_{IN}, used in the ZORK model of Figure 3 and discussed in Section II.A.4.

Figure 2C. Comparison of the radiation induced background in a disconnected PCD cable with that calculated by SCREAMER using the simulated current loss, I_{LOSS}, in the MITL (Fig. 2A) and MITL voltage, V_{MITL} (Fig. 2B).

Figure 2D. Comparison of the measured current at the load, I_{LOAD}, with that simulated by ZORK, I_{ZORK}, using V_{IN} of Figure 2B and the circuit model of Figure 3 for a 4-mg load. Shown also is a graphical description that defines the experimental (73 - 28 = 45 ns) and theoretical (79 - 28 = 51 ns) implosion time. Here PCD corresponds to the photoconducting detector whose response is centered at 1.4 keV (Table I).

15

with a SCREAMER prediction (solid line). The temporal characteristic of this background[22] is expected to scale as the electron loss current I_{LOSS} times $V_{MITL}^{2.2}$. The background signal observed during the rising portion of the injected current is in excellent agreement with this expectation using SCREAMER to calculate I_{LOSS} and V_{MITL}, giving credibility to both the current measurements and the associated SCREAMER simulations. Observed also in the background measurements are smaller signals before and after the bremsstrahlung, suggesting that additional current loss is occurring in other parts of the current path. Bremsstrahlung pickup was minimized by adding shielding near the load, below the lower MITL, around detectors, and by collimating to record only radiation coming directly from the load (Fig. 1D).

4. Equivalent Circuit Model

Measurements and SCREAMER analyses show that these Saturn experiments can be described by the simpler equivalent circuit model of Fig. 3, which is easily implemented as input to the RHC and HC modeling discussed later. Here the accelerator up to the insulator stack is replaced by the voltage source V_{IN} shown in Fig. 2B in series with a 1/6-Ohm resistor and a 0.75-nH inductor. In the vacuum section, the four parallel MITLs and adder (L_2 in Fig. 3) are equivalent to 6 nH, with the remaining radial feeds to the wire array adding 14.7 nH (L_3 and L_4 in Fig. 3). Figure 2D shows that the load current I_{ZORK} calculated with this circuit model using the revised ZORK code[17,23] (which includes the motion of the load assuming a slug implosion) is in reasonable agreement with that measured up to implosion time. ZORK load modeling does not include internal plasma degrees of freedom and therefore cannot model the load at later times. It is this circuit model up to the load region that is used as input to the more complete RHC and HC load simulations discussed in Section III. These models agree with the radius vs. time prediction of ZORK up to the implosion time.[17]

The interval between the leading edge of the MITL current (which is well defined) and the 1.4-keV radiation signal, as shown in Fig. 2D determines the experimental implosion time. This implosion time as a function of the load mass (Fig. 4) is in agreement with ZORK calculations for masses less than 8 mg. The agreement provides confirmation that the bulk of the measured load current is flowing through the load and gives additional credibility to the circuit model. If the bulk of the measured load current were not flowing in the load, the measured implosion times would be longer than those calculated for the full mass participating in the implosion (see Sec. IIIB).

5. Radiation Diagnostics

The temporal and spatial characteristics of the radiation were sampled by detectors 35° below the horizontal plane in vacuum lines of sight (Fig. 1D). Because of this angle, each diagnostic viewed 1.5 cm of the 2-cm plasma length. A nickel bolometer, filtered diamond photoconducting detectors (PCDs),[24] and a filtered fluorescer array (FFA) (see Appendix I) measured the radiation history in broad photon-energy bins ranging from 0 to

16

A.

L_2

L_{MITL}

Z
0.167
Ω

L_1
0.75
nH

V_1 V_2

18.1
nH

19.3
nH   3.6 nH

12.2
nH   3.2 nH

11.2
nH   2.4 nH

L_{ADDER}

1.1 nH

V_{IN}

L_{FEED}

V_3

L_3
6.2 nH L_4
8.5 nH

V_4

L_{PLASMA} L_{LOAD}

Oil / Water
Section   Vacuum
Section

Insulator Stack

B.

Z
0.167
Ω

L_1
0.75
nH

L_2
6.0
nH

L_3
6.2
nH

V_1 V_2 V_3

L_4
8.5 nH

V_{IN}

Oil / Water
Section   Vacuum
Section

V_4

L_{PLASMA} L_{LOAD}

Insulator Stack
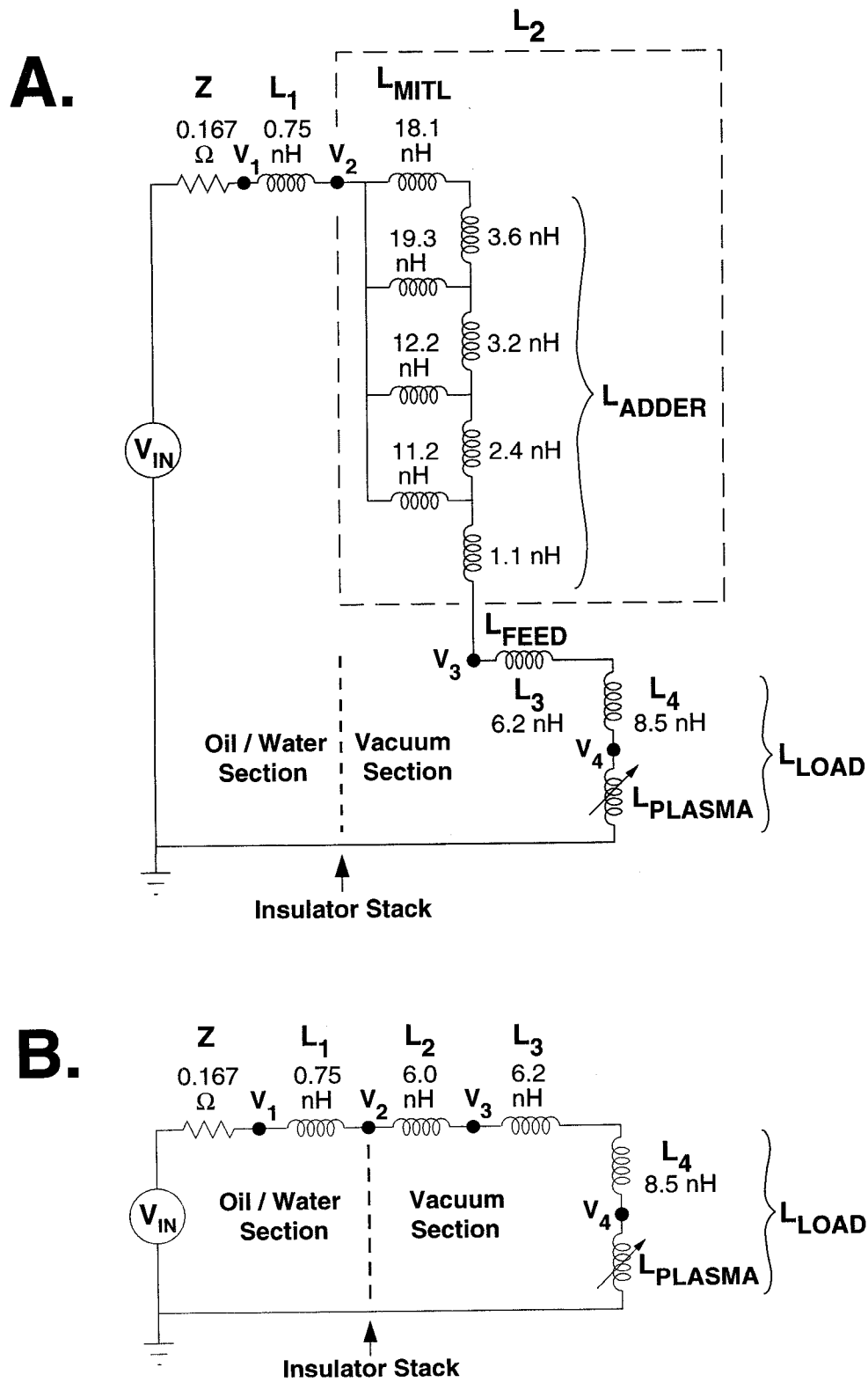
Figure 3. (A) Detailed circuit corresponding to the geometry of Figure 1A and (B) equivalent circuit used in the ZORK, RHC, and HC models.

17
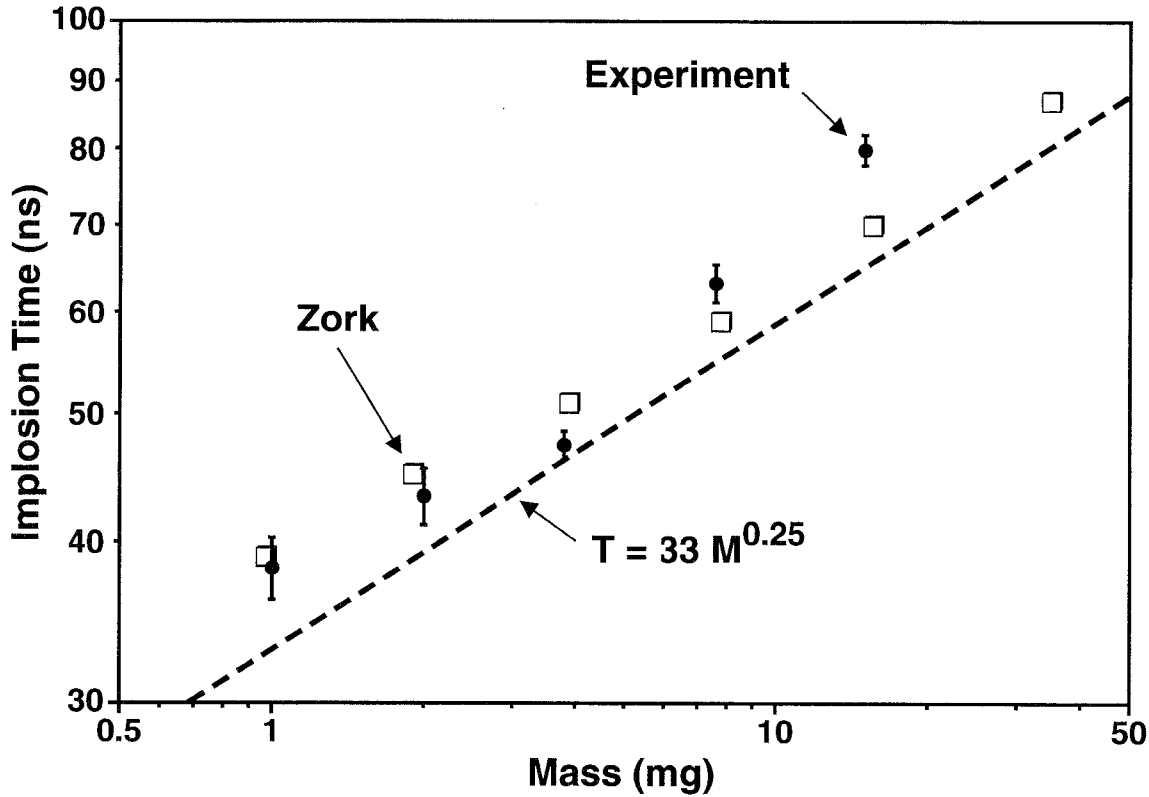
Figure 4. Comparison of measured implosion time with that calculated by the ZORK model as a function of the load mass.

~ 350 keV (Table I). The bolometer was calibrated to an accuracy of 10% , the PCDs were intercalibrated using the Brookhaven National Laboratory synchrotron to an absolute accuracy of 20% and to a relative accuracy of 5%, and the FFA calibration was established to an absolute accuracy of 50% with relative channel-to-channel accuracy of 30% using LLNL's High Energy X-ray Calibration facility. A fast-framing x-ray pinhole camera[25] recorded the spatial distribution of the radiation generated in two energy bands (1-4 and 4-10 keV) in five 3-ns time intervals with a 5-ns inner frame spacing. A KAP crystal spectrometer measured the time-integrated x-ray spectrum over the range of 0.8 to 3 keV with 1-eV resolution. Owing to the broad band response and the uncertainty in inferring the spectra with these detectors, the uncertainty in extracting the measured radiation yield from a given PCD or FFA is estimated to be a factor of two.

Table I

List of radiation diagnostics used and their associated sensitivity range. The "center" and "limits" refer to the x-ray energies associated with the peak and about 50% of peak responses of the given detector to the measured spectrum of Fig. 18. "Width" refers to the bin width of the x-ray energy used to convert the energy measured in the given detector to units of J/keV. **BOLO, PCD, FF**, and **ROSS** refer to nickel bolometer, filtered diamond photo conducting detector, filtered fluorescer, and ROSS filter pair, respectively.

| Diagnostic | Filter/Fluorescer | Sensitive Range | | | |
		Lower Limit keV	Center keV	Upper Limit keV	Width keV
BOLO	None	0	~0.4	≤1	0.8
PCD	8-mm Be	0.7	1.0	1.6	0.9
PCD	8-mm Kapton	1.0	1.4	2.1	1.1
PCD	254-mm Kapton	3.2	4.5	6.6	3.4
ROSS	25-mm Fe; 81-mm Ti	5	6.1	7	2.0
PCD	25-mm Ge	5	6.2	9	4.0
FF [**]	38-mm Cu/76-mm Cu[†]	9.5	11.5	14	4.5
FF [**]	— / 76-mm Cu[†]	5	~15*	23	8
FF [**]	51-mm Mo/25-mm Mo[††]	22	29	36	14
ROSS	152-mm Au; 1-mm Ag	50	65	80	30
PCD	1-mm Ag	~ 90	~ 140	~ 300	310

*   Double valued
** 250.4-mm Mylar (vacuum window) prefilter
†   7.6-mm polypropylene post filter
†† 105-mm polypropylene post filter

B. Data

1. Temporal Structure

The temporal responses of the PCDs and FFA in various photon-energy bins for a typical 4-mg tungsten implosion (Shot 1864) are shown in Fig. 5. The radiation from the load is superimposed on a background arising from high-energy bremsstrahlung picked up by the monitors and associated cables. Figure 5J illustrates the shape of this background as measured using an open-ended cable in proximity to the high-energy detectors. The intensity of the radiation shows a multiple-peak characteristic occurring simultaneously in all detectors, as illustrated by the A, B, C peak regions shown in Fig. 5. The period between peaks grows from about 10 ns to about 40 ns as the mass is increased from 1 to 8 mg (Figs. 6 and 7). The
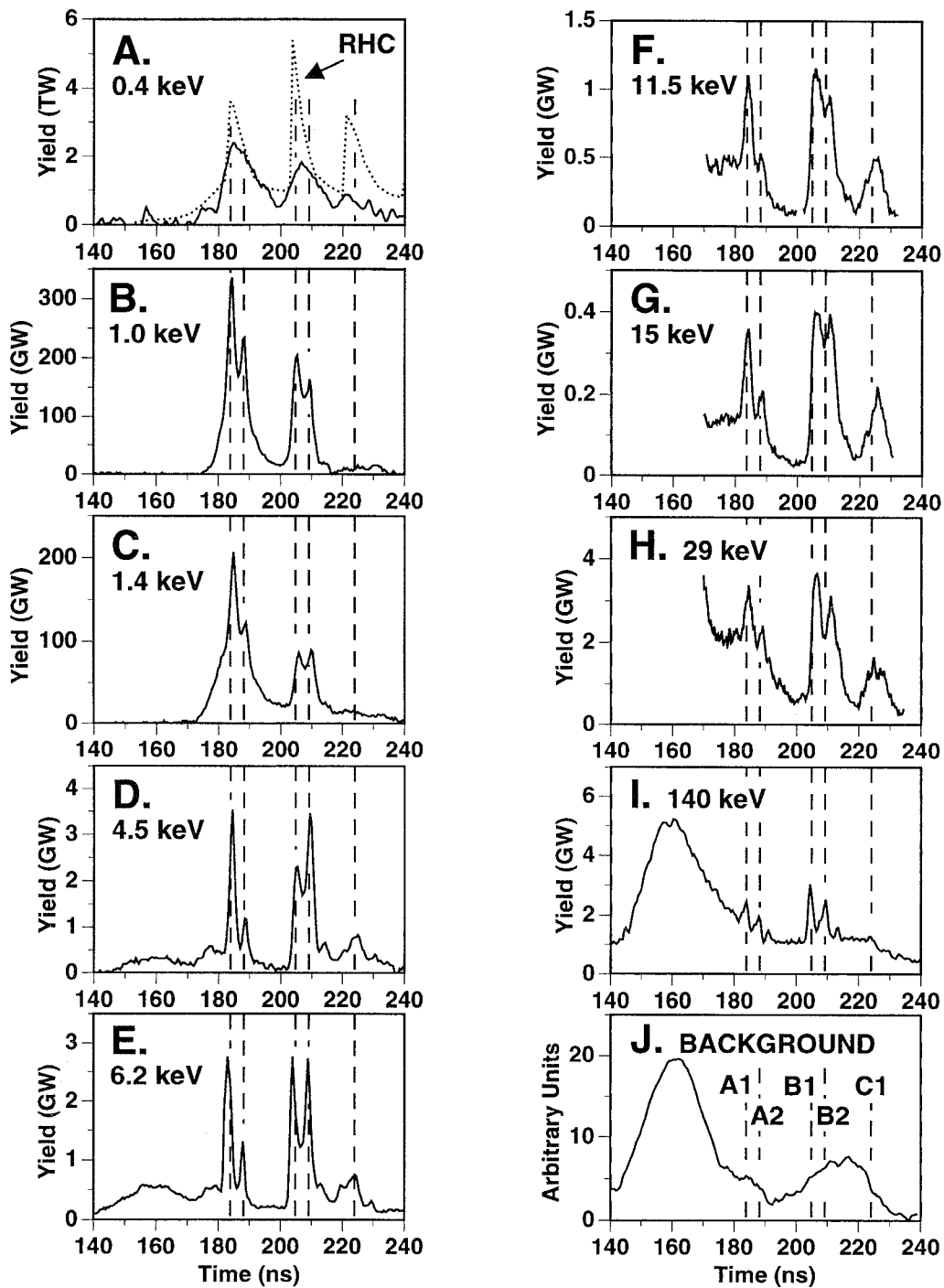
Figure 5. Comparison of the radiation measured for a 4-mg tungsten load (shot 1864) as a function of the energy response of the given detector listed in the upper left-hand corner of each figure (except J). (A) corresponds to that measured in the bolometer; (B) through (E) and (I) correspond to that measured in the PCDs; (F) through (H) correspond to that measured in the FFA; and (J) corresponds to the background measured in a disconnected PCD cable (see Table I). Shown also in (A) is the total radiation yield calculated by 1D-RHC.
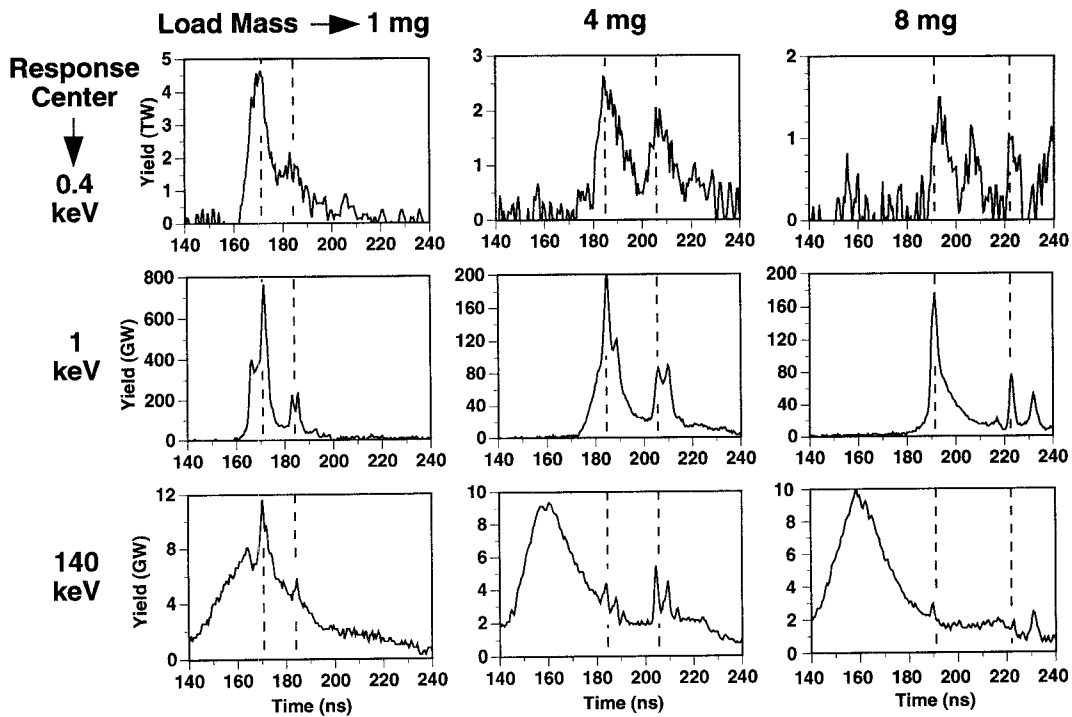
Figure 6. Comparison of the radiation measured in the bolometer (0.4 keV), the 1-keV PCD, and the 140-keV PCD (see Table I) as a function of the mass, m, of the tungsten load shots, where m = 1, m = 4, and m = 8 mg.
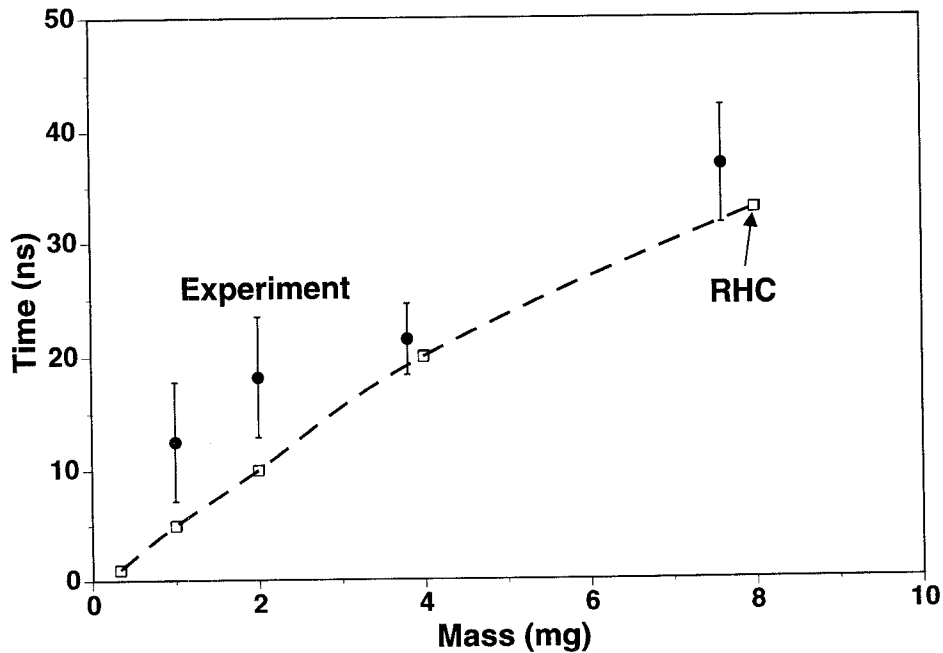
Figure 7. Comparison of the measured time between the first and second implosions (major radiation bursts as shown by the dashed lines in Figure 6) with that calculated by 1D-RHC as a function of the mass of the tungsten load.

multiple-peak behavior is interpreted as a series of oscillations of plasma radius predicted by RHC and HC simulations of the load dynamics (Fig. 6 and 7 and Sec. III). These and other analyses[26] predict that the plasma "bounces" back out to large radius following the initial implosion and stagnation. Conversion of kinetic energy to thermal energy causes the kinetic pressure to exceed the magnetic pressure at peak compression so that the plasma expands against, and does work on, the magnetic field. As the plasma expands and cools, magnetic pressure again exceeds the kinetic pressure and the plasma is recompressed. In contrast to usual PRS loads, the high-mass tungsten pinches should be optically thicker, so that less of the thermal energy that drives the bounce motion is radiated away. The process continues until either the driving current pulse decays and the pinch disperses, or excess internal energy is radiated away and an equilibrium pinch is established. In practice, other processes, such as breakdown in the MITLs and the insulator stack following the initial implosion may speed termination of the oscillations.

Observation of multiple peaks in imploding annular radiation sources is a unique feature of the present experiment. Typical wire-array and gas-puff loads have larger initial radius, lower mass, and implosion times occurring later in the current pulse in order to maximize thermal excitation of K-line radiation.[2] Under such conditions, the radial bounce time (see Section III) is comparable to the current-pulse duration, and additional implosions are unlikely. Additionally, the higher plasma temperatures of conventional plasma radiation sources promote faster instability growth so that instabilities may disrupt the pinch on the bounce time scale.

For 4-mg loads (Fig. 8), three to four oscillations are clearly observed in the radiation traces with the period between the radiation bursts being in agreement with that seen in the 1D-RHC simulations (Figs. 5A and 7). The agreement with analysis of this measured periodicity and that measured for different masses (Fig. 7) suggest that the current continues to flow through the plasma following the first implosion (see Sec. IIIB). The time variation of load inductance produced by the oscillating plasma radius should produce corresponding oscillations in load current. This oscillation, if present, is not observed in the measured currents (Fig. 2A) due to monitor flashover near the time of the first implosion where inductive voltage drops (Fig. 2B) and electron losses become high.

2. Variation with Atomic Number

The radiation emitted by Al and Cu plasmas at 4 mg shows a similar oscillatory pattern to that measured for W in all but the highest two energy channels (Fig. 9). Figure 10 summarizes the emission in various photon-energy bins as a function of atomic number for 4-mg implosions. Total radiation results (divided by the 0.8-keV experimental bin width used for the bolometer data [Table I]) predicted by 1D-RHC simulations are shown for comparison. Emissions in the sub-keV regime for the three atomic number plasmas are comparable because the bulk of the implosion energy (comparable for the three cases) is expected to be efficiently radiated away at the low photon energy regime.[27] Emission of keV-level photons is observed to be higher for aluminum. This behavior is also expected due to thermal excitation of aluminum K-lines and associated recombination radiation. At the
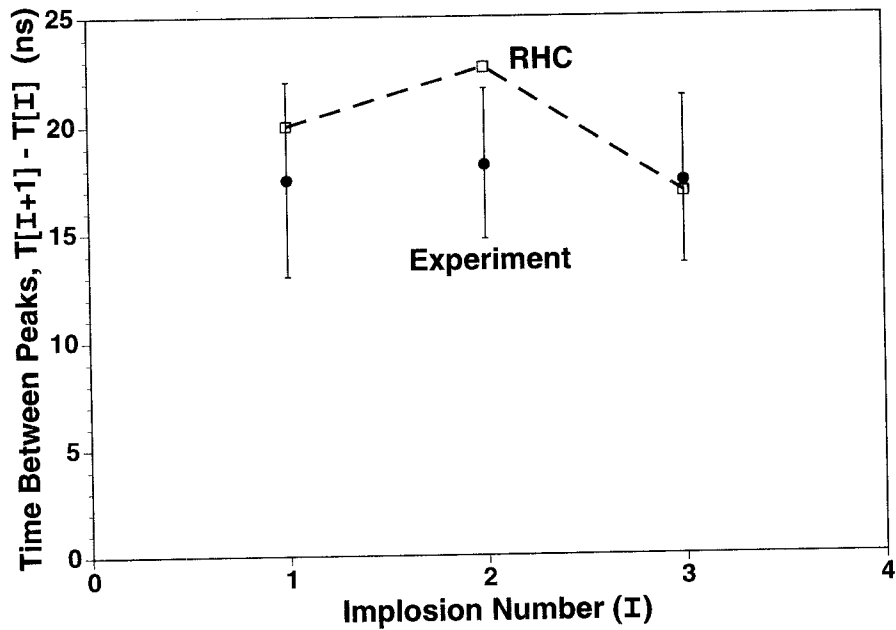
Figure 8. Comparison of the measured time, T(I+1) - T(I), between implosions (major radiation bursts), I, and I+1 with that calculated by 1D-RHC as a function of implosion number, I, for the 4-mg tungsten load shots.
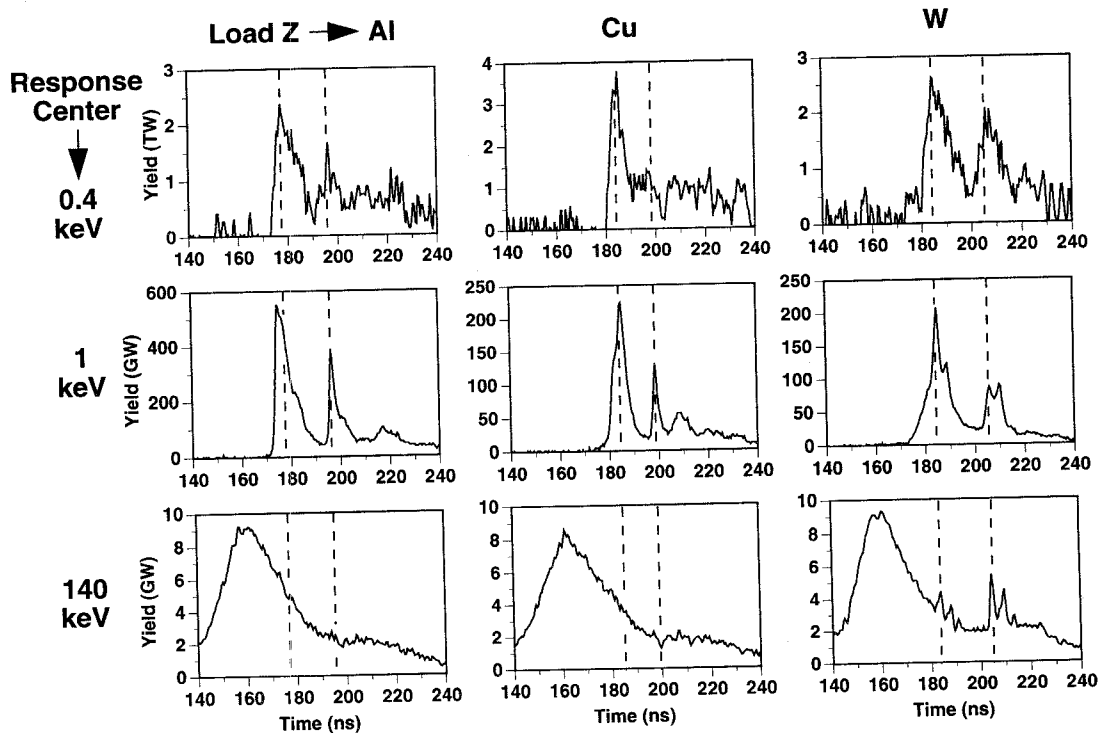
Figure 9. Comparison of the radiation measured in the bolometer (0.4 keV), and 1-keV PCD, and the 140 keV PCD (see Table I) as a function of the atomic number of the 4-mg load shots for Al, Cu, and W.
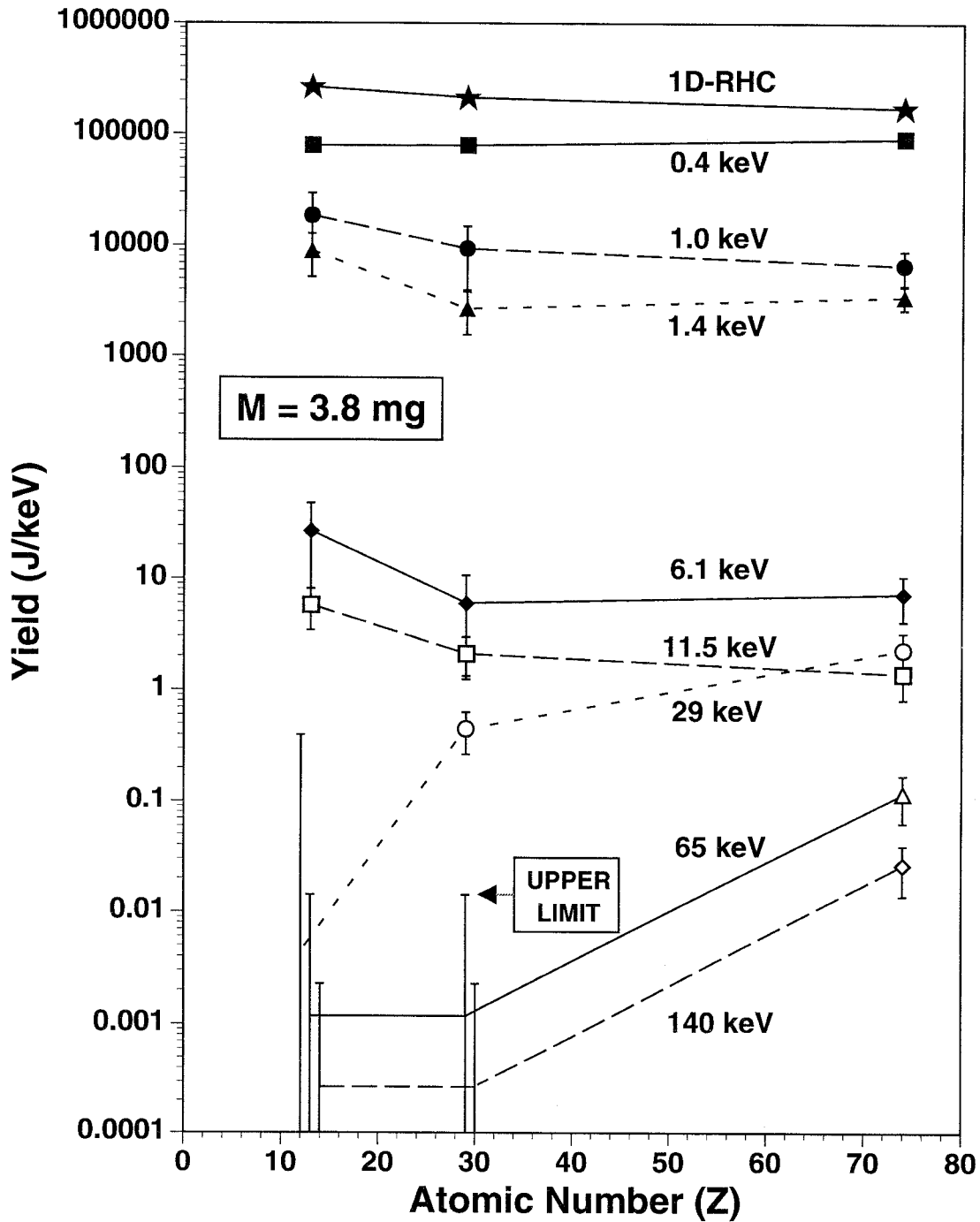
Figure 10. Comparison of the radiation yield measured in J/keV as a function of detector response (noted by the photon energy adjacent each plot on the right) and atomic number of load. The 0.4 keV, 1 keV and 140 keV plots correspond to the data of Figure 9. The load mass was 4 mg. The data for the 65 keV and 140 keV plots for the Al and Cu loads correspond to upper limits only. Shown also is the 1D-RHC total yield normalized by 0.8 keV, which corresponds to the same response width used to normalize the 0.4-keV bolometer data. The bolometer is sensitive to the total yield (see Table I) to within 5%.

highest photon energies, much lower radiation yields are measured for Al and Cu loads, suggesting that high-energy x rays arise from nonthermal processes for which the yield was observed[8] to scale like Z^2. In particular, no signal above background was measured for the Al and Cu loads in the 65 and 140-keV channels. The values shown for these two channels represent upper limits to that which could be observed were a signal to be present.

3. Variation with Mass

For all shots, the first implosion radiated the most power, but not in the highest energy band. The variation of peak total x-ray power with implosion number is shown in Fig. 11 averaged over the 4-mg W loads. The ratio of the peak total x-ray power at the first implosion to that at the second implosion decreases with increasing mass (Fig. 12A). This ratio is greater than unity for all masses, while that calculated by RHC is so only for the lowest-mass implosions. For the hardest radiation channel, the peak power at the second implosion is greater than at the first for all but the lowest mass tested (Fig. 12B).

The energy radiated in the various photon-energy bins as a function of mass is shown in Fig. 13. The trend of increased emission with decreasing mass is reflected by the 1D-RHC simulations, though the total predicted yields are substantially higher than those measured. This discrepancy is consistent with the idealized nature of the simulations, producing larger radial convergence over the full length of the pinch.

The observed decreased peak power and increased duration between radiation pulses with increased mass (Fig. 6) is expected from simple arguments (see Sec. IIIB). As the mass increases, the implosion velocity decreases resulting in increased implosion times and lower plasma temperatures at stagnation. Because the bounce time scales with the implosion time and the implosion time increases with mass, longer durations between turn around in the implosion/explosion process and subsequently lower radiation rates are expected. The total radiation yield, however, peaks near ~ 2 mg (Fig. 13). 1D-RHC shows that this maximum (1.5 mg in RHC [Fig. 13]) is the result of two competing factors. First, as the mass decreases the number of compact, high-temperature implosions that generate the bulk of the radiation increases. Second, however, at very low mass the increased frequency of the radial oscillations combined with the limiting excursions of the oscillations (owing to the decreased internal pressure generated for lower masses) leads to high load inductances with lower driving current and reduced radiation output. Within the large shot-to-shot variation, the yields measured in the higher-energy channels follow the trend measured for the total radiation yield with mass (Fig. 13).

4. Spatial Structure

The fast-framing x-ray pinhole camera (FFC), which is sensitive to 1- to 4-keV x rays was gated to capture five frames in two x-ray energy bins spanning a 20-ns interval after the onset of the first implosion. These data show that near the time of the first implosion, radiation emission in this 3-keV-wide channel is primarily from bright spots formed along the z axis. This correlation is illustrated in Figs. 14 and 15 for the same 4-mg load. The
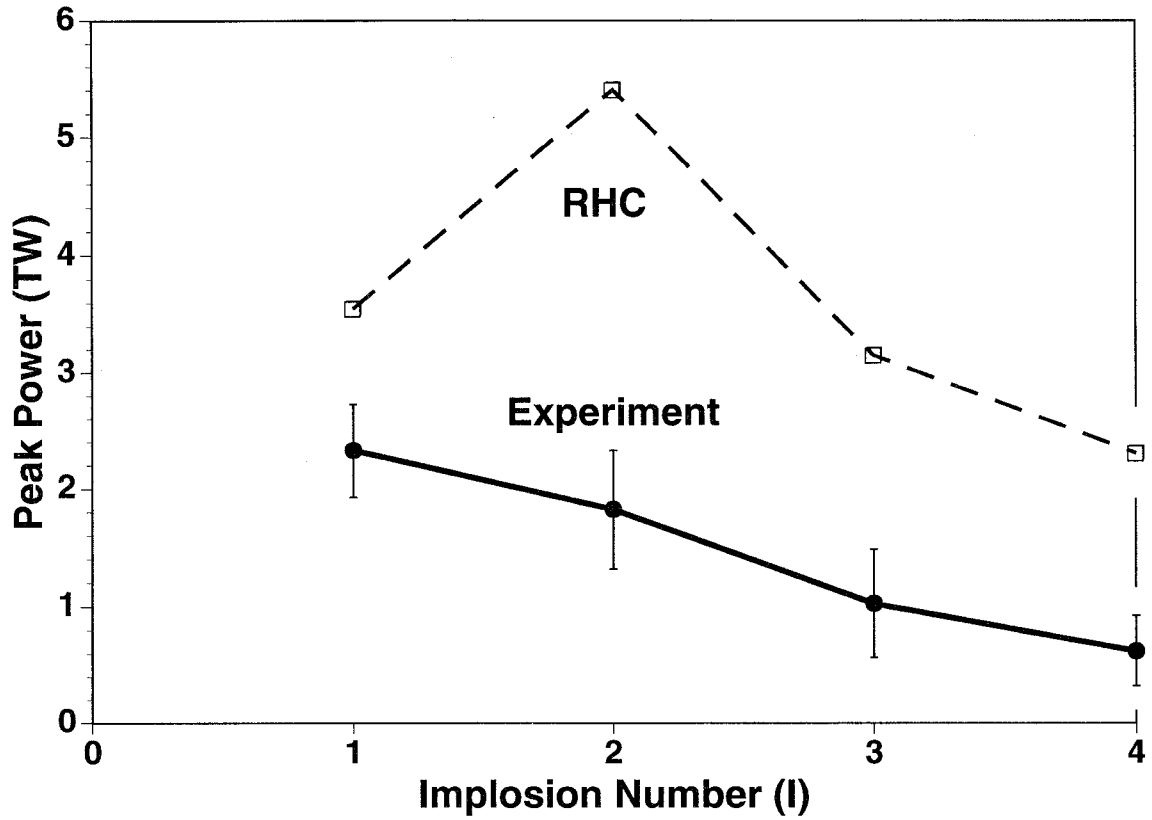
Figure 11. Comparison of the average peak power measured in the bolometer with that calculated by 1D-RHC as a function of the implosion number, I, for all 4-mg tungsten load shots.
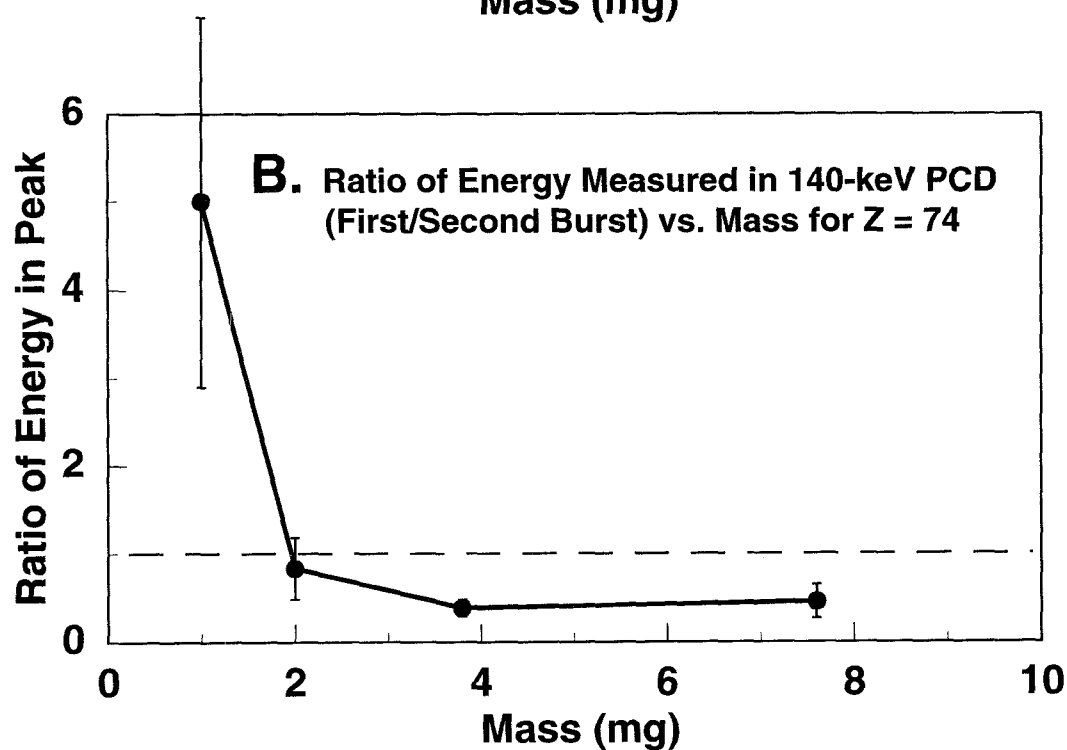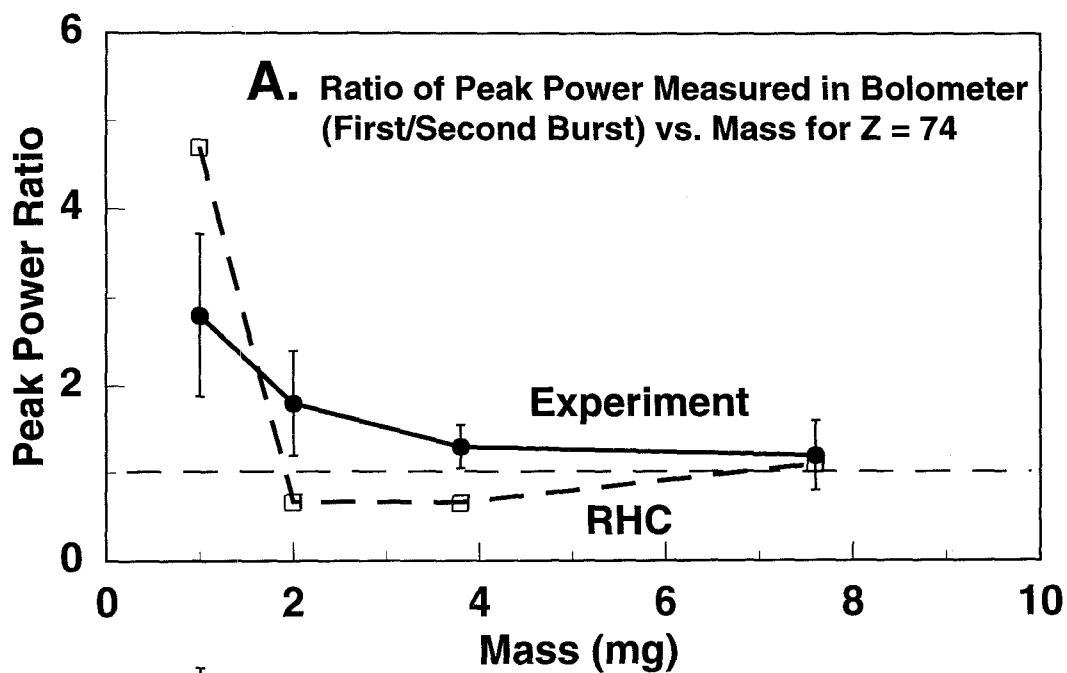
Figure 12A. Comparison of the ratio of the peak power measured at the first implosion relative to that measured at its second implosion (by the bolometer) with that calculated by 1D-RHC as a function of mass for the tungsten load shots.

Figure 12B. Plot of the ratio of the energy measured from the first implosion relative to that measured from the second implosion (by the 140-keV PCD) as a function of mass for the tungsten load shots.
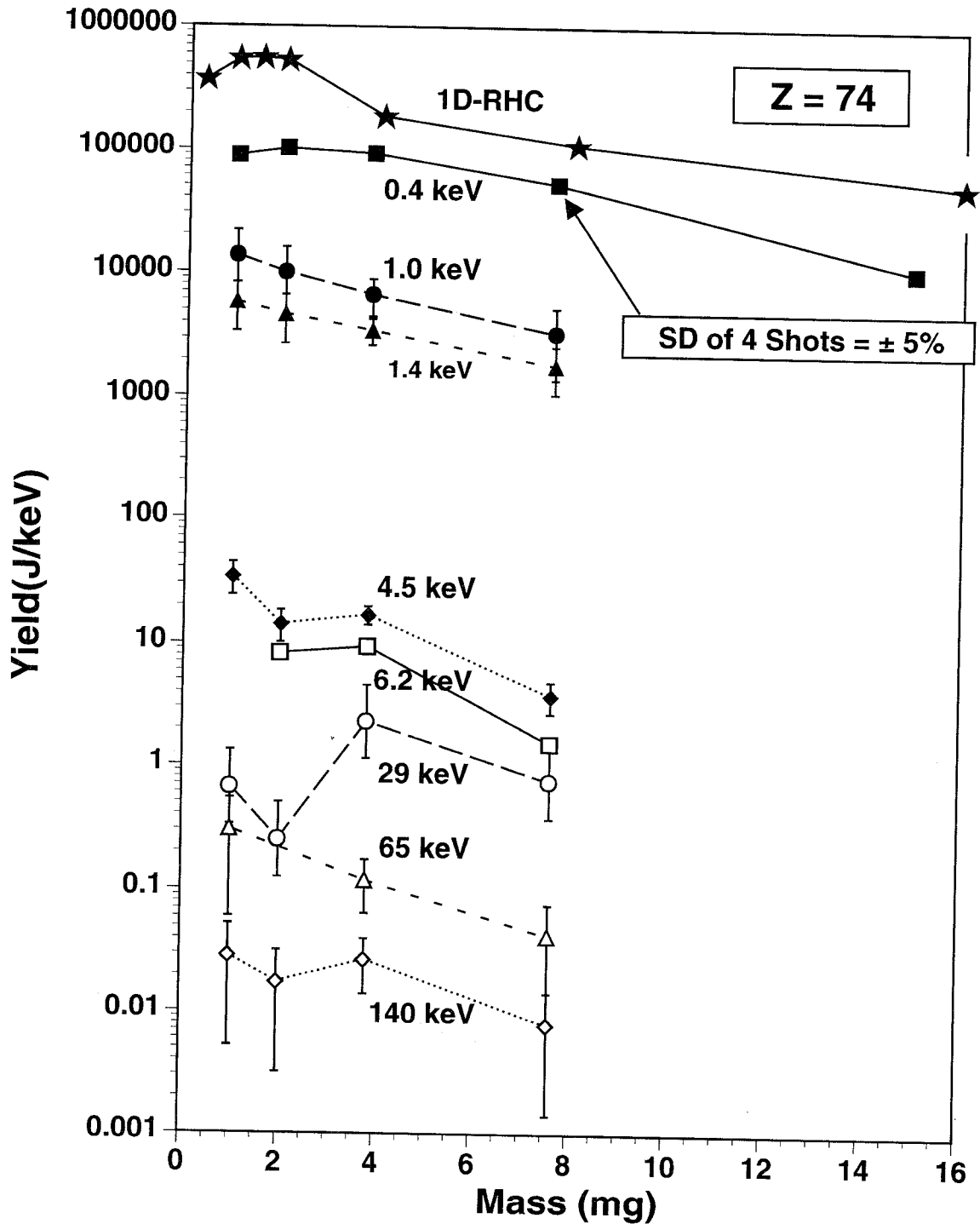
Figure 13. Comparison of the radiation yield measured in J/keV as a function of detector response (noted by the photon energy adjacent each plot) and load mass for tungsten loads. Shown also is the 1D-RHC total yield normalized by 0.8 keV, which corresponds to the same response width used to normalize the 0.4-keV bolometer data, which is within 5% sensitive to the total yield.
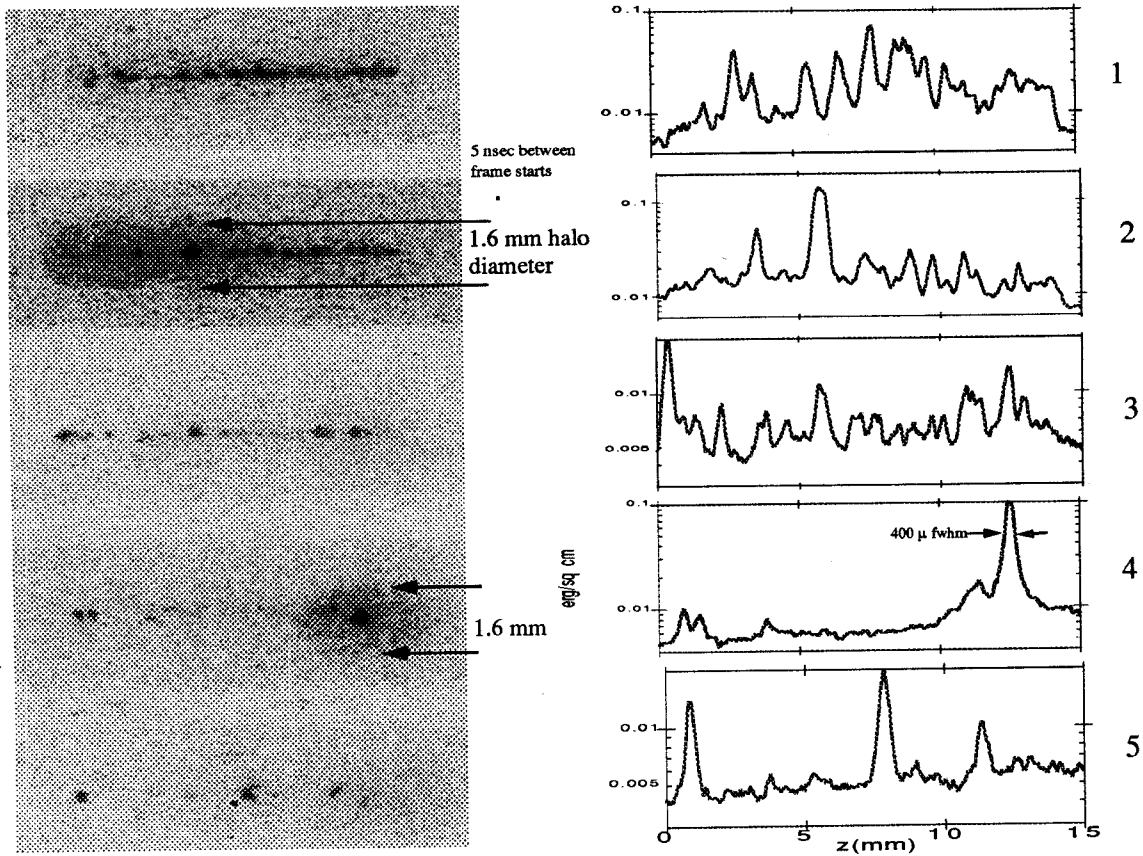
Figure 14. One-ns gated, 25-mm Be filtered pinhole images with line-outs along the z axis for 4-mg tungsten load shot 1857. The time of Frame 1 with respect to the radiation measured is shown in Fig. 15J.
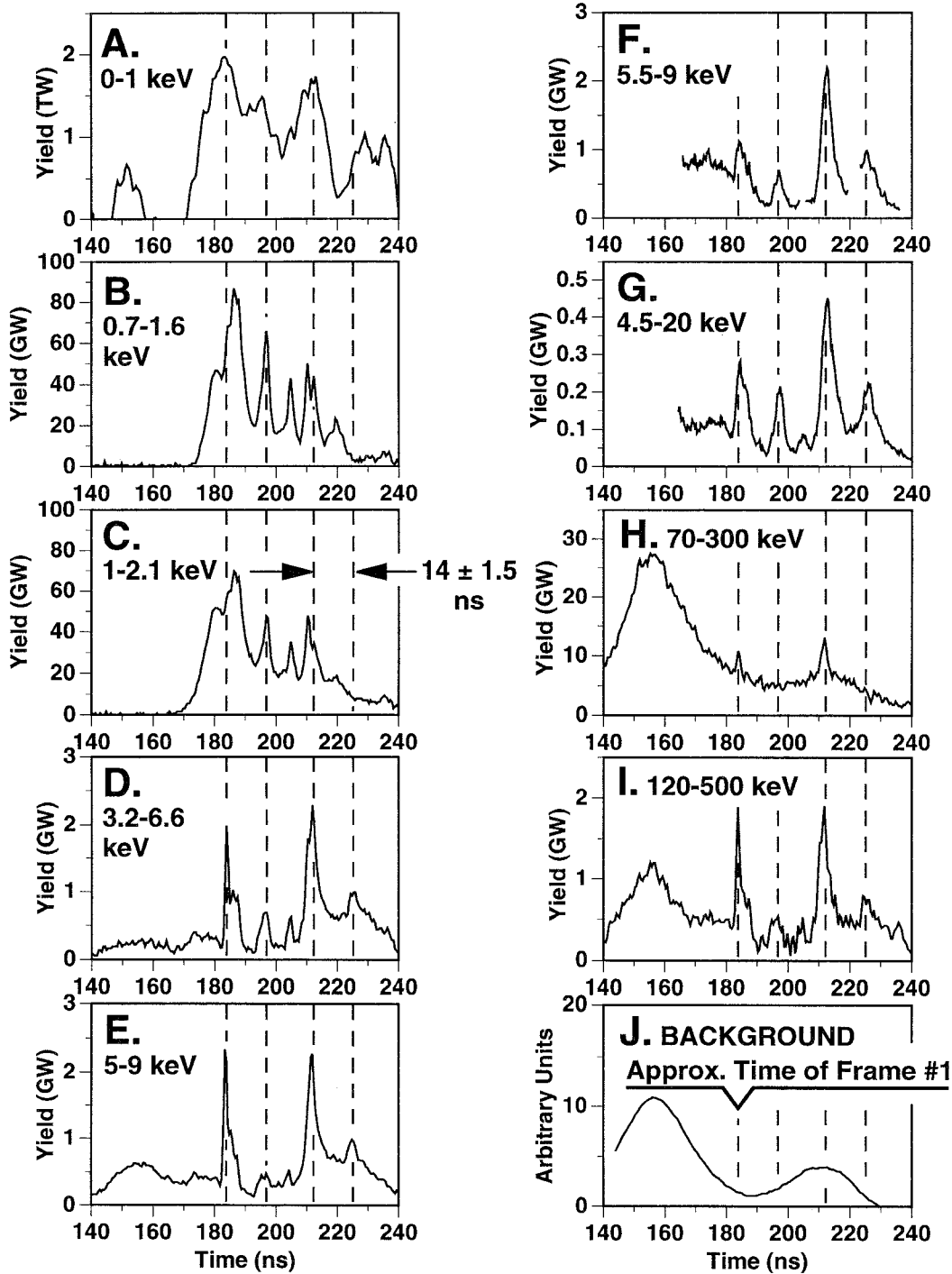
Figure 15. Comparison of the radiation measured for a 4-mg tungsten load (Shot 1857) as a function of the energy response range of the given detector listed in the upper left-hand corner of each figure (except J). (A) corresponds to that measured in the bolometer; (B) through (E) and (H) and (I) correspond to that measured in the PCDs; (F) and (G) correspond to that measured in the modified FFA (see Appendix I); and (J) corresponds to the background measured in a disconnected PCD cable (see Table I). Shown also in (J) is the start time of Frame #1 shown in Fig. 14.

30

appearance of the dominant bright spot shown in frame 4 of Fig. 14 correlates well with the narrow radiation spike measured at 197 ns in the radiation detectors (Fig. 15). The data frequently shows large-diameter radiation halos surrounding bright spots as shown in Frame 4 of Fig. 14. Such halos arise from $hv > 30$-keV x rays that are collimated by the 1.6-mm diameter hole in the Al/Fe structure (TRPHC insert of Fig. 1D) supporting the 76-μm-thick Ta, 50-μm-diameter pinhole used for imaging the softer x rays (Fig. 1D). The halos demonstrate that the hard x rays are also generated near the spots. Following the first implosion, bright spots are observed to occur with about 1-mm spatial frequency along the discharge for all masses in the 1- to 8-mg range (Fig. 16). After the first implosion, the number of spots appears diminished with time as shown in Fig. 17. The time range of the FFC was not sufficient to observe bright spots arising from the latter implosions. The spacing of bright spots is consistent with the growth of the Rayleigh-Taylor (R-T) instability during the initial radial-implosion process (see Sec. IIID).[28]

5. Spectrum

Within the shot-to-shot variation and systematic uncertainty, little time-integrated spectral difference is measured over the mass range of 1 to 4 mg (Fig. 13). Figure 18 shows a typical spectrum for a 4-mg load corresponding to the detector signals shown in Fig. 5. The spectrum is extracted by iterating a trial spectrum together with the detector response functions. Convergence occurred after one iteration. Each data point is located along the abscissa corresponding to the location of the peak response of the associated detector. The horizontal error corresponds to the FWHM of the detector response in the measured spectrum (Table I). As mentioned earlier, the vertical error represents an estimate of the systematic uncertainty arising from the broad energy response of the detectors. The 0.4 keV point comes from the bolometer, the three points between 10 and 30 keV come from the FFA diagnostic, and the remaining points come from the PCD detectors.

The spectrum shows a clear change in slope at about 10 keV, with the measurements below and above 10 keV associated with thermal and nonthermal processes, respectively. Over the range 1 to 10 keV, the thermal spectrum is well fit by

$Y = 4600\left(^{+4600}_{-2300}\right)E^{-(3.4\pm0.7)}$, and over the range 10 to 300 keV the nonthermal spectrum can be

described by $Y = 35\left(^{+35}_{-17}\right)E^{-(1.4\pm0.5)}$, where Y is in J/keV and E is the x-ray energy in keV. The e-folding temperature associated with the thermal spectrum is about 1.3 keV. A detailed measure of the time-integrated spectrum (Fig. 19) using the x-ray crystal spectrometer for a 1-mg load shows that between 0.9 and 1.9 keV, the spectrum is dominated by free-bound continuum transitions, and the enhancement near 2.1 keV is due to Ni-like 3d-to-4f tungsten transitions. The measured slope is consistent with that measured in the PCDs. The discontinuity at 1.55 keV in Fig. 19 is due to absorption by the K-shell edge of the aluminized KIMFOL filter used in the spectrometer. The presence of aluminum was not completely corrected for in the film analysis.

In Fig. 20, the experimental fit of Fig. 18 is compared with a corresponding 1D-RHC spectrum, integrated in time over the duration of the current pulse. Over the thermal region
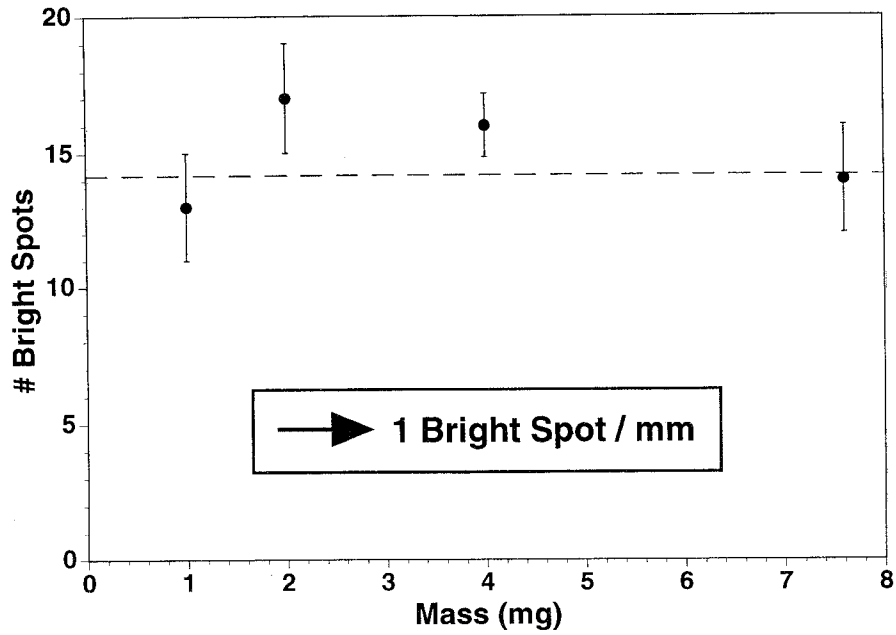
Figure 16. Number of bright spots measured for photon energies 1 to 4 keV in the time-resolved fast-framing x-ray pinhole camera at peak power (first implosion) as a function of the mass of the tungsten load shots. The z-pinch length viewed by the camera corresponds to 15 mm as the bottom 5 mm of the pinch is blocked by the anode wire support structure (Fig. 1D).
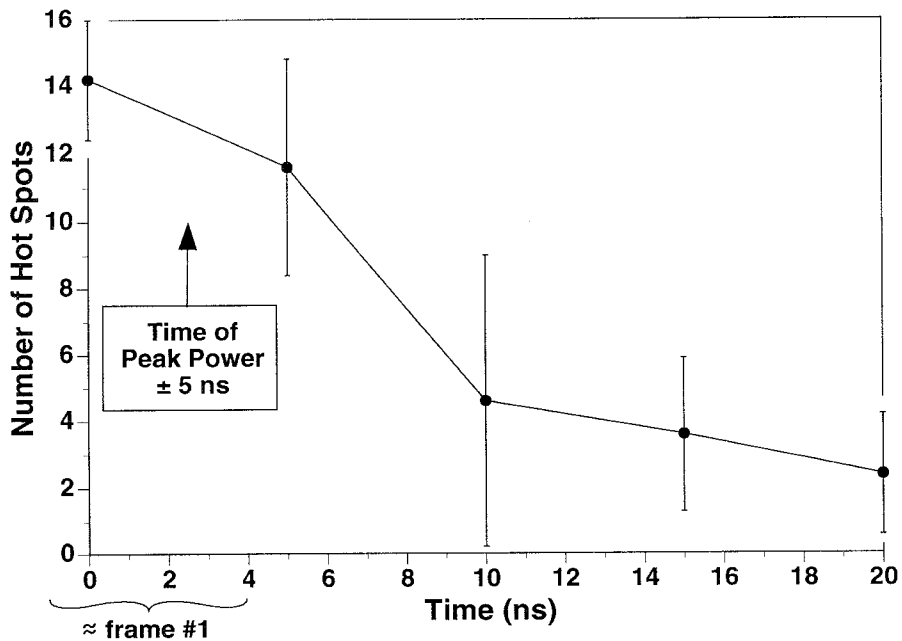
Figure 17. The average number of bright spots measured for photon energies 1 to 4 keV in the time-resolved camera as a function of time for the 4-mg tungsten load shots. Zero to five ns time corresponds to the approximate time of peak power (first implosion). The frame open-time is 2 ns with an inner frame time of 5 ns.
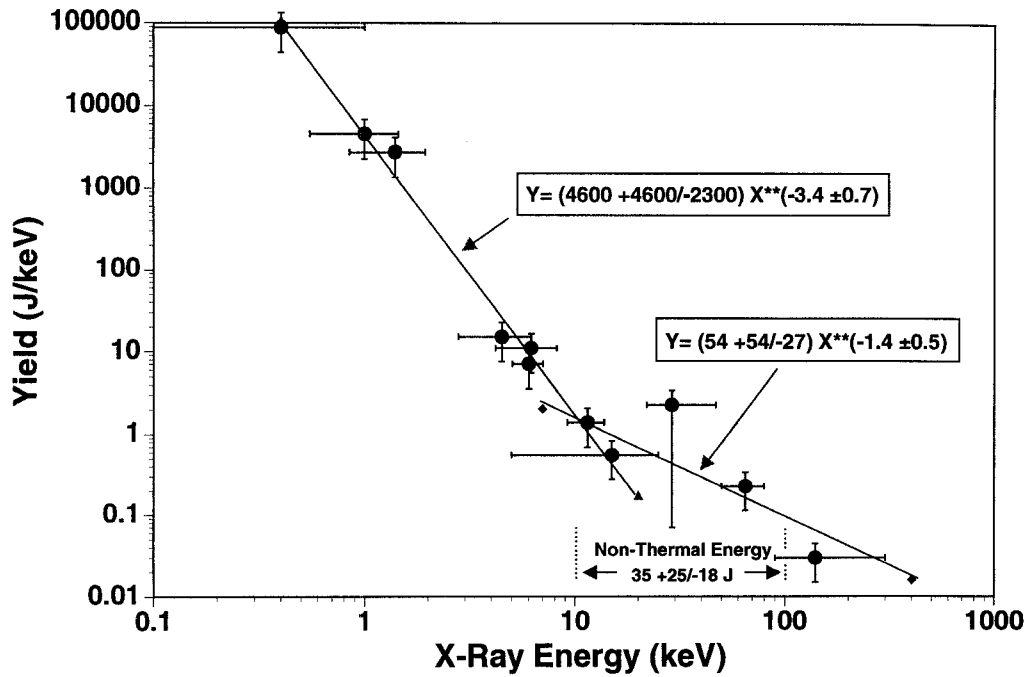
Figure 18. Measured time integrated x-ray yield in J/keV as a function of x-ray energy in keV for the 4-mg tungsten load shot 1864, corresponding to data of Figure 6. The solid lines correspond to power-law fits to the thermal and nonthermal portions of the spectrum.
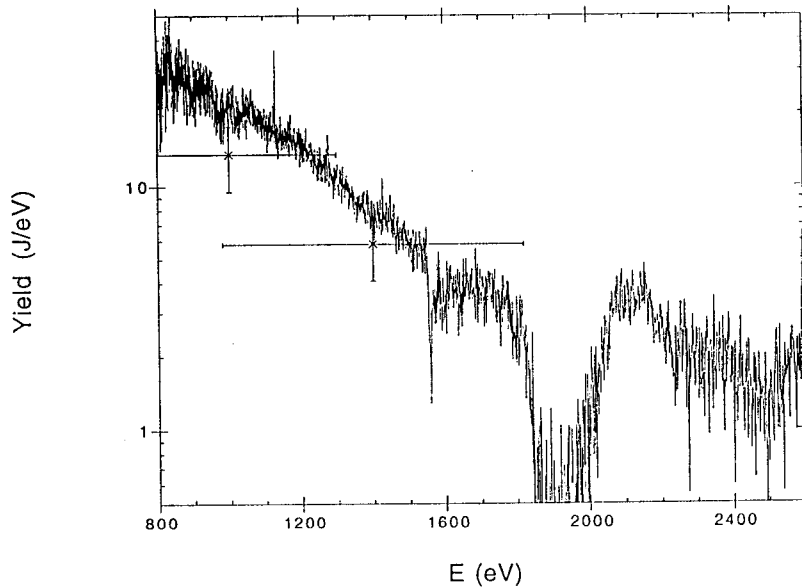
Figure 19. Relative comparison of time integrated x-ray yield in the crystal spectrometer with that measured in the PCDs for a 1-mg tungsten load. The plasma temperature associated with the measured 1/e folding length of the spectrometer data over the range 0.8 to 1.7 keV is 400 eV.

33
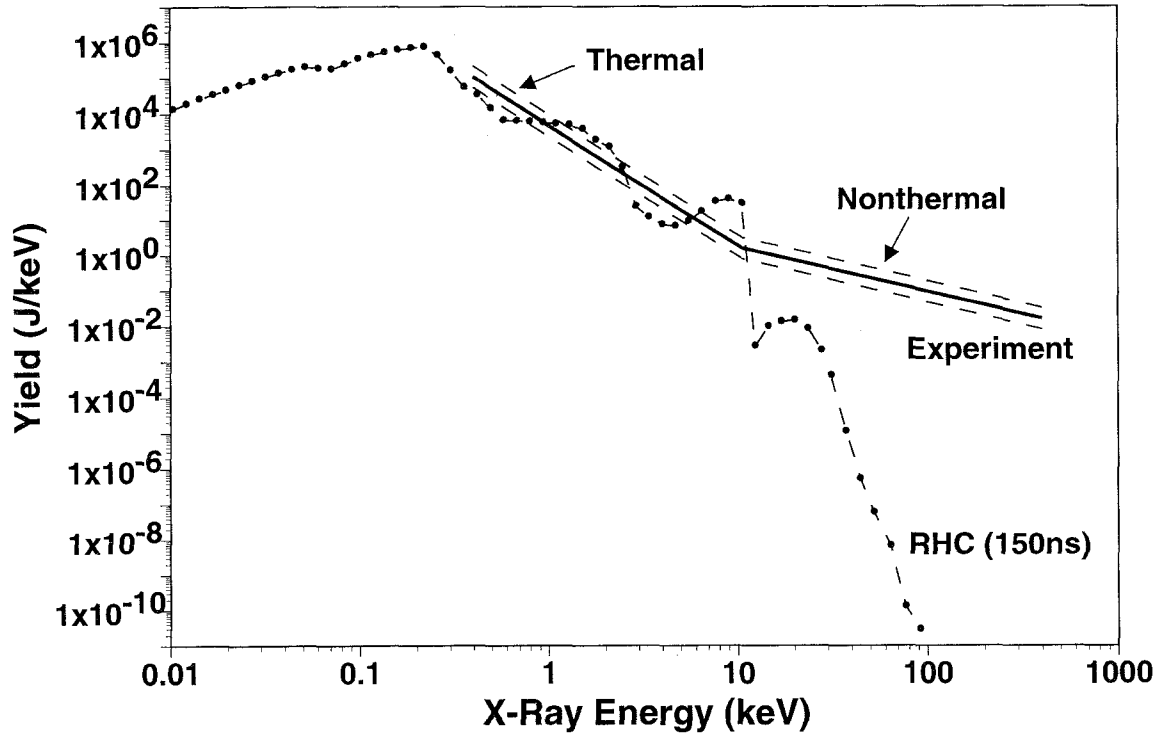
Figure 20. Comparison of the experimentally fitted power-law spectrum (Fig. 18) with that calculated by 1D-RHC for a 4-mg tungsten load.

0.2 to 12 keV, the RHC spectrum can be described by $Y = 3200\,E^{-(3.8\pm0.2)}$, which is in agreement with that measured. The uncertainty reflects the variation calculated due to the number of implosions included in the integration. The comparison of the measured spectrum with the RHC results indicates that the measured points beyond 12 keV are associated with nonthermal processes not accounted for in the simulations. Inclusion of nonthermal-electron modeling in RHC simulations (Appendix II) shows increased x-ray production in the 1- to 10-keV region, but no significant increase above about 10 keV. The slope of the measured spectrum over the 10- to 100-keV range is consistent with that measured in the Gamble-II experiment, which can be described by $Y = 136E^{-1.41}$ (see Sec. IIIC and Fig. 26). This similarity indicates similar nonthermal-electron spectra in the two experiments, thereby suggesting a common production mechanism may be manifest. However, the Gamble-II nonthermal yields were about three times that of the much higher-current Saturn experiments, suggesting that the Saturn implosion geometry cannot produce nonthermal x rays as efficiently as the single-wire Gamble-II discharges.

34

III. DISCUSSION

A. Overview of the Compact Imploded Plasma Radiation Source

Compared to conventional imploding PRS loads, the Saturn compact pinch has an order-of-magnitude higher mass confined in a region of order-of-magnitude smaller diameter, leading to average densities up to 3 orders-of-magnitude higher. The higher densities and correspondingly lower temperatures produce thermal x-ray spectra (Figs. 10 and 18) similar to those of high-atomic-number single-wire discharges; most of the coupled electrical energy is radiated away in the below-1-keV regime with a rapid fall-off above 1 keV. The compact imploded PRS therefore represents a means of achieving the high soft x-ray brightness of single-wire discharges on high-current, low-inductance pulsed-power drivers.

Also similar to single-wire discharges are the appearance of pinch spots along the axis of symmetry of the stagnated plasma. In the Gamble-II experiments with very-high-atomic-number wires, spots were observed to be strung along the pinch axis, each with diameters of order 100 μm (the resolution of the camera) or smaller, separated by diffuse flares of plasma with diameters of order 1 mm. Each spot emitted 2- to 10-ns-wide radiation pulses with 3 to 10 such spots emitting at the same time. Averaged over the discharge history, the pinch spots emitted a major portion of the total thermal and nonthermal radiation.

Following the initial implosion, the Saturn sources form about 1 spot per mm of length (Fig. 16), comparable in periodicity to Gamble II. The fast-framing-camera pinhole images of Fig. 14 demonstrate that the distribution and number of spots vary on the interframe time scale, in agreement with x-ray-streak-camera data from Gamble II. The framing camera images show spots with diameters in the 200- to 400-μm range. Taking the intrinsic camera resolution and that associated with the 50-μm pinhole into account, the smaller pinch spots on Saturn have similar sizes to those on Gamble II.

The framing camera data show a general reduction in spot number with time following the time of peak x-ray power (Fig. 17). In view of the multiple-bounce character of the Saturn source, it is reasonable that this reduction represents the desolution of pinch spots as the plasma expands following the first implosion. Time-resolved images from the second implosion (frames 4 and 5 of Fig. 14) indicate a reduction in spot number compared to the first implosion. Pinch-spot reduction on second or later implosions may be due to the accumulation of initially-imposed and instability-driven asymmetries, which prevent strong radial convergence at some locations. Because pinch spots likely dominate the radiation emission, their reduction may help to explain the observed drop in thermal x-radiation with implosion number (Figs. 11 and 12). The 1D-RHC predictions shown in these figures cannot reproduce the reduction in radiated power with implosion number for radiation dominated by pinch-spot emission and other higher-dimensional effects.

In addition to similarities in thermal x-ray characteristics between single-wire and compact-imploding plasmas, the Saturn experiment confirmed important Gamble-II results concerning pinch spots and nonthermal radiation. In both cases, correlations of temporal and spatial data demonstrate that x-ray emission in all spectral bins is dominated by that from pinch spots. The appearance of hard radiation halos surrounding bright pinch-spot images (two are seen in Fig. 14) confirm that the hardest nonthermal component is associated with pinch spots. The same power-law fall-off of the Saturn nonthermal spectrum with photon energy as Gamble II is observed (Fig. 18 and associated discussion). The Gamble-II current-to-mass scaling for maximum nonthermal emission has been confirmed (Fig. 13) using masses much greater than those of conventional imploded Saturn loads. Finally, Saturn experiments with compact aluminum and copper arrays confirm the strong atomic-number dependence of nonthermal emission (Figs. 9 and 10). This dependence has not been observed in conventional PRS experiments, which have been limited to midrange atomic numbers in order to maximize thermal K- and L-line emission in the below-10-keV range.[2] These confirmations of Gamble-II results at higher Saturn currents demonstrate a common nonthermal x-radiation production mechanism for the single-wire and compact-implosion configurations.

One unique feature of the Saturn compact-imploded source is the apparent "bouncing" of the plasma manifested by multiple radiation spikes occurring simultaneously at all photon energies (Figs. 5, 9, and 15). The period between peaks grows from about 10 ns to about 40 ns as the mass is increased from 1 to 8 mg (Fig. 7). Agreement of this bounce-period variation with 1D-RHC simulations suggests that the behavior is due to a series of plasma-radius oscillations produced by a dynamic imbalance between kinetic and magnetic pressures following the initial implosion (Sec. IIIB below). The process continues until either the driving current pulse decays and the pinch disperses, or excess internal energy is radiated away and an equilibrium pinch is established.

Observation of multiple implosions at high current had not been observed before the present experiment for which the load is designed to implode early in the current pulse. Conventional imploding PRS sources have implosion times occurring later in the current pulse in order to maximize thermal x-ray excitation so that the radial bounce time is comparable to the current-pulse duration, and the plasma disperses before recompression can occur.[2] Single-wire discharges are predicted to have bounce oscillations with much-shorter periods than the current-pulse duration that quickly damp into an equilibrium discharge.[4] The bounce dynamic characteristics of the compact imploding PRS can therefore be considered as between those of conventional-imploding and single-wire sources.

B. One-Dimensional Modeling of Compact PRS Dynamics

A one-dimensional version of the RHC radiation hydrodynamic code[16] (Appendix II), the hydrodynamic code HC (Appendix III),[17] and associated simpler analyses have been used to provide a basic understanding of the overall dynamic and radiation characteristics of the

Saturn compact PRS. Examples of RHC comparisons with the experiment are shown in Figs. 5, 7, 8, 10-13, and 20.

1. Load Current Confirmation from Bounce Dynamics

As there were no operational monitors for the current flowing in the PRS, an important aspect of the theory-experiment comparison is to confirm that current levels measured in detectors upstream of the load are representative of those flowing in the discharge. One such confirmation is provided by Fig. 4, where the measured implosion times for various mass loads are compared to predictions of ZORK and the corresponding RHC runs employing the ZORK circuit-model. In ZORK, the load is treated as a time-varying inductance, composed of a thin, current-carrying annulus of mass that is imploded by self-magnetic forces. This type of zero-dimensional modeling is commonly used to determine implosion times and implosion kinetic energies of conventional annular PRS loads.[27] It has the benefit of being the simplest model with some predictive capability for implosion dynamics. It has the drawback of neglecting all internal degrees of freedom (pressure, temperature, etc.), so that the load dynamics cannot be followed after forms of energy other than magnetic and kinetic become significant. For ZORK, the annulus radius is fixed at $1/10^{th}$ of the initial radius after imploding to that value. The corresponding RHC computations[17] predict implosion times nearly identical to ZORK because plasma temperature and pressure play a negligible role prior to entering the bounce phase. Either model supports the hypothesis that, except for the weakly radiating 16-mg loads, most of the current measured upstream of the load must be flowing in the implosion, assuming that the bulk of the plasma participates. If not, the measured implosion times would be substantially greater than those predicted.

Because the load current inferred from upstream current monitors is close to linearly rising for most of the implosion phase, the sensitivity of the implosion time τ on load current can be estimated by considering the zero-dimensional analysis for a linearly-rising current.[27] For $I(t) = \dot{I}t$, this analysis yields

$$mR^2 = 1.26 \times 10^{-3} I^2(\tau)\tau^2 \tag{1}$$

where m is the line mass in g/cm, R = 0.2 cm is the initial annular wire-array radius, I(t) is in A, and τ is in s. Fitting a linear current rise to I_{load} in Fig. 2D, $\dot{I} \approx 1.2 \times 10^{14}$ leads to $\tau = 33M^{1/4}$ ns, where M(mg) = $2 \times 10^3 m$ for a 2-cm load length. This result is close to the experimental values and ZORK predictions shown in Fig. 4. Because Eq. (1) reproduces the variation of implosion time with mass, it can also be used to predict that $\tau \propto 1/I(\tau)$. Figure 4 shows that the maximum deviation of implosion time from the ZORK prediction is less than 10% for masses of 8 mg or less, implying a comparable maximum deviation of the load current from the values calculated from upstream current monitors.

Corroboration of the assumed load current is also provided by comparison of the observed bounce period with the RHC predictions shown in Figs. 7 and 8. The RHC

computations use the ZORK circuit model and treat the initial wire-array configuration as an annulus of radius 2 mm, thickness 80 μm (arbitrarily chosen), and length 2 cm. Load-current and radius time histories (displaying the motion of selected radial zones) for the case of a 4-mg load are shown in Figs. 21A and B. The agreement of bounce period with measurements in Figs. 5, 7, and 8 is consistent with the current levels flowing in the experimental load as exemplified by Fig. 21A.
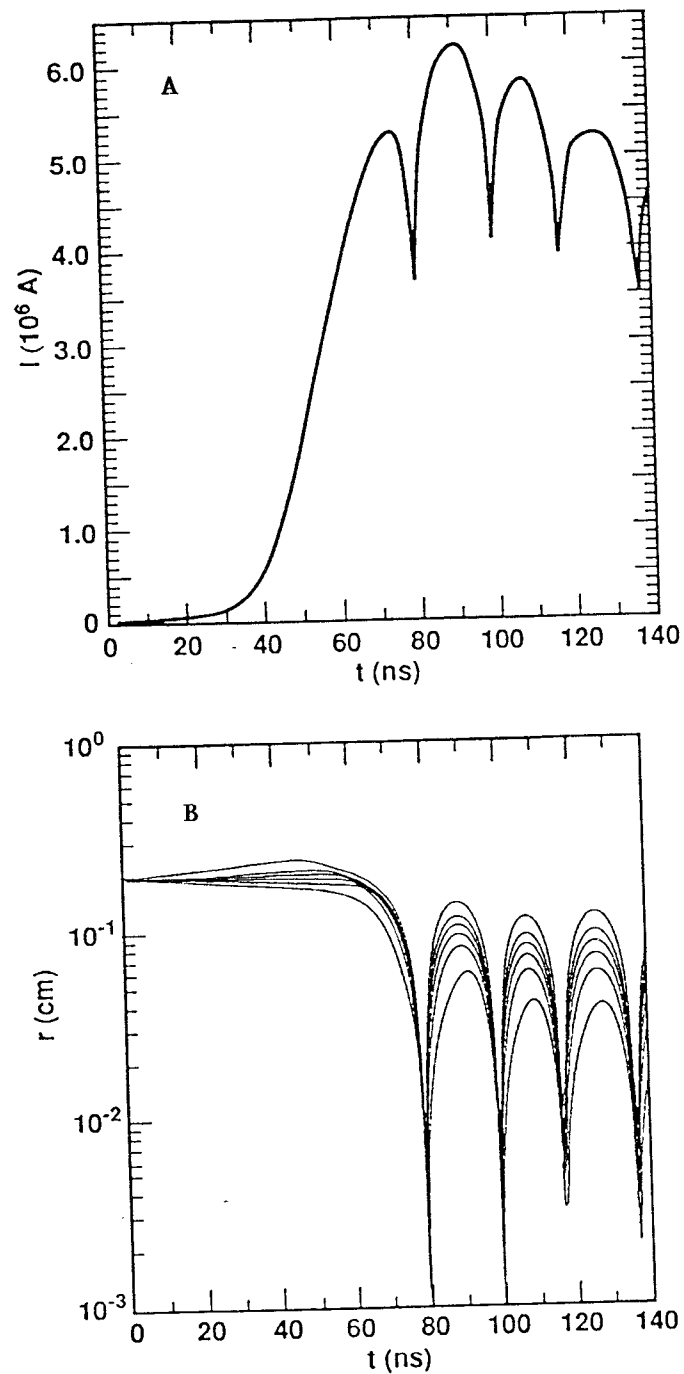
Figure 21. 1D-RHC simulation of the (A) load current and (B) radial zones of the plasma load as functions of time for a 4-mg tungsten load.

The variation of bounce-period with experimental parameters can be understood through arguments similar to those employed for Eq. (1). Consider a zero-dimensional analysis applied to the implosion and subsequent bouncing of a load driven by a constant current. For that case,[26] the implosion time τ_c is half of the value given in Eq. (1) when I(t) is identified with the constant current I_0. If the plasma experienced no radiation losses or heating other than that provided by stagnation of kinetic energy, the sum of load kinetic, internal, and magnetic energies would be conserved, and the load would repeatedly bounce out to the initial radius and reimplode for the duration of the constant-current pulse. The bounce period $\Delta\tau$ would then be $2\tau_c$ by symmetry. However, radiation losses during the peak-compression phase rob the load of energy and the plasma rebounds to a smaller radius R_1. From the scaling of Eq. (1), the bounce period is then reduced by a factor (R_1/R). If, as Fig. 21A indicates, the implosion is assumed to occur during a linearly-increasing current, and subsequent bounces occur during a period of roughly-constant current, the above argument suggests:

$$mR_1^2 = 126 \times 10^{-3} I^2(\tau)(\Delta\tau)^2 \ . \tag{2}$$

Equation (2) is in good agreement with the experiment and RHC result for a 4-mg mass when $R_1 = 0.09$ cm is chosen for the center of the peak-expansion radial spread shown in Fig. 21B.

The relative constancy of bounce period with bounce number shown in Fig. 8 follows from Eq. (2) and Fig. 21B, where the rebound radius is nearly constant over three bounces. Because the observed and predicted radiation losses are substantial for later bounces (Fig. 5), constant rebound radius implies that resistive heating plays a significant role in the load energetics during the bounce phase.

The data of Figs. 4 and 7 show that the ratio $\tau/\Delta\tau$ decreases somewhat with mass though the ratio from Eqs. (1) and (2) is constant. Qualitatively, this behavior can be understood from the above arguments when the experimental current variation is considered. For low masses and early implosion times, the current continues to increase after the first implosion so that $\Delta\tau$ is decreased relative to τ. For high masses and late implosion times, the first bounce experiences the current decrease at the end of the driving pulse and $\Delta\tau$ is increased relative to τ. For any mass, the sensitivity of bounce period on current is the same as for the implosion time, so that agreement between calculation and experiment again confirms 5-MA load-current levels.

Figure 10 compares the total measured radiation (labeled 0.4 keV for the bolometer measurements) with RHC predictions for 4-mg loads of various atomic number. The total yield is obtained from Fig. 10 by multiplying the J/keV values shown by 0.8 keV (the assumed spectral width of the detector). It is not surprising that the total measured radiation yields are comparable for the three atomic numbers because the bulk of the radiation is sub-keV for which the high-density, few-hundred-eV plasma is optically thick. The plasma energy can then be efficiently radiated away independent of atomic number.

Zero-dimensional modeling can be used to establish approximate bounds on the sensitivity of radiation emission on discharge current. For the constant-current case considered above, the implosion kinetic energy is given by $K = I_0^2 \Delta L / 2$, where

$$\Delta L = 2 \times 10^{-9} \ell \ln(R / R_f) \tag{3}$$

is the change in inductance (Henries) experienced by a load of length ℓ (cm) imploding to stagnation radius R_f. For a linearly-rising current pulse,[27] K is decreased by about 20% so that

$$K(J) = 0.8 \times 10^{-9} I^2(\tau) \ell \ln(R / R_f) \tag{4}$$

For a 5.5-MA peak load current before implosion, 2-cm length, and a 10-to-1 radial compression consistent with the pinhole images, Eq. (4) predicts a kinetic energy of about 110 kJ in approximate agreement with ZORK. Without strong resistive heating, this implosion energy represents the maximum energy that can be radiated away, so that the measured yields from Fig. 10 (64 to 74 kJ) are energetically consistent with the assumed discharge current. There are a number of reasons for the kinetic energy to overestimate the radiation yield. For example, not all of the available energy can be radiated (there is residual internal and kinetic energy at the end of the current pulse), and the observed asymmetries and instabilities may disrupt plasma confinement, locally quenching the radiation. Indeed, considering the spotty spatial nature of the source, it is surprising that the total radiated energy fraction is as close to unity as it is. Such a large fraction suggests that higher compressions than 10 may be achieved in the pinch spots, and that resistive heating may provide additional heating in the highly-compressed regions.[4,15,26]

The 1D-RHC simulation results shown in Fig. 10 have x-ray yields varying from two- to three-times the measured values. The high compressions attributed just above to the experimental pinch spots occur over the full 2-cm length of the plasma in the 1-D simulations (Fig. 21B), so that the predicted radiation yields exceed those observed. Note that the predicted yields are comparable to the implosion energy calculated in Eq. (4) using the unrealistic 100-to-1 compression ratio of the 1D simulation. Despite the yield differences, Fig. 20 shows that the predicted spectrum for 4-mg tungsten loads follows the shape of the experimental thermal spectrum, indicating that calculated temperature distributions are consistent with a 5-MA driving current.

2. Low-Mass Dynamics and Radiation

The experiment-RHC yield comparison in Fig. 13 shows that the yield discrepancy is enhanced for low-mass loads. Figure 22 for a 1-mg-tungsten RHC simulation illustrates that the increased discrepancy is due to a change in load dynamics from a bounce mode to an equilibrium pinch. For low masses, the rapid bounces observed and calculated by Eq. (2) are predicted by RHC to decay as the kinetic energy is radiated away. This process appears for low mass because a portion of the kinetic energy can be radiated away in a burst at each
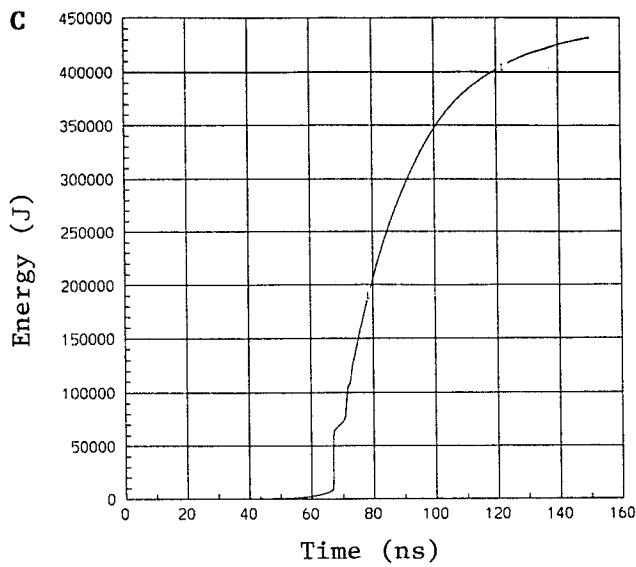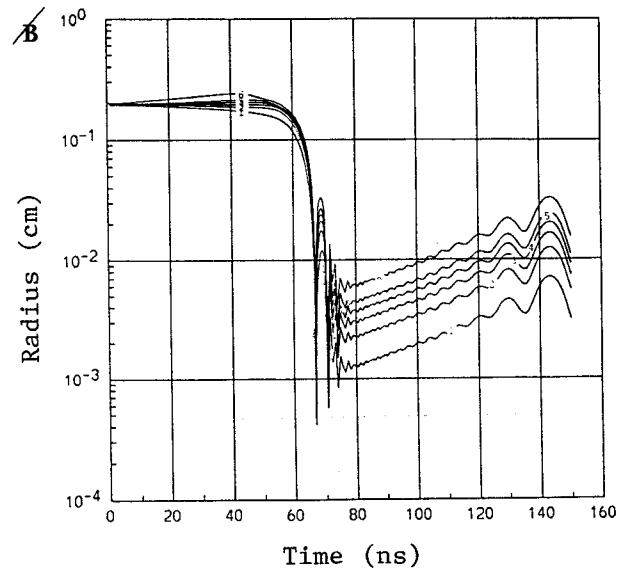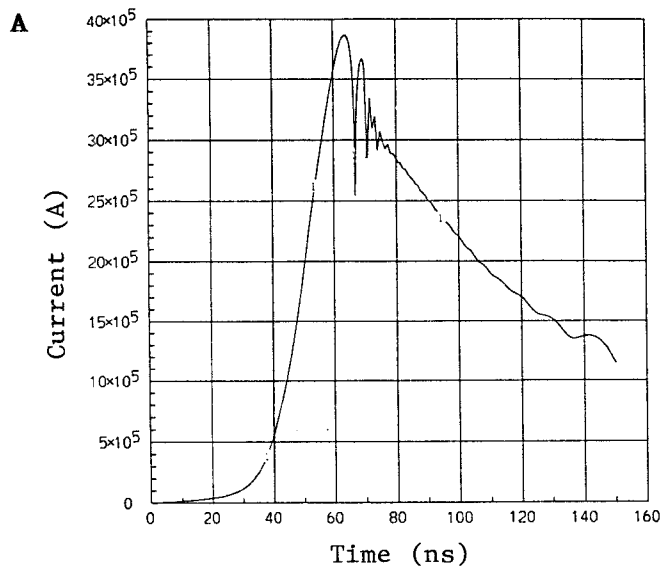
Figure 22. 1D-RHC simulation of the (A) load current, (B) radial zones, and (C) total radiated energy as functions of time for a 1-mg tungsten load.

compression, so that a rapid sequence of compressions allows all of the kinetic energy to be lost in a time shorter than the current-pulse duration. This radiative-decay of kinetic energy has been predicted in 1-D simulations of single-wire loads.[4]

The slow change in radius occurring after decay of the radial oscillations results from a balance between optically-thick radiation losses and resistive heating. Figure 22C shows that the kinetic energy is radiated away after a few bounces, with the remaining large radiation yield emitted continuously as the current pulse decreases in a manner consistent with the resistive decay of inductive energy stored in the load. Though the peak radiated power during this phase is much lower than that associated with conversion of kinetic energy in the earlier radiation spikes, the total energy radiated is much higher because it is emitted continuously over the current pulse.

As the equilibrium-pinch phase reflects both pressure and energy balance, the plasma radius slowly expands against the decreasing magnetic field (Fig. 22B). This behavior is identical to that predicted for very-high-atomic-number, single-wire discharges[4] and the transition from a bounce to a resistive phase has been described by self-similar modeling of imploded, radiation-dominated plasmas.[26] Although this 1D behavior is not observed in the experiment, the resistive phase shown in the low-mass RHC calculations is of interest because it has been proposed to explain the small size of pinch spots for which radiation collapse terminates in such a state.[15]

A simple model combining pressure and energy balance can be used to quantify the behavior shown in Fig. 22. Consider a z-pinch plasma of temperature $T(eV)$, ionization state Z, outer radius $a(cm)$, ion line density $N = m/1.67 \times 10^{-24} A$, where A is the atomic weight, and axial current $I(A)$. The density and current density are uniformly distributed, and are given by $n_i = N / \pi a^2$, $j = I / \pi a^2$. Balancing the radial kinetic pressure against the magnetic pressure at the plasma boundary results in the Bennett relation

$$(1 + Z)NT = 3 \times 10^9 I^2 \quad . \tag{5}$$

For an optically-thick plasma, blackbody radiation from the plasma surface is balanced by ohmic dissipation in the volume, so that

$$2\pi a \sigma T^4 = \eta I^2 / \pi a^2 \quad ; \quad \eta = 1 \times 10^{-2} Z / T^{3/2} \quad . \tag{6}$$

Spitzer resistivity transverse to a strong magnetic field is assumed with $ln\Lambda = 1$ for the high-densities of this problem. Eliminating temperature between Eqs. (5) and (6) leads to

$$a = \frac{7.2 \times 10^{-21} Z^2 N^2}{I^3} \left(\frac{Z}{N} \right)^{1/6} \quad . \tag{7}$$

The system of equations is closed by fitting $Z(T)$ from an average-atom model[29] for tungsten to a power law in the 100-eV to 1-keV regime: $Z \approx 7T^{0.26}$. Then, as the current in

42

Fig. 22A decays from 3 MA to 1.5 MA, Eq. (5) predicts T decreases from 550 eV to 175 eV for a 1-mg load. During this time, Eq. (7) is an excellent fit to the lowest radial zone plotted in Fig. 22B, demonstrating that an optically-thick equilibrium model holds for the high-density regime following radiative decay of kinetic energy. It is important to note that no such equilibrium exists for optically-thin plasmas. In that case, the radiation losses and ohmic heating have the same radius dependence, and energy balance can only be achieved at a single value of current, well below 1-MA for high-atomic-number plasmas.[26] Higher currents in optically-thin plasmas produce rapid radiation collapse to smaller radii where increased opacity permits energy balance.

3. Imploded Plasma Characterization

RHC results and Eq. (2) demonstrate that the bounce period depends on the rebound radius, and that the rebound radius is reduced by dissipation of plasma energy through radiation bursts at peak compression (Figs. 21 and 22, and Eq. (4)). It is then clear that radiation modeling will effect predictions of bounce dynamics. Computations using the HC hydrocode (Appendix III) have been used test the sensitivity of bounce period on radiation. Although HC does not have the sophisticated atomic-physics and radiation-transport models employed by RHC, its simplicity provides greater access to control of fundamental processes, and allows one to perform computer experiments to probe the underlying physics of complex problems.

Figure 23 shows how the bounce dynamics predicted by 1D-HC varies with the assumed radiation emission. The figure shows the motion of the center-of-mass radius for various values of the coefficient C_R in the equation

$$\lambda = C_R/\rho^2 \ , \tag{8}$$

where $\lambda(m)$ is the radiation mean-free-path and $\rho(kg/m^3)$ is the mass density. The assumed radiation loss rate increases in proportion to C_R at each bounce, so that larger C_R values produce rebounds with reduced plasma energy, rebound radius, and bounce period. For large values of the coefficient, radiation losses dominate the energetics, the plasma goes into radiation collapse following the first compression, and no bounces occur.

Figure 24 shows the variation of radius, current, and load voltage predicted by HC for a 4-mg load using a radiation coefficient adjusted to provide a time between the first and second implosions comparable to that observed in the experiment. The letter labels in Figure 24 correspond the times of the radial profiles shown in Figs. 25A - E. The first plot at each time shows the mass density, temperature, magnetic field strength, and radial fluid velocity. The second shows the current density, axial electric field, and the v×B (inductive) contribution to the electric field. Note that because E_z is close to $-v_r B_\theta$, the inductive contribution to the electric field dominates over the resistive contribution except near the symmetry axis.
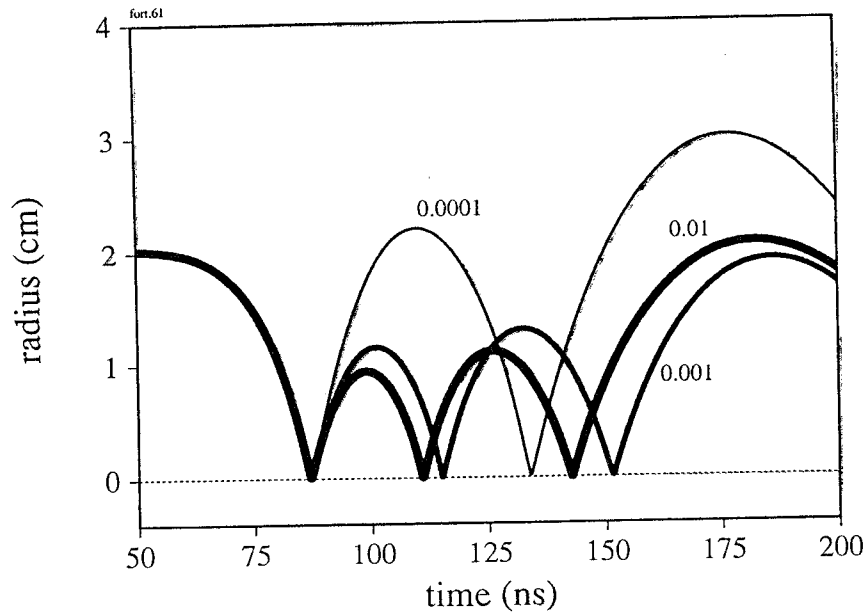
Figure 23. HC simulations of the center-of-mass radius as functions of time for 4-mg tungsten loads and various values of the radiation parameter C_R in kg/m^2.
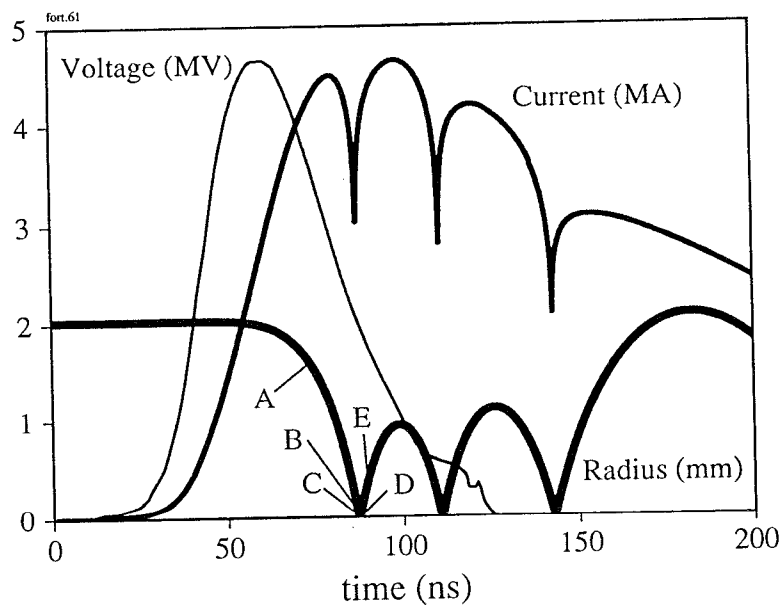
Figure 24. HC simulation of the load voltage, current, and center-of-mass radius for a 4-mg tungsten load and $C_R = 0.01$ kg/m^2. The letter labels indicate the times corresponding to the radial profiles shown in Fig. 25.

44
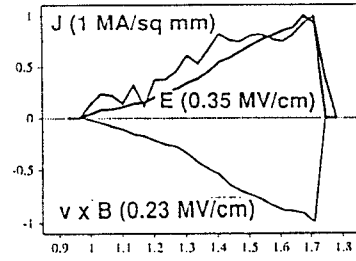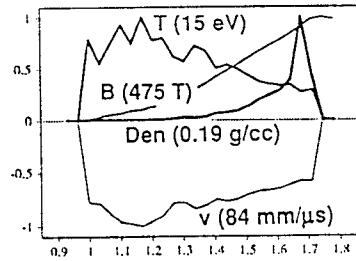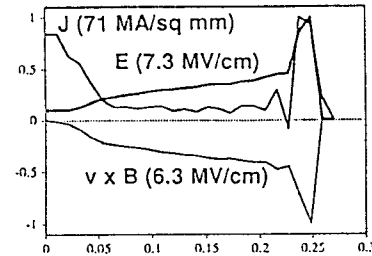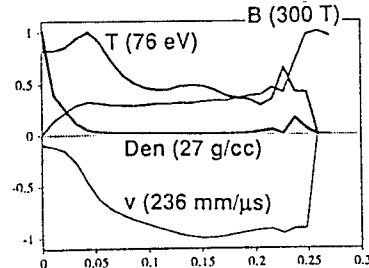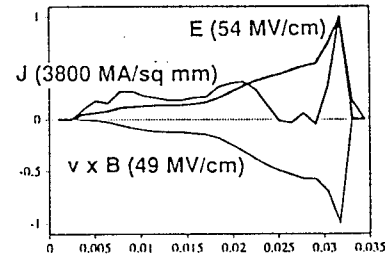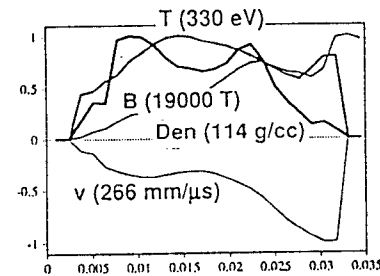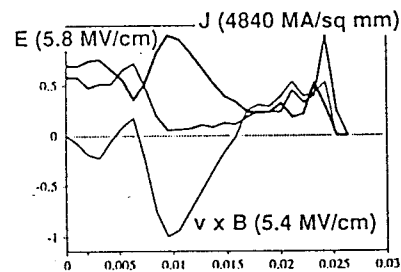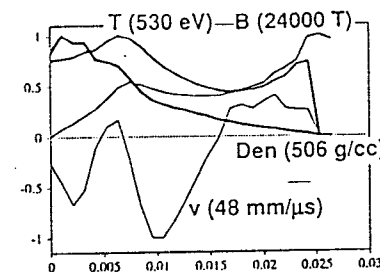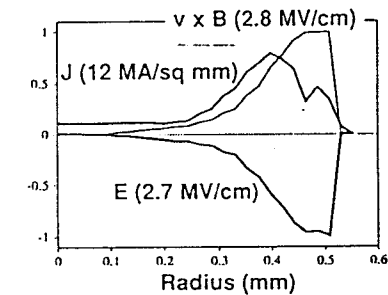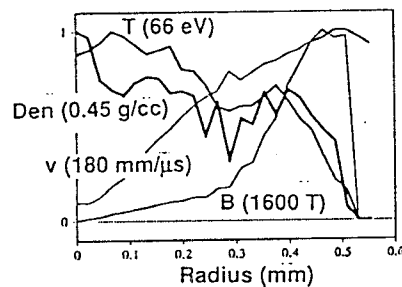
Figure 25. HC radial profiles for the case of Fig. 24 at 5 times during the first implosion and bounce. At each time, the first figure shows magnetic field density, temperature, and radial velocity. The second figure at each time shows current density, electric-field and the inductive v×B component of electric field.

45

The temperature rise at the inner radius in Fig. 25A reflects the compressive work done on the plasma. The magnetic field has penetrated quickly because the temperature, and, therefore, the conductivity are initially low. At time B, the inner radius of the plasma reaches the origin, creating a spike in density and temperature as kinetic energy is thermalized. At time C, just prior to peak compression, the largest velocity and electric-field values are achieved. At time D, the plasma has stagnated at maximum compression as indicated by the reduced velocity values of both signs. At time E, the velocity is positive throughout the expanding plasma, and the current increases due to the reduced load inductance. Eventually, expansion and radiation cooling lowers the plasma pressure sufficiently to allow a second compression. The high peak values of density, magnetic-, and electric-field strengths result from the 100-to-1 radial compression allowed by a 1-dimensional treatment. Though certainly not representative of the overall experimental load, such compressions may be representative of the pinch spots.

The large inductive-electric fields predicted by HC at high compression can be simply understood. The induced voltage drop across a plasma load of outer radius r(t) is given by

$$V = \frac{d}{dt}(LI) \approx I\frac{dL}{dt} = -2\times10^{-9}\,\ell\frac{\dot{r}}{r}I, \tag{9}$$

where the $L\dot{I}$ term, smaller than the $\dot{L}I$ term during the current dip, has been neglected. The implosion velocity $\dot{r}$ can be estimated from Eq. (4) with $R_f = r$ and $K = m\ell\dot{r}^2/2$, demonstrating that $\dot{r}$ depends weakly on r. Thus, the induced electric field $E = V/\ell$ scales inversely with radius. For Fig. 25C, I = 3 MA, and the peak value of $\dot{r}$ is -2.7×10^7 cm/s at r = 0.003 cm. Substituting these values into the right-hand-side of Eq. (9) results in E = 54 MV/cm, equal to the peak electric-field value in the figure. The data of Fig. 25 are used in the next section to determine if the extreme plasma conditions predicted by HC can explain nonthermal electron creation and production of the associated radiation. Of course, in 2D calculations, the local electric field could become larger than this estimate because of smaller length scales.

C. Modeling of Nonthermal Electron Production from 1D Analyses

As in the present experiment, nonthermal x-ray spectra have been observed in various high-atomic-number z-pinch plasmas, indicating that electrons with energies greatly in excess of the plasma temperature are present.[7,8,30-32] The Gamble-II data obtained with single tungsten wires is of particular interest because the observed 0.25% x-ray efficiency for 5- to 100-keV photons required about 1/3 of the total discharge current to be in the form of nonthermal electrons.[8] The Gamble-II data also show a strong dependence of nonthermal radiation on atomic-number; the results for aluminum, copper, and tungsten shown in Fig. 26 demonstrate an order-of-magnitude increase in nonthermal x-ray yield for each step up in atomic number. Although cold-target radiation emission scales with atomic number, a
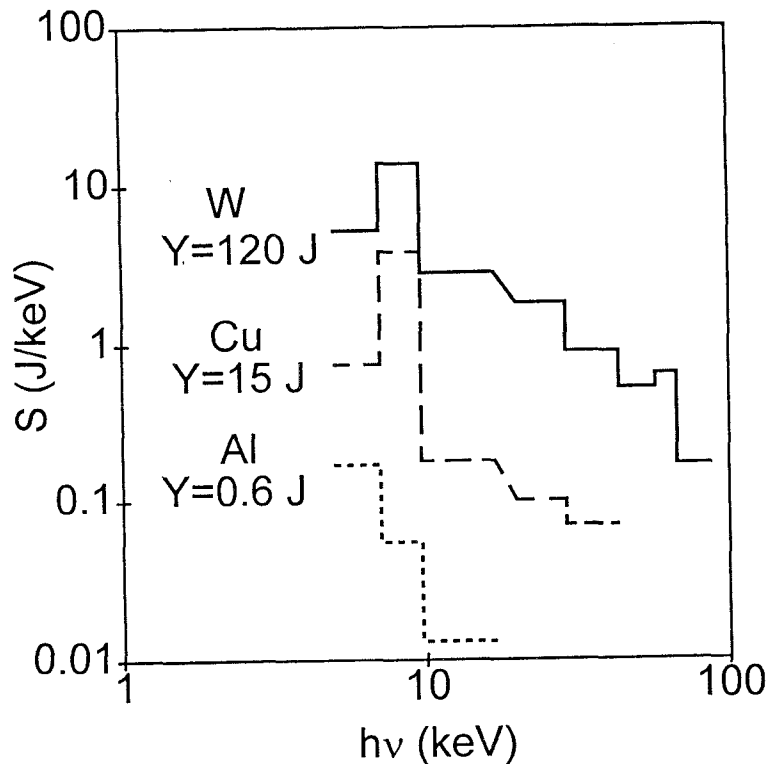
Figure 26. Nonthermal x-ray spectra for Gamble-II single-wire loads of aluminum, copper, and tungsten, each 50 μm in diameter.

portion of the increase is due to the observed hardening of the spectrum. For each atomic number, the continuum spectrum can be fit by bremsstrahlung emission from a power-law electron-energy distribution $f(K) \sim K^{-n}$ with $n \approx 3.4$, 1.7, and 0.85 for Al, Cu, and W, respectively.[8] These data therefore demonstrate an increase of nonthermal-electron energy with atomic number. The Saturn results shown in Figs. 9 and 10 are consistent with the Gamble-II observations.

A widely-proposed mechanism for nonthermal electron production is acceleration in the inductive electric fields produced by localized radial collapse of plasma into pinch spots.[15,33,34] One problem with this process is the presence of intense (megagauss) azimuthal magnetic fields embedded in the plasma, which impede the motion of electrons along the electric field. Appendix IV employs a fluid model for nonthermal electron flow in dense, high-atomic-number plasmas[35] to determine how collisions mediate energy gain in crossed electric and magnetic fields. There, simple scaling laws derived from this model are shown to be in good agreement with IPROP particle-in-cell simulations[36] of the same plasma environment.

In a hydrogenic plasma, an electron can gain energy from the electric field until its collision frequency in the background plasma is reduced to below the electron cyclotron frequency. Subsequently, it is constrained to move perpendicular to the electric field for a

time comparable to that for collisional energy-loss to background electrons, and energy gain slows. In the very high-atomic-number plasmas of interest here, the electron scattering (momentum-transfer) frequency v_s is of order Zv_e, where v_e is the rate associated with collisional energy loss to low-energy plasma electrons. In that case, a large number of scattering collisions along the electric field can occur in an energy-loss time and larger energy gains are possible than in hydrogenic plasmas. This hypothesis is developed and evaluated in Appendix IV as a mechanism for nonthermal electron production.

The results of the Appendix IV analyses can be summarized as follows. For electric fields in excess of a critical field E_c, electrons with initial energies in excess of a minimum value K_0 will gain energy from scattering collisions along the electric field until an asymptotic value K_f is achieved. These quantities are defined by

$$E_c(V/cm) = 3\times10^{-5}\varepsilon^{1/2}\Omega_c^{2/3}\Omega_s^{1/3} \qquad\qquad \sim B^{2/3}n_i^{1/3}Z^{1/6}, \qquad\qquad (10)$$

$$K_0(eV) = 6\varepsilon^{1/2}\Omega_s/E \qquad\qquad \sim n_iZ^{3/2}/E, \qquad\qquad (11)$$

$$K_f(eV) = 6\times10^{14}E^2/\varepsilon\Omega_c^2 \qquad\qquad \sim ZE^2/B^2, \qquad\qquad (12)$$

and are related to basic plasma parameters on the right-hand side. In these equations, $\varepsilon = 1/(Z+2)$, Ω_c is the electron cyclotron frequency, and Ω_s is the elastic scattering frequency for a 250-keV electron. The time required for the energy to approach K_f is of order $(1-10)$ Ω_s^{-1} for final energies in the 10- to 100-keV range (Fig. 4 of Appendix IV). For electric fields lower than E_c or initial electron energies below K_0, no energy gain above thermal levels is predicted. When the magnetic field approaches zero, only Eq. (11), essentially the Dreicer runaway condition,[37] remains significant. As shown in Appendix IV, this equation set is in good agreement with IPROP computations for electric fields significantly in excess of E_c. Equation (11) is in qualitative agreement with experimental results since $K_f \sim Z$ predicts spectral hardening with ionization level.

These relations can be used to estimate nonthermal-electron-energy gain for the experimental plasma parameters. For Saturn tungsten-load masses of 1 to 8 mg, the ion line density is in the range 10^{18} - 10^{19} cm^{-1}, where the low end includes values for the Gamble-II experiments. A range of ion densities $n_i \approx 10^{20}$ - 10^{21} cm^{-3} results for a uniform plasma within the 0.05-cm-radius diffuse regions of both Saturn small-diameter-array and Gamble-II single-wire discharges, resulting in $\Omega_s \approx 4\times10^{10}$ - 4×10^{11} s^{-1} for tungsten plasmas. The electron-cyclotron-frequency range at this radius for Gamble-II and Saturn current levels is $\Omega_c \approx$ 5×10^{13} - 2×10^{14}. For this parameter range, Table II lists E_c, E required to achieve $K_f = 100$ keV, and the initial required electron energy K_0 for energy gain at these electric-field values.

Table II

Parameters for K_f = 100 keV in Tungsten

Ω_s (s^{-1})	4×10^{10}	4×10^{11}	4×10^{10}	4×10^{11}
Ω_c (rad/s)	5×10^{13}	5×10^{13}	2×10^{14}	2×10^{14}
E_c (MV/cm)	24	51	60	129
E (MV/cm) for K_f	104	104	414	414
K_0 (keV)	0.37	3.7	0.092	0.92

The table indicates that the electric fields required for a 100-keV class of nonthermal electrons are in the 100 MV/cm regime. Thermal electrons with energies given by the last row of the table can be accelerated out of the plasma background by this field. The time scale for energy gain to the final energy for the specified Ω_s values are in the 10^{-11}- to 10^{-10}-s regime. Final electron energies less than 100 keV can be realized with electric fields approaching E_c. Reductions in E_c can be realized by lowering the plasma density, but Eq. (10) shows that a density reduction by 10^3 is required for an order-of-magnitude reduction in the critical electric field. Though one can imagine such low densities in the regions outside of pinch spots and between flares, the nanosecond time scale allowed for inductive-electric-field creation by z-pinch implosion or pinch-spot collapse is then too short for energy gain to K_f. The electric-field values shown in the table therefore represent reasonable estimates of those required by the load dynamics and average load densities.

The electric-field values shown in the left two columns of the table are at the top of the range estimated for sausage-instability pinch-spot collapse[15] at Gamble-II current levels. The nonthermal analysis can therefore marginally explain nonthermal electron production by strong 2-D processes in these high-atomic-number pinch plasmas. However, the values of E shown in the two right columns of Table II are an order-of-magnitude higher than the largest fields predicted in 1-D by the above HC simulations of Saturn implosions.

Quantitative comparisons of the electric fields produced in HC with those required for nonthermal-electron production are provided in Figs. 27 and 28. Figure 27 plots the ratio $P = E(r)/E_c(r)$ for the case and times shown in Fig. 25. The electric field is always smaller than the critical field calculated from Eq. (10). Near the axis of symmetry, where the magnetic field is small, Eq. (11) determines the ability to extract nonthermal electrons out of the plasma background. The time variations of Fig. 28 show that the axial plasma temperature is always much less than the required initial electron energy for nonthermal extraction. During times of strong compressional heating, the plasma is too dense, when it is at lower density, the plasma is too cool. The disparity between temperature and required initial energy is preserved as one moves off axis, indicating that failure to satisfy Eq. (11) alone is sufficient to preclude nonthermal electron production with the electric fields predicted by 1-D modeling.
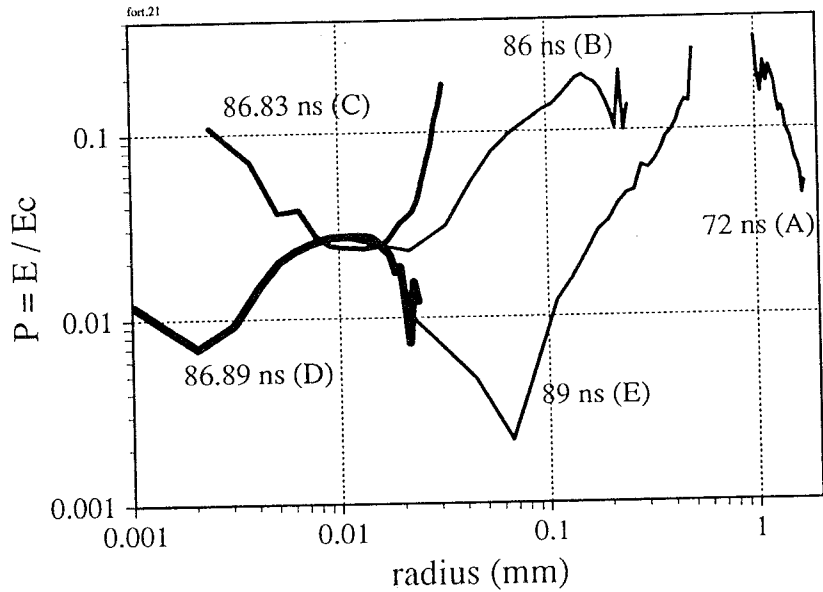
Figure 27. Ratio of electric field to the critical field for nonthermal electron creation as a function of radius for the times of Fig. 25.
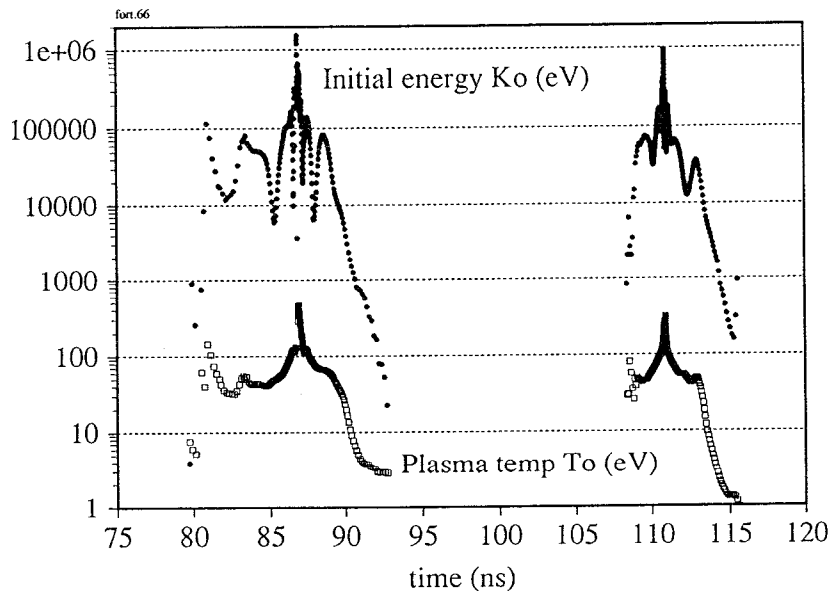
Figure 28. Axial plasma temperature and initial electron energy required for nonthermal creation as functions of time for the case of Fig. 24.

Though already insufficient for nonthermal electron production, the inductive electric fields calculated by HC must be considered to be upper limits when applied to Eqs. (10) - (12) for the following reason. The analysis of Appendix IV assumes that the scattering ion background is stationary in the frame in which the electrons experience the electric field. As indicated above, the major contribution to the field is the inductive $v \times B$ component associated with the plasma radial-mass-flow velocity. Because the ions move with this velocity, the local electric field in the ion rest frame is that due to resistivity only. The resistive portion of the electric field has been shown to be smaller than the inductive component away from the axis of symmetry (Fig. 25). The conclusion that the 1-D fields in the Saturn experiment are insufficient for nonthermal-electron production is therefore strengthened. The RHC computations described in Appendix II employ the above argument by using only the resistive electric-field components to conclude that the 1-D fields are insufficient for nonthermal production.

D. Two-Dimensional Effects

Irrespective of the analyses of Sec. IIIC, nonthermal radiation has been observed in the Saturn compact-array experiments, and the Gamble-II single-wire results demonstrate that such emission is associated with pinch-spot formation. It is therefore of interest to speculate on how multidimensional effects can enhance nonthermal electron production.

Two-dimensional, r-z RHC simulations were carried out for the 4-mg Saturn loads to supplement the 1D results and examine the structure of the pinch.[28] The computations finely resolved a small axial section of the pinch, and followed its development through the first compression to the start of the expansion phase. The primary results of these calculations are the nonlinear growth of the instability into the familiar bubble and spike formations, and a softening of the peak-compression phase caused by transport of magnetic flux to smaller radii as the bubbles fall through the fluid. The implosion dynamics, radial profiles, and predicted radiation characteristics are all similar to those of the 1D-RHC calculations. The dominant wavelength of the R-T instability, growing out of a 0.1% initial random density disturbance, was comparable to the diffusion length of the magnetic field as predicted by Roderick and Hussey.[38] In the RHC simulations, growth of the R-T stopped as the plasma began to expand while the sausage instability continued to grow.

At peak compression, the 2-D RHC calculations showed the development of dense, warm regions along the axis of symmetry with axial extents and diameters of about 100 μm (Fig. 2 of Ref. 28). When the radiation distribution from these density and temperature profiles was post-processed to produce a simulated pinhole image with the experimental resolution (Fig. 5 of Ref. 28), the image was close to the axial size and relative brightness of one of the smaller spots observed in the experiment (Fig. 4 of Ref. 28). Additionally, the several-hundred-μm spacings for the larger R-T structures in Fig. 2 of Ref. 28 are consistent with the smallest separations observed between pinch-spots in the Saturn loads (Fig. 14).

The 2-D RHC results are therefore consistent with the R-T instability providing a perturbation for the development of pinch spots in the Saturn loads with subsequent energy-

density concentration and coalescing of small spots provided by strong radiation processes and the nonlinear growth of the sausage instability.[15] The sausage instability is required to explain the larger, more intense spots observed, where the spot brightness relative to the surrounding regions is 10 to 10^2 (Fig. 14). It is unlikely that the R-T instability plays a dominant role in pinch-spot formation in the Gamble-II single-wire discharges, where annular implosions are not present and relative intensities of order 10^4 or larger have been observed.[7]

The observed 2-D pinch-spot structure allows larger electric fields to be generated than suggested by the 1-D simulations. In one dimension, the electric field is limited by the current that the generator can deliver to the load at peak compression. These simulations show current dipping to the 3-MA level (Figs. 21A and 24) as the electric-field achieves inductive electric fields of several-10's MV/cm (Fig. 25 and Eq. (9)). Because the strong L-dot loading occurs over the full 2-cm load length, the Saturn circuit model cannot provide sufficient voltage to sustain much larger electric fields. In two dimensions (and reality), where instabilities limit large radial compressions to small axial regions, the high-impedance and high-electric-field regions are limited to a small portion of the discharge length, and high currents can be maintained throughout the pinch. This effect has been characterized by a nonlinear, quasi-two-dimensional model for pinch-spot formation from the sausage instability in which local radiation collapse terminates when resistive heating balances optically-thick emission.[15] Results of this model indicate that inductive electric fields in the 100-MV/cm regime can be generated across the spots for discharges of interest. However, the model does not treat the radial MHD motion in a self-consistent manner for compact pinches, so that the 2-D electric fields derived from it are questionable.

In addition to nonthermal creation from 2-D instabilities, one can consider the development of 3-D asymmetries and turbulence. Compact-wire arrays have inherent three-dimensional asymmetries because individual wire plasmas exhibit MHD instabilities before merging into a single pinch. In such cases, electric fields can be generated parallel to the magnetic field so that nonthermal electron creation depends only on satisfying a condition similar to Eq. (11). This concept was crudely tested in 1-D RHC with the magnetic field set equal to zero in the nonthermal calculations described in Appendix II. These calculations showed that nonthermal electrons could be generated with modest electric fields in lower-density regions of the plasma in accordance with Eq. (11).

In addition to 2D-MHD instabilities, one can invoke micro-turbulence to support the existence of large inductive electric fields in lower-density regions of the plasma created by pinch-spot formation. If substantial current flows at low density, such that the electron drift speed exceeds its thermal velocity, two-stream turbulence can create high effective resistivity. The magnetic field can penetrate such regions without sweeping in the mass, leaving behind a stationary, resistive corona that can support electric fields induced by radial motion at smaller radius.[39] This mechanism provides a means of creating regions favorable to nonthermal-electron generation based on the analysis of Appendix IV. A similar mechanism, driven by the lower-hybrid instability[41] has recently been used in conjunction with RHC computations to explain a sharp improvement in Saturn gas-puff implosion quality due to

suppression of R-T modes by B-field-sheath thickening.[41] Though not yet studied in this context, stochastic electron-energy gain associated with micro-turbulence is a promising nonthermal-production mechanism.

E. Effects of Implosion Geometry on Nonthermal Electron Production

Although roughly six-times more current flowed through the Saturn compact arrays than through Gamble-II and Owl single-wire loads, comparable or lower nonthermal yields were recorded. Because the scaling of Saturn nonthermal yield with atomic-number and the tungsten spectra were similar to those observed with single wires, it is suggested that a common pinch-spot mechanism was the source of the nonthermal radiation in both cases. Thus, differences in pinch-spot formation between compact-imploding and single-wire loads are likely responsible for the disparity in nonthermal-radiation efficiencies (nonthermal yield divided by electrical energy delivered to the load).

Two major differences between the compact-imploding and single-wire geometries lead to differences in pinch-spot formation. The first is associated with the instabilities and azimuthal asymmetries that accompany the annular-implosion geometry. As indicated above, wire arrays develop azimuthal asymmetries when individual wire plasmas go MHD unstable before merging into a single pinch. Additional azimuthal asymmetries can be traced to the return-current geometry, differences in current carried by each wire, or small errors in wire location. These asymmetries create canonical angular momentum in the imploding array that limits the radial convergence.[42] A 10% initial azimuthal asymmetry in mass or current density can result in a maximum radial compression ratio of 10 to 15, limiting pinch spots to the observed range of 200- to 400-μm diameter for Saturn compact arrays. This mechanism may be responsible for the weaker, larger-radius, and more-irregular pinch spots formed in the Saturn loads as compared to those of Gamble-II single-wire tungsten loads. The growth of R-T instabilities in the Saturn imploding-load geometry, not present in single-wire discharges, can further limit radial convergence in pinch spots. The analyses and code computations discussed in Sec. IIIB indicate that spot compactness is directly related to the magnitude of induced electric fields and associated nonthermal radiation.

The second major difference between the compact-imploding and single-wire geometries is the inferred radial bouncing of the Saturn loads from the time-dependent oscillations in the x-ray output. This intrinsically 1D behavior, suggested from simple analysis and 1D-code simulation in Sec. IIIB, persists through several bounces even though the plasma structure is seen to be dominated by 2D instabilities. Indeed, the high compressions calculated in the 1D simulations are interpreted to be representative of the pinch spots, because the 2D calculations of spot formation in high-atomic-number pinches show little axial mass flow.[15,25] The larger flare structures between the spots are presumed to be due to the instabilities. Imposing the bounce dynamics on pinch spots may disrupt their development and limit their compression compared to those in single-wire discharges, where

no such periodic radial motion occurs. Dynamically interrupted spot compression may be responsible for further reduction of electric fields and the associated nonthermal radiation.

Although other differences such as driver impedance exist between the Gamble-II single-wire and the Saturn compact-array experiments, the two cited above that target the ability of the loads to create intense-pinch-spot-dominated plasmas are likely sufficient to explain the reduced nonthermal efficiency of the Saturn loads.

IV. Summary

Compact tungsten wire arrays, which have been studied for the first time in this experiment, exhibit multiple implosions as suggested by one-dimensional RHC and HC simulations. Aside from the observed axial bright spots at the time of implosion, soft radiation from these low-velocity implosions is well described in 1D. Two-dimensional RHC simulations show that the bright spots that are formed during the first implosion are due to the growth of the R-T instability, which leads to a bubble and spike phase. The bubble regions evolve into the bright spots, which corresponds to a region where the density and temperature are enhanced over the surrounding plasma regions. Although the 2D simulations were not run more than 5 ns past the time of the first implosion, the simulations indicate that as the plasma expands, the R-T instability shuts off, and the sausage instability begins to grow, which may lead to the subsequent, more intense bright spots seen later in time. Experimentally, a fraction of the evolved bright spots are observed to be the source of the warm x rays as observed in the Gamble-II single-wire experiments.

The thermal x-ray spectra measured between about 1 and 10 keV are in agreement with RHC simulations. Moreover, the implosion periodicities for various load masses calculated analytically and with RHC agree with those measured when the measured currents upstream of the load are assumed to flow in the pinch. This agreement with experiment gives credibility to the RHC radiation model.

Warm x rays from nonthermal processes are observed between 10 and 100 keV corresponding to a yield and efficiency of 35^{+35}_{-17} J and $\left(0.04^{+0.04}_{-0.02}\right)\%$, respectively. The similarity of the measured warm x-ray spectra and spatial structures to those measured at lower current on Gamble II suggest a common production mechanism for these processes. The lower production efficiency and the larger, more irregular pinch spots formed in this experiment relative to those measured on Gamble II, however, suggest that implosion geometrics are not as efficient as single exploding wire geometrics for warm x-ray production. These differences may arise from the instabilities, azimuthal asymmetries, and inferred radial bouncing that accompanies the annular implosion geometry.

Lastly, a model of electron acceleration across magnetic fields in a highly-collisional, high-atomic-number plasma has been developed, which shows the existence of a critical electric field below which strong nonthermal electron production does not occur. One-dimensional HC simulations show that a significant nonthermal electron population is not expected in this experiment because the calculated environmental electric fields are at least one to two orders-of-magnitude below the critical electric field. These negative nonthermal results are confirmed by RHC simulations using a nonthermal model based on a Fokker-Plank analysis.

References

1. T. W. L. Sanford, J. A. Halbleib, G. Cooperstein, and B. V. Weber, Sandia National Laboratory Technical Report, SAND95-0087 (August 95) and *IEEE Trans. Nucl. Sci.* **42**, 1902 (1995).

2. N. R. Pereira and J. Davis, *J. Appl. Phys.* **64**, R1 (1988).

3. D. D. Bloomquist, R. M. Stinnett, D. H. McDaniel, J. R. Lee, A. W. Sharpe, J. A. Halbleib, L. G. Shlitt, P. W. Spence, and P. Corcoran, *Proc. 6th IEEE Pulsed Power Conference* (Arlington, VA), ed. P. J. Turchi and B. H. Bernstein (IEEE, New York, 1987), p. 310.

4. D. Mosher, et al., *Ann. N. Y. Acad. Sci.* **25**, 632 (1975).

5. D. Mosher, et al., *Appl. Phys. Lett.* **23**, 429 (1973).

6. C. Stallings, K. Nielson, and R. Schneider, *Appl. Phys. Lett.* **29**, 404 (1976).

7. C. M. Dozier, et al., *J. Phys.* B10, L73 (1977).

8. D. J. Johnson, S. J. Stephanakis, and D. Mosher, NRL Memorandum Rep. 3207, 1976.

9. P. Spence (Pulse Sciences, Inc., San Leandro, CA), informal communication.

10. M. Krishnan (Alameda Applied Science Corp., San Leandro, CA) and R. B. Spielman (Sandia National Laboratories, Albuquerque, NM), informal communications.

11. D. A. Hammer, et al., *Appl. Phys. Lett.* **57**, 2083 (1990).

12. B. S. Fraenkel and J. L. Schwob, *Phys. Lett.* **40A**, 83 (1978).

13. W. Lochte-Holtgreven, *Atomkernenerie* **28**, 150 (1976).

14. C. Deeney, "Measurement of Hot Spots and Electron Beams in z-Pinch Devises," PhD. Thesis, Plasma Physics Group, Blackett Laboratory, Imperial College, London SW7, United Kingdom (April 1988).

15. D. Mosher and D. Colombant, *Phys. Rev. Lett.* **68**, 2600 (1992).

16. S. Maxon and T. Wainwright, *Phys. Fluids* **27**, 2535 (1984).

17. T. W. L. Sanford, D. R. Humphreys, J. W. Poukey, B. M. Marder, J. A. Halbleib, J. T. Crow, R. B. Spielman, and R. C. Mock, Sandia National Laboratories Technical Report, SAND94-0694 (June 1994).

18. B. L. Welch, H. R. Griem, and F. C. Young, *J. Appl. Phys.* **73**, 3163 (1993).

19. B. L. Welch, F. C. Young, and H. R. Griem, *J. Appl. Phys.* **74**, 2260 (1993).

20. T. W. L. Sanford, et al., *Bull. Am. Phys. Soc.* **40**, 1846 (1995).

21. M. L. Kiefer and M. M. Widner, *Digest of Tech. Papers 5th IEEE Pulsed Power Conf.* (Arlington, VA, 1985), M. F. Rose and P. J. Turchi, eds., p. 685.

22. T. W. L. Sanford, J. A. Halbleib, J. W. Poukey, C. E. Heath, and R. C. Mock, *Nucl. Instrum. Methods in Phys. Res.* **B34**, 347 (1988).

23. M. J. Clauser, L. Baker, D. H. McDaniel, R. W. Stinnett, and A. J. Toepfer, Sandia National Laboratories Report, SAND78-1387C (1978).

24. R. B. Spielman, *Rev. Sci. Instrum.* **66**, 867 (1995).

25. R. B. Spielman, et al., *Dense Z-Pinches 3rd Intl. Conf.*, London, United Kingdom, 1993; *AIP Conference Proceedings* **299**, ed. M. Haines and A. Kneight (AIP Press, New York, 1994), p. 404.

26. D. Mosher and D. Colombant, *Dense Z-Pinches*, N. R. Pereira, J. Davis, and N. Rostoker, eds., AIP Conf. Proc. 195 (AIP, New York, 1989), p. 191.

27. K. G. Whitney, et al., *J. Appl. Phys.* **67**, 1725 (1990).

28. S. Maxon, J. H. Hammer, J. L. Eddleman, M. Tabak, G. B. Zimmerman, W. E. Alley, K. G. Esterbrook, J. A. Harte, T. J. Nash, T. W. L. Sanford, and J. S. De Groot, LLNL Rep. UCRL-JC-120752 (April 1995).

29. D. E. Post, et al., *Atomic Data and Nuclear Data Tables* **20**, 397 (1977).

30. B. A. Hammel and L. A. Jones, *Appl. Phys. Lett.* **44**, 667 (1984).

31. D. R. Kania and L. A. Jones, *Phys. Rev. Lett.* **53**, 166 (1984).

32. J. D. Hares, R. E. Marrs, and R. J. Fornter, *J. Phys. D-Appl. Phys.* **18**, 627 (1985).

33. J. Fukai and E. J. Clothiaux, *Phys. Rev. Lett.* **34**, 863 (1975).

34. V. V. Vikhrev, V. V. Ivanov, and K. N. Koshelev, *Sov. J. Plasma Phys.* **8**, 688 (1982).

35. D. Mosher, *Phys. Fluids* **18**, 846 (1975).

36. D. R. Welch, C. L. Olson, and T. W. L. Sanford, *Phys. Plasmas* **1**, 768 (1994).

37. H. Dreicer, *Phys. Rev.* **115**, 238 (1959).

38. N. F. Roderick and T. W. Hussey, *J. Appl. Phys.* **59**, 662 (1986).

39. R. C. Davidson and N. A. Krall, *Nucl. Fusion* **17**, 6 (1977).

40. A. B. Mikhailovskii, Chapter 13 in *Theory of Plasma Instabilities, Volume 1: Instabilities in a Homogeneous Plasma*, (Consultants Bureau, New York, 1974).

41. J. S. De Groot, "Effective Collision Frequency Due to the Lower Hybrid Instability," UC Davis Report, PGR-M-240, March 13, 1995.

42. D. Mosher, *Proc. 10th Intl. Conf. on High Power Particle Beams* (San Diego, CA, June 1994), R. White and W. Rix, eds., p. 159, NTIS PB95-144317.

Appendix I

Filter Fluorescer Spectrometer

In order to determine the spectrum of photons of energies greater than 10 keV, an instrument that has good efficiency and a high degree of background rejection is needed. The use of heavily filtered detectors is complicated by the necessity of correcting for backgrounds over a wide energy domain extending from about 10 keV up to hundreds of keV. Generally, this implies that both the detector and the filter response be well characterized over this entire interval. While predicting the energy response of a given filter over this region presents no extreme difficulty, the determination of a given detector response over such a large energy interval is a formidable task.

The filter fluorescer technique was developed to minimize these problems. This technique relies on the well understood fluorescence of a given material over this energy interval. Instead of exposing the detector directly to the radiation source, the detector views a fluorescer, which is exposed to the filtered radiation of the source. The detector then responds to fluorescence and whatever scattering occurs. The amplitude and spectrum of this secondary radiation can be accurately predicted for any given incident spectrum and combination of filters and fluorescers. By choosing the proper filter fluorescer pairs, the response of a particular detector may be limited to a narrow band of energy. The primary advantage of this technique is that this measurement requires that the detector be calibrated at this single photon energy.

For this experiment, sixteen pairs of channels were designed to give contiguous non-overlapping coverage from 10 keV to 100 keV with a sensitivity optimized to measure an emission of about one kilojoule per energy band and a limit of detectability of about a joule per channel. This sensitivity was accomplished by using a two-dimensional focusing microchannel plate for the photon detector. This design not only allowed for all sixteen channels to be integrated into one 20-cm by 12-cm by 12-cm instrument, but also allowed a considerable variation in sensitivity by adjusting the microchannel plate (MCP) gain. Figure A1 shows the geometry of this instrument. Figure A2 details the post-MCP electron beam focusing to increase the sensitivity of each channel.

In the experiment, the z-pinch hard x-ray yield was several orders of magnitude lower than anticipated, resulting in channel energies of a few joules instead of the anticipated kilojoules—see Figure 18. Therefore, it was necessary to field modify the instrument to increase its sensitivity by an order of magnitude. This increase was accomplished by changing both the geometry and the width of the energy bands. The final configuration consisted of four filter fluorescer channels arranged in pairs to cover from 10 to 20 keV and from 20 to 30 keV. The responses of these four channels are shown in Fig. A3.
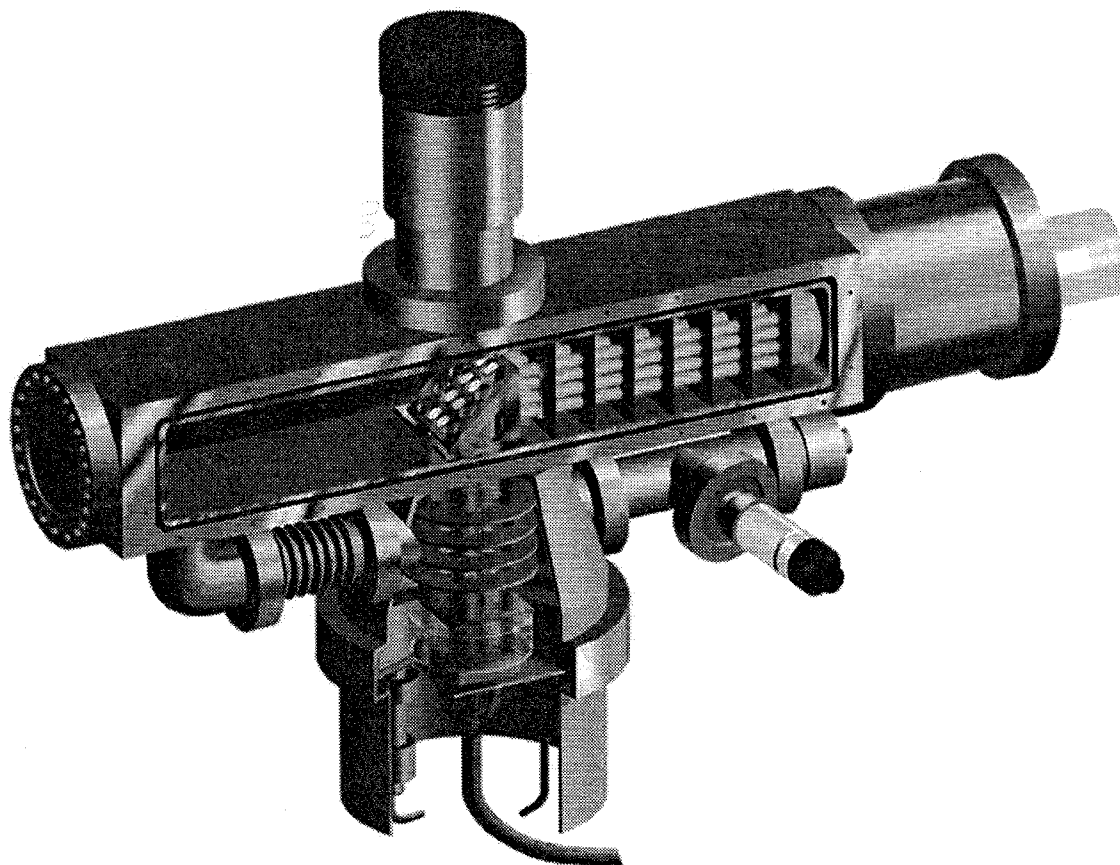
Figure A1. Drawing of the filter fluorescer as fielded. The incident beam is from the right and is collimated by the collimator stack shown. The fluorescers are at 45 degrees to both the incident beam and the detector. The filters are located both before the fluorescer and after the fluorescer.

X-RAY BEAM

MCP

ELECTRON BEAM

LENS

FIBER-OPTIC FACE PLATE
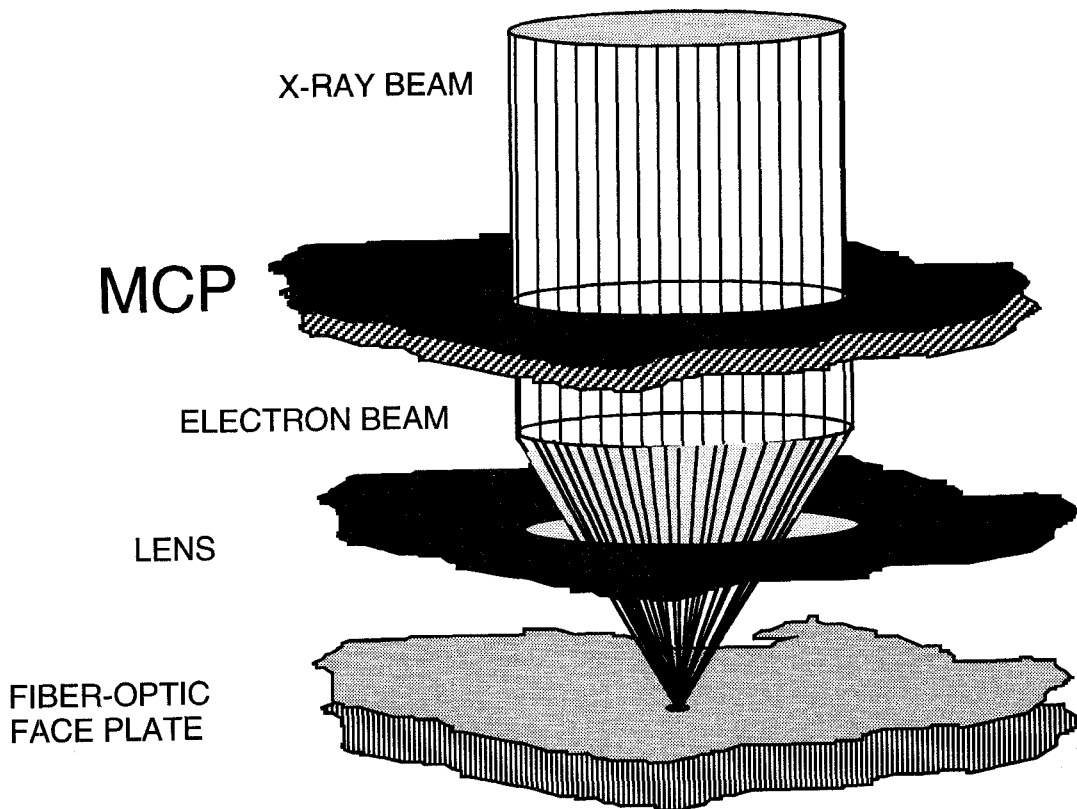
FILTER-FLUORESCER DETECTOR

Figure A2. Focusing electro-optic used to amplify the output of the microchannel plate x-ray detector.
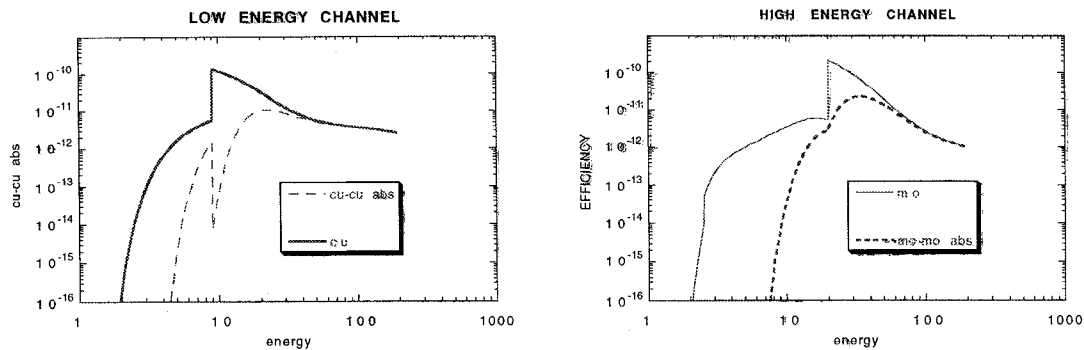
Figure A3. Filter fluorescer response curves.

In each figure, the solid curve is the response of a filtered fluorescer; the dotted curve has an additional filter to absorb the fluorescent radiation. This channel then, is a measurement of the broad band high energy scattered radiation. Subtraction of these two channels gives the channel response due to only fluorescent radiation where the detectors' response has been well calibrated. Such a subtraction requires limited scattering, otherwise the error propagation due to subtraction of two numbers of similar magnitude negates the advantages of this technique. Upon analysis of the data, we discovered that the extended knee, which appears in the unfiltered high-energy channel at a photon energy of about 2.5 keV when convolved with the steeply falling power law spectrum of Fig. 18, produced a bimodal response peaked at energy of about 5 keV and 25 keV. This bimodal response function was dependent in a nonlinear way upon the incident spectrum and made interpretation of the data obtained with this channel difficult. For this reason, the channel was ignored for most of the data analysis and does not appear in Table I or Fig. 18.

In Fig. 15 the agreement of the curve 5.5 - 9 keV FFA yield (Fig. 15F) —which was obtained by a further modification to the filter arrangement—with the 5-9 keV PCD yield (Fig. 15E) demonstrates the usefulness of this technique. It should be noted that these curves were **not** normalized to each other in any way, yet, not only are the relative amplitudes generally similar, but the absolute magnitudes are also in rough agreement, giving confidence in the overall calibration of the detectors.

Appendix II

Radiation-Hydro Code

The code RHC[1] solves the equations

$$\rho\left(\frac{\partial}{\partial t}+\mathbf{V}\cdot\nabla\right)\mathbf{V}+\nabla(P+Q)=\frac{\mathbf{J}\times\mathbf{B}}{c},\tag{1}$$

$$\frac{3}{2}n_i\left(\frac{\partial}{\partial t}+\mathbf{V}\cdot\nabla\right)kT_i+(P_i+Q)\nabla\cdot\mathbf{V}+\nabla\cdot\boldsymbol{q}_i=k(T_e-T_i)\frac{n_i}{\tau_{e-i}}\tag{2}$$

$$\rho\frac{\partial\varepsilon_e}{\partial T_e}\left(\frac{\partial}{\partial t}+\mathbf{V}\cdot\nabla\right)T_e+P_e(\nabla\cdot\mathbf{V})-\rho^2\frac{\partial\varepsilon_e}{\partial\rho}(\nabla\cdot\mathbf{V})+\nabla\cdot\boldsymbol{q}_e=k(T_e-T_i)\frac{n_i}{\tau_{e-i}}$$

$$=\frac{k(T_i-T_e)n_i}{\tau_{ei}}+\eta J^2+4\pi c\rho\int_0^\infty dv\left(\kappa_v U_v-e_v\right)\tag{3}$$

$$\frac{\partial}{\partial t}U_v+\nabla\cdot q_v=c\rho\left(e_v-\kappa_v U_v\right),\tag{4}$$

where ρ, $\mathbf{V}$, T_e, T_i, k, η, κ_v, e_v, and q_v are the density, fluid velocity, electron temperature, ion temperature, Boltzmann's constant, resistivity, frequency-dependent opacity, frequency-dependent emissivity, and frequency-dependent radiation energy flux in cgs units. P is the total pressure (electron + ion) and Q is the artificial viscosity. $n_{e(i)}$ is the electron (ion) particle density and $\tau_{e\cdot i}$ is the ion-electron relaxation time.[2] The quantity ε_e is the specific electron energy, ηJ^2 is the Joule heating term (magnetic diffusion), and the third term on the right-hand side of Eq. (3) is the net energy transfer from the radiation field to the electron. Thermo-electric terms have been dropped. The quantity e_v is defined so that $4\pi c\rho e_v$ is the energy radiated per unit time per unit frequency from line emission, recombination, and bremsstrahlung.

The electron and (ion) heat flux are given by

$$\mathbf{q}^{e(i)}=-\kappa_{||}^{e(i)}\nabla_{||}\left(kT^{e(i)}\right)-\kappa_\perp^{e(i)}\nabla_\perp\left(kT^{e(i)}\right)\tag{5}$$

where $\kappa_{||}$ and $\kappa_\perp$ are the conductivities parallel and perpendicular to the magnetic field, while the radiation flux is given by

$$\boldsymbol{q}_v=-\frac{(c/3)\nabla U_v}{\max\left[\rho\kappa_v,2/3(|\nabla U_v|/U_v)\right]}\tag{6}$$

where U_v is the frequency-dependent radiation energy density and κ_v is the frequency dependent opacity.

The above equations are solved together with Maxwell's equation

$$\nabla \times \mathbf{B} = \frac{4\pi}{c}\mathbf{J},$$ (7)

$$\nabla \times \mathbf{E} = -\frac{1}{c}\frac{\partial}{\partial t}\mathbf{B},$$ (8)

where $\mathbf{E}$ obeys the simple Ohm Law.

For the calculations reported here, a modified suprathermal electron package was included in the computations. The suprathermal package models the production and acceleration of suprathermal electrons across the azimuthal magnetic field by the electric field generated to drive the axial current in the z-pinch. In the superthermal calculations, the plasma is treated as highly collisional so the electron distribution function is represented by the first two terms in a spherical harmonic expansion, $f = f_0 + \mu f_1$, where $\mu = \cos\theta$, and θ is the polar angle, i.e., the angle between the z-axis and the velocity vector. This approximation is substituted into the Fokker-Planck equation for electron-ion collisions. The resultant equation is averaged over the polar angle to obtain an equation for the time evolution of the isotropic component of the electron distribution function:

$$\frac{\partial f_{e0}}{\partial t} = \frac{e^2}{3m^2}\frac{1}{v^2}\frac{\partial}{\partial v}\left[v^2\tau(v)\left(\frac{E_\perp^2}{1+\omega_{ce}^2\tau^2(v)}+E_\parallel^2\right)\frac{\partial f_{e0}}{\partial v}\right] - \frac{\partial f_{e0}}{\partial t}\bigg|_{e-e\ drag\ term:}$$

where ω_{ce} is the electron cyclotron frequency. The electric field in the ion rest frame, $E_\perp$, is determined from the distribution function. The velocity dependent current density is $\bar{j}_\perp(v)$. The boundary condition that applies is that the radial current is zero. This condition results in the radial electric field required to maintain the zero radial current

$$\bar{j}_\perp(v) = \frac{4\pi}{3}\frac{e^2}{m}\frac{v^3\tau(v)}{1+\omega_{ce}^2\tau^2(v)}\frac{\partial f_{e0}}{\partial v}\left[-\vec{E}_\perp + \omega_{ce}\tau(v)\hat{B}\times\vec{E}_\perp\right].$$

Integrating this equation over velocity, we obtain the electric field perpendicular to the magnetic field in terms of the current density perpendicular to the magnetic field:

$$\vec{E}_\perp = \frac{-\bar{j}_\perp(v)-\eta\hat{B}\times\bar{j}_\perp(v)}{\frac{4\pi}{3}\frac{e^2}{m}(1+\eta^2)\left\{\int_0^\infty \frac{v^3\tau(v)}{1+\omega_{ce}^2\tau^2(v)}\frac{\partial f_{e0}}{\partial v}dv\right\}}$$

where

$$\eta = \frac{\displaystyle\int_0^\infty \frac{v^3\tau(v)}{1+\omega_{ce}^2\tau^2(v)}\, \omega_{ce}\tau(v)\frac{\partial f_{e0}}{\partial v}\, dv}{\displaystyle\int_0^\infty \frac{v^3\tau(v)}{1+\omega_{ce}^2\tau^2(v)}\frac{\partial f_{e0}}{\partial v}\, dv} \; .$$

RHC[3] was used to perform 1D and 2D calculations of the tungsten wire implosion on Saturn. The initial conditions correspond to various masses of tungsten, and selected aluminum and copper masses, at an initial radius of r = 2 mm, annular width Δr = 80 mm, and length 2 cm, driven by the Saturn accelerator,[4] with a peak current ~ 5-6 MA and a rise time ~ 70 ns. The external circuit in RHC solves for the current with voltage pattern (Fig. 2B), initial inductance, and resistance taken from experiment (Fig. 3). Equations (1)-(8) are solved in both 1D and 2D (r,z). We assume rotation symmetry about the z axis. The relevant 2D calculations are described in Ref. 5.

References

1. G. B. Zimmerman, LLNL Rep. UCRL-74811 (1973); P. D. Nelson and G. B. Zimmerman, LLNL Rep. UCRL-53127 (1981).

2. L. Spitzer, Jr., *Physics of Fully Ionized Gases* (Interscience, New York, 1962).

3. S. Maxon and T. Wainwright, *Phys. Fluids* **27**, 2535 (1984).

4. T. W. L. Sanford, et al., Sandia National Laboratories Technical Report, SAND94-0694, 1994.

5. S. Maxon, et al., LLNL Rep. UCRL-JC-120752, April 1995, submitted for publication.

Appendix III

Numerical Simulation of a Z-Pinch in Cylindrical Coordinates with a MHD PIC Code

A particle-in-cell (PIC) MHD code with crude radiation transport HC is used to investigate the one and two dimensional dynamics of the z-pinch. Particular attention is paid to sheath physics and electron runaway. PIC codes are useful because of their sub-grid resolution and intuitive nature.

1. MHD Equations

The governing MHD equations[1] in MKS units are:

$$\frac{\partial \rho}{\partial t} + \nabla \bullet \rho \mathbf{v} = 0 \tag{1}$$

$$\rho \frac{d\mathbf{v}}{dt} = -\nabla \left(p + \frac{\varepsilon \rho}{3} \right) + \mathbf{J} \times \mathbf{B} \tag{2}$$

$$\rho \frac{de}{dt} = \frac{p}{\rho}\frac{d\rho}{dt} + \frac{\mathbf{J}^2}{\sigma} + \nabla \bullet \kappa \nabla T - P_{rad} \tag{3}$$

$$\rho \frac{d\varepsilon}{dt} = \frac{\varepsilon}{3}\frac{d\rho}{dt} + \nabla \bullet \frac{c}{3\lambda} \nabla(\rho\varepsilon) + P_{rad} \tag{4}$$

$$\mathbf{E} + \mathbf{v} \times \mathbf{B} = \frac{\mathbf{J}}{\sigma} \tag{5}$$

$$\frac{\partial \mathbf{B}}{\partial t} = -\nabla \times \mathbf{E} \tag{6}$$

$$\nabla \times \mathbf{B} = \mu \mathbf{J} \tag{7}$$

$$T = T(e), \quad p = p(\rho,e), \quad \kappa = \kappa(\rho,e), \quad \sigma = \sigma(\rho,e), \tag{8}$$

$$Z = Z(\rho,e), \quad \lambda = \lambda(\rho,e), \quad P_{rad} = P_{rad}(\rho,e,\varepsilon)$$

where ρ is the mass density, $\mathbf{v}$ is the velocity, $\mathbf{B}$ and $\mathbf{E}$ are the magnetic and electric fields, $\mathbf{J}$ is the current density, e is the specific fluid internal energy (energy per unit mass), ε is the specific radiation energy density, p is the fluid pressure, T is the plasma temperature, κ is the thermal conductivity, σ is the electrical conductivity, Z is the ionization state, and λ is an average photon

mean free path. P_{rad} is the radiative power production per unit volume. Viscosity and the additional "Hall" terms in (5) are negligible for the parameter range of interest and are not included. μ is the free space permeability and c is the speed of light.

Let θ be the temperature in electron volts, $\theta = T/11600$. An ionized plasma ideal gas approximation is used for the fluid pressure,

$$p = (1+Z)nkT = (1+Z(\theta))\rho\theta\left\{\frac{11600k}{m_p}\right\}\frac{Nt}{m^2} \tag{9}$$

where m_p is the proton mass. The heat conduction and resistivity are from Spitzer.[2] The transport coefficients become

$$\kappa(\theta) = 1.95 \times 10^{-9}\frac{T^{\frac{5}{2}}}{Z\ln\Lambda} = \frac{28\theta^{\frac{5}{2}}}{Z(\theta)\ln\Lambda}\quad\frac{Joules}{sec\ m\ K} \tag{10}$$

$$\sigma(\theta) = \frac{T^{\frac{3}{2}}}{38Z\ln\Lambda} = \frac{\theta^{\frac{3}{2}}}{3.0 \times 10^{-5}Z(\theta)\ln\Lambda}\quad\frac{mho}{m}. \tag{11}$$

Both are independent of density. The Coulomb logarithm, $\ln\Lambda$, is taken to be one.

The photon mean free path, λ, needed for the radiation diffusion, depends on the photon energy as well as on temperature and density. The code does not use spectral information in its treatment of radiation production and diffusion. The average mean free path used in the diffusion equation (4) is approximated by

$$\lambda = \frac{C_R}{\rho^2}\ m\ . \tag{12}$$

For tungsten, $C_R \approx 0.1$ is a reasonable approximation for photons in the range 1 - 100 ev. Its temperature dependence is considerably weaker than that of the density for plasmas below about a keV. This radiation production and transport model is clearly an empirical approach which does not accurately reflect the physics. It does, however, give reasonably close agreement in one dimensional runs with codes, such as PHC[3], that do. The ionization state, $Z(\theta)$, is given as a function of temperature. The specific heat relates the internal energy to the temperature by

$$e(\theta) = \frac{9.6 \times 10^7}{A}S(\theta)\theta\quad\frac{J}{kg} \tag{13}$$

where A is the atomic number. The continuum radiation power generation is

70

$$P_{cont} = 5.4 \times 10^{15} \left(\frac{\rho}{A}\right)^2 \theta^{\frac{1}{2}} Z(\theta)\beta(\theta) \; \frac{Watts}{m^3} \tag{14}$$

while that for line radiation is

$$P_{line} = 1.26 \times 10^{23} \left(\frac{\rho}{A}\right)^2 \theta^{-\frac{1}{2}} z(\theta)\psi(\theta) \; \frac{Watts}{m^3} \; . \tag{15}$$

Both are averaged over all photon energies. The functions Z, S, β and ψ, are plotted in Fig. 1 and are interpolated by the code from tabulation of coronal equilibrium calculations.[4] These functions are for optically thin plasmas, which do not interact with the background radiation field.

To account for the presence of radiation energy density in the plasma in an ad hoc manner, P_{cont} and P_{line} are multiplied by a factor which is unity when there is no background radiation but which vanishes when the radiation energy density equals the plasma energy density. The total radiation power production is then

$$P_{rad} = (P_{line} + P_{cont})\left(\frac{e - \varepsilon}{e}\right) \; . \tag{16}$$

The current is computed from a circuit equation containing a voltage source (Fig. 2B), external resistance and inductance (Fig. 3), and plasma resistance and inductance. The plasma inductance is obtained from the plasma radius. Its resistance is derived from the integrated J^2/σ heating in the plasma.

2. The Numerical Algorithm

The above set of equations are solved in cylindrical (z,r) coordinates using a fluid particle-in-cell (PIC) technique in which the "particles" represent elements of fluid in that they mark its location and carry its properties.[5] The grid is used to store ensemble averages of particle quantities. Particle quantities will be labeled with "i", while grid quantities will carry the labels "L" and/or "M", corresponding to the underlying spatial variables. The following quantities are assigned to particles: mass, position, density, velocity, specific internal energy, specific radiation energy, and magnetic field. These are denoted by

$$m(i), z(i), r(i), \rho(i), v(i), e(i), \varepsilon(i), b(i)$$

The particle index, i, will be omitted when there is no danger of confusion. The magnetic field has only an azimuthal component. Because kinematic information, two thermodynamic quantities (ρ and e), and the radiation energy and magnetic field are carried by the particles, they
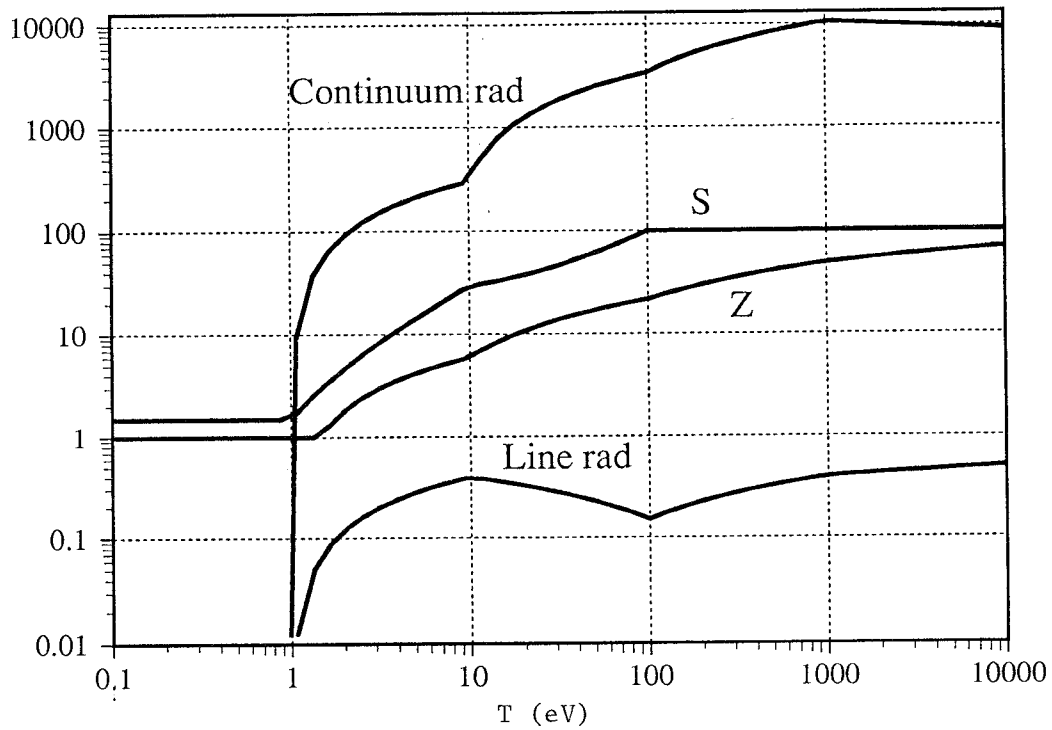
Figure 1.   Ionization level, $Z(\theta)$, specific heat function, $S(\theta)$, continuum and line radiation
power functions, $\beta(\theta)$ and $\psi(\theta)$, vs. temperature in eV.

contain all the information needed to characterize the current state of the system and predict its dynamic behavior. The grid is simply an overlay that is redefined when needed as the plasma moves. With all particle quantities known at a time step, the algorithm proceeds as follows. To insure that the Courant stability condition is not violated, a time step is determined from the maximum particle value of the combined sound-Alfven-fluid speed. New particle locations are found from the velocity in the usual manner.

The grid is constructed to be slightly larger than the fluid so that only a few vacuum cells surround it. In general, for cylindrical coordinates only the radius need change as the plasma contracts or expands. It is not necessary to change the underlying grid every time step, only when the plasma conditions warrant it. The density on grid vertices is computed by summing the area weighted mass in the surrounding four cells divided by the effective vertex volume:

$$\rho(L, M) = \frac{\sum_i m(i)\delta(i, L, M)}{Vol(L, M)} \quad . \tag{17}$$

Here, $\delta(i,L,M)$ represents the bi-linear area-weighting factor used to apportion particle variables to the grid. The volume in cylindrical coordinates it is $2\pi r(M)\Delta z\Delta r$. Vertices at boundaries and at the origin have smaller volumes. New particle densities, $\rho(i)$, are then interpolated from the grid by area weighting. Along with the density, grid velocity, specific energy, radiative energy, and magnetic field are defined on the grid in such a manner as to conserve a particular quantity were every particle to be given its interpolated value:

$$v(L, M) = \frac{\sum m v \delta}{\sum m \delta}, \quad e(L, M) = \frac{\sum m e \delta}{\sum m \delta}, \quad \varepsilon(L, M) = \frac{\sum m \varepsilon \delta}{\sum m \delta}, \quad b(L, M) = \frac{\sum \frac{m b \delta}{r\rho}}{\sum \frac{m \delta}{r\rho}} \quad . \tag{18}$$

The first of these conserves momentum, although it should be noted that radial momentum is not necessarily conserved since, by symmetry, the total radial momentum for a concentric hoop is always zero. The second two conserve internal and radiative energy, and the last conserves magnetic flux, b x area.

3. Diffusion and Transport

Diffusion and transport are handled in two separate steps. (2), (3) and (4)-(7) can be written in the form

$$\rho\frac{de}{dt} = -\rho p(\rho, e)\frac{d}{dt}\left(\frac{1}{\rho}\right) + \nabla\bullet\kappa\nabla T \tag{19}$$

$$\rho^{\frac{1}{3}}\frac{d}{dt}\left(\frac{\varepsilon}{\rho^{1/3}}\right) = \nabla \bullet \frac{c}{3\lambda}\nabla(\iota \qquad (20)$$

$$r\rho\frac{d}{dt}\left(\frac{b}{r\rho}\right) = \frac{1}{\mu}\left[\frac{\partial}{\partial z}\frac{1}{\sigma}\frac{\partial b}{\partial z} + \frac{\partial}{\partial r}\frac{1}{(r\sigma)}\frac{\partial}{\partial r}(rb)\right] \qquad (21)$$

The advective part of these three equations is handled by the particles as follows:

$$e_{new} = e_{old} - p\left(\frac{1}{\rho_{new}} - \frac{1}{\rho_{old}}\right), \quad \frac{\varepsilon_{new}}{\varepsilon_{old}} = \left(\frac{\rho_{new}}{\rho_{old}}\right)^{\frac{1}{3}}, \quad \frac{b_{new}}{b_{old}} = \left(\frac{r_{new}\rho_{new}}{r_{old}\rho_{old}}\right) \qquad (22)$$

That is, as the particles' density and radius change, these quantities are altered accordingly. Notice that if the pressure is a function of e and ρ, as it is in a regular fluid, the internal energy equation can also be integrated analytically. For a plasma, some of the internal energy goes into ionization and has no effect on the pressure.

The diffusion part is handled separately by solving the partial differential equations.

$$\rho\frac{\partial e}{\partial t} = \nabla \bullet \kappa \nabla T \qquad (23)$$

$$\rho\frac{\partial \varepsilon}{\partial t} = \nabla \bullet \frac{c}{3\lambda}\nabla(\rho\varepsilon) \qquad (24)$$

$$\mu\frac{\partial b}{\partial t} = \frac{\partial}{\partial z}\frac{1}{\sigma}\frac{\partial b}{\partial z} + \frac{\partial}{\partial r}\frac{1}{(r\sigma)}\frac{\partial}{\partial r}(rb) \qquad (25)$$

Notice that these contain the partial time derivative, the advective part of the total time derivative having already been handled by the particle movement. These are solved iteratively in the plasma with a successive over-relaxation algorithm as follows. For the internal energy, the normal derivative vanishes at the plasma surface since energy is neither lost nor gained by this diffusion. This is accomplished at the irregular, constantly changing surface by defining the specific energy in the adjacent vacuum cells by

$$e(L, M) = \frac{\sum e(L^*, M^*)\rho(L^*, M^*)}{\sum \rho(L^*, M^*)} \qquad (26)$$

where * indicates the four points of a cross centered on (L,M). Where the denominator vanishes, there is no need to define the energy since it does not influence the computation. Where it does

74

not vanish, that is along the plasma border, the vacuum energy is the weighted average of neighboring energies. In general, only one of these densities will be non-zero, giving the desired zero normal derivative. The radiation energy escapes at the plasma-vacuum boundary so it is set equal to zero there. The magnetic field is $\mu I / 2\pi r$ at the outer plasma boundary, and zero the inner boundary, should there be one.

Even if there were no transport, the act of distributing the particle quantities to the grid and then returning them via area weighting would introduce numerical diffusion into the code. The transport equation (19), (20), and (21) are, therefore, used only to compute the time derivatives of the respective quantities. Using the magnetic field for illustration, particle quantities are updated by

$$b = b_{old} + \frac{\partial b}{\partial t}(L, M)\Delta t \ , \tag{27}$$

where the time derivative is interpolated to the particle location. By doing this, only the incremental change, proportional to Δt, is communicated back to the particles. When this is zero, no numerical diffusion occurs.

At each step some of the particle internal energy is converted into radiative energy:

$$\frac{d}{dt}(e - \varepsilon) = -\frac{2P}{\rho}\left(\frac{e - \varepsilon}{e}\right) \ . \tag{28}$$

The solution to this equation is approximated numerically by

$$e - \varepsilon = (e_{old} - \varepsilon_{old})e^{-\frac{2P\Delta t}{\rho e}} \ , \tag{29}$$

where the old values are used in the exponent. This equation, together with

$$e + \varepsilon = e_{old} + \varepsilon_{old} \tag{30}$$

gives the new energies. If the particle radiative energy ever exceeds the internal, the code transfers energy to equilibrate the two.

The GAP[6] numerical smoothing algorithm is used to handle shocks and control particle scatter.

References

1. Shih-I Pai, *Magnetogasdynamics and Plasma Dynamics* (Prentice Hall/Springer-Verlag, Englewood Cliffs, NJ, 1962).

2. Lyman Spitzer, Jr., *Physics of Fully Ionized Gases* (Interscience Publishers, NY, 1967).

3. S. Maxon, et al., LLNL Rep. UCRL-JC-120752, April 1995, submitted for publication.

4. D. Mosher, *Phys. Rev A* **10,** (1974) 2330.

5. F. H. Harlow, *Meth. Comp. Phys.* **3,** (1963) 319.

6. B. M. Marder, *Math. of Comput.* **29,** (1975) 473.

Appendix IV

Nonthermal Electron Energy Gain Modeling

The starting point for this analysis is a set of relativistic electron fluid equations appropriate for collision-dominated flows in high-atomic-number plasmas.[1] Constant axial-electric and azimuthal-magnetic fields are assumed in an unbounded, uniform, and stationary plasma, and the variations of nonthermal-electron fluid velocity v and average nonthermal-electron energy K are followed in time. In the nonrelativistic limit, $\vec{\beta} = v/c \ll 1$ and $\Gamma = K/mc^2 \ll 1$, where c is the velocity of light, and m is the electron rest mass. These nondimensional variables evolve according to

$$\frac{d\vec{\beta}}{dt} + \frac{e\mathbf{E}}{mc} + \frac{e\vec{\beta} \times \mathbf{B}}{m} = -\frac{\Omega_s \vec{\beta}}{(2\Gamma)^{3/2}} \quad , \tag{1}$$

$$\frac{d\Gamma}{dt} + \frac{e\mathbf{E} \cdot \vec{\beta}}{mc} = -\frac{\varepsilon \Omega_s}{(2\Gamma)^{1/2}} \quad . \tag{2}$$

In these equations, $\Omega_s = 4\pi n_i r_0^2 c(\alpha_i + 2\alpha_e)$ is a characteristic scattering frequency for mildly relativistic ($\Gamma = 0.5$) electrons, r_0 is the classical electron radius, and α_i and α_e are the collision contributions made by plasma ions and electrons. The α values, calculated by averaging over beam-electron scattering angles, are given by[1]

$$\alpha_i = Z_A^2 \ln\left(\frac{2K}{I_z}\right) + Z^2 \ln\left(\frac{\lambda_D}{Zr_0}\frac{I_z}{mc^2}\right) \quad ,$$

$$\alpha_e = Z_A \ln\left(\frac{\sqrt{2}K}{I_z}\right) + Z \ln\left(\frac{\lambda_D}{2r_0}\frac{I_z}{mc^2}\right) \quad . \tag{3}$$

In Eq. (3), Z_A is the atomic number, I_z is the ionization potential of the Z-times ionized plasma, and λ_D is the plasma Debye length.

The quantity ε in Eq. (2) is given by $\varepsilon = \alpha_e / (\alpha_i + 2\alpha_e)$. As a general rule-of-thumb for dense, high-atomic-number plasmas, these quantities can be estimated from[1] $\alpha_i \approx Z^2 \ln\Lambda(K)$ and $\alpha_e \approx Z\ln\Lambda(K)$, where $\ln\Lambda$ is about 10 for low-energy beam electrons and increases slowly with K. Using these approximate forms for α_i and α_e leads to $\varepsilon = 1/(Z + 2)$. For the tungsten plasmas of interest, these approximations lead to $\Omega_s \approx 4 \times 10^{-10} n_i$ s^{-1}, and $\varepsilon \approx 1/40$ using either Eq. (3) or the approximate forms. Note that the scattering frequency, defined as

$$\nu_s = \Omega_s / (2\Gamma)^{3/2} \tag{4}$$

by Eq. (1), is much greater than Ω_s. For electron energies characterized by plasma temperatures in the 100-eV to 1-keV regime, v_s is of order $(10^4 - 10^5)\,\Omega_s$, which is larger than Ω_c for z-pinch parameters of interest. The energy lose rate is defined by Eq. (2) as

$$v_e = 2^{1/2}\,\varepsilon\Omega_s \,/\, (2\Gamma)^{3/2} = 2^{1/2}\,\varepsilon v_s \approx 2^{1/2}\,v_s \,/\,(Z+2) \quad , \tag{5}$$

so that electron scattering occurs on a faster time scale than energy loss in very-high-atomic-number plasmas.

These different time scales for scattering and energy loss differentiate collision processes in high-atomic number plasmas from those in hydrogenic plasmas and simplify solution of Eqs. (1) and (2). For a cartesian coordinate system with $\mathbf{E}$ along z and $\mathbf{B}$ along y, the equations can be written

$$\frac{d\beta_x}{d\tau} - \left(\frac{\Omega_c}{\Omega_s}\right)\beta_z = -\frac{\beta_x}{(2\Gamma)^{3/2}} \quad , \tag{6}$$

$$\frac{d\beta_z}{d\tau} + \left(\frac{\Omega_c}{\Omega_s}\right)\beta_x = \mathcal{E} - \frac{\beta_z}{(2\Gamma)^{3/2}} \quad , \tag{7}$$

$$\frac{d\Gamma}{d\tau} = \mathcal{E}\beta_z - \frac{\varepsilon}{(2\Gamma)^{1/2}} \quad , \tag{8}$$

where $\tau = \Omega_s t$ and $\mathcal{E} = -eE_z/mc\,\Omega_s$. The equation for β_y shows exponential decay to zero on the v_s^{-1} time scale and need not be considered further.

Because of the rapid collisional relaxation of fluid velocity compared to that of energy, $d\vec{\beta}/dt$ approaches zero on the time scale over which Γ varies. Following the decay of initial transients, this quasistatic variation in $\vec{\beta}$ takes the form

$$\beta_x = (2\Gamma)^{3/2}\left(\frac{\Omega_c}{\Omega_s}\right)\beta_z \quad ; \quad \beta_z = \mathcal{E}\left[\left(\frac{\Omega_c}{\Omega_s}\right)^2 (2\Gamma)^{3/2} + \frac{1}{(2\Gamma)^{3/2}}\right]^{-1} \quad , \tag{9}$$

so that the energy equation takes the form

$$\frac{d\Gamma}{d\tau} = \mathcal{E}^2\left[\left(\frac{\Omega_c}{\Omega_s}\right)^2 (2\Gamma)^{3/2} + \frac{1}{(2\Gamma)^{3/2}}\right]^{-1} - \frac{\varepsilon}{(2\Gamma)^{1/2}} \quad . \tag{10}$$

78

If allowed by initial conditions and the electric-field strength, the energy will asymptotically approach a constant value given by $d\Gamma/dt = 0$, or

$$\mathcal{E}^2 = \varepsilon\left[\left(\frac{\Omega_c}{\Omega_s}\right)^2 (2\Gamma) + \frac{1}{(2\Gamma)^2}\right]. \tag{11}$$

The minimum electric field $\mathcal{E}_c$ that permits the energy to approach a constant, nonzero value is determined from $d\mathcal{E}^2/d\Gamma = 0$, with the result

$$\Gamma_c = \left(2\frac{\Omega_c}{\Omega_s}\right)^{-2/3} \quad ; \quad \mathcal{E}_c^2 = \frac{3\varepsilon}{2^{2/3}}\left(\frac{\Omega_c}{\Omega_s}\right)^{4/3} . \tag{12}$$

Normalizing the energy and electric field to the Eq. (12) values puts Eq. (11) in the form

$$Y^2 = \frac{2G}{3} + \frac{1}{3G^2} \tag{13}$$

where $G = \Gamma/\Gamma_c$ and $Y = \mathcal{E}/\mathcal{E}_c$.

Equation (13) is plotted in Fig. 1. Examination of Eq. (10) shows that a nonthermal-electron fluid in a given electric field with initial average energy below the lower branch of
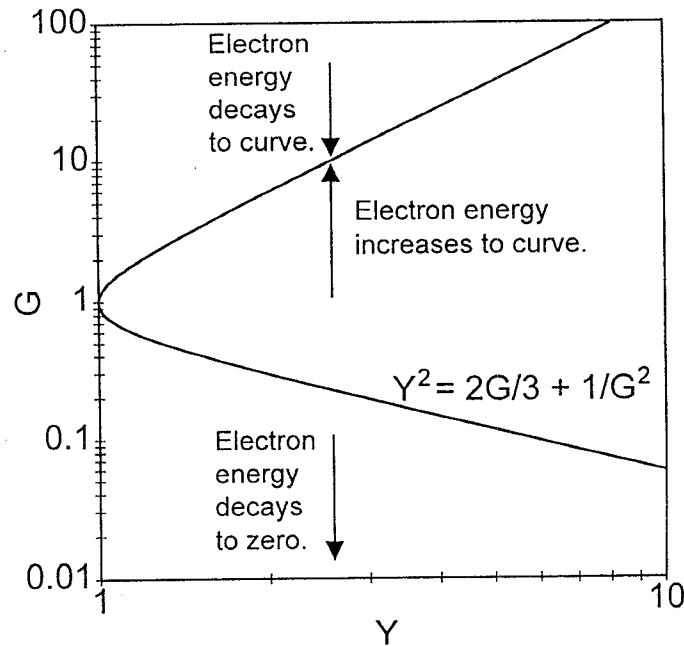
Figure 1. Final electron energy as a function of electric field normalized so as to remove density and magnetic field dependencies.

the curve will lose energy due to the dominance of collisions with the plasma until it merges with the background electron population. Electrons with energy between the two branches will gain energy through scattering collisions along the electric field and asymptotically approach the upper branch. Electrons with initial energy above the upper branch have insufficient scattering collisions to cross the magnetic field before they loose energy, and asymptotically approach the upper branch from above.

That the nonthermal-electron fluid evolution relaxes to the quasistatic behavior in a time short compared to the energy-relaxation time is demonstrated in Figs. 2 and 3 where the solutions of Eqs. (6) - (8) are compared with those of Eqs. (9) and (10) for $(\Omega_c / \Omega_s) = 1000$, $Y = 2$, initial energy $\Gamma(0) = \Gamma_c = 6.3 \times 10^{-3}$, $\beta_x(0) = 0$, and $\beta_z(0) = (2\Gamma_c)^{1/2} = 0.112$. These initial conditions correspond to the extreme case where all electrons move in the z-direction. Figure 2 compares the early-time evolution of fluid velocity using the fully time-dependent (TD) and the quasistatic (QS) models. Initial values are seen to relax to the QS variations in a time $0.01\Omega_s^{-1}$, or about $4v_s^{-1}$ for the average electron energy during this period. Figure 3 compares the corresponding variations in Γ over a somewhat longer period. Following the short-term transient associated with initial conditions, the two models converge rapidly. The
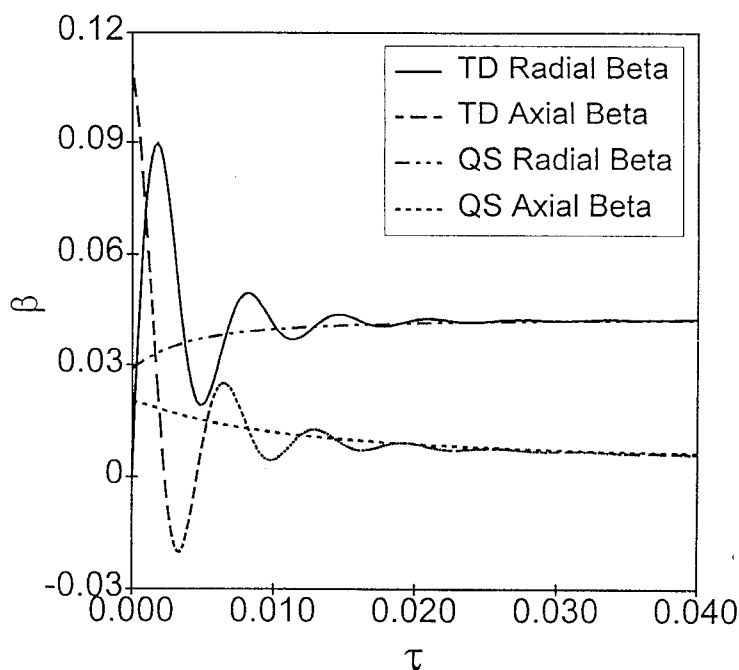
Figure 2.   Time variation of radial and axial electron fluid velocities comparing the full time-dependent and quasistatic models. The case shown is for $Y = 2$, $G(0) = 1$, and $(\Omega_c / \Omega_s) = 1000$.
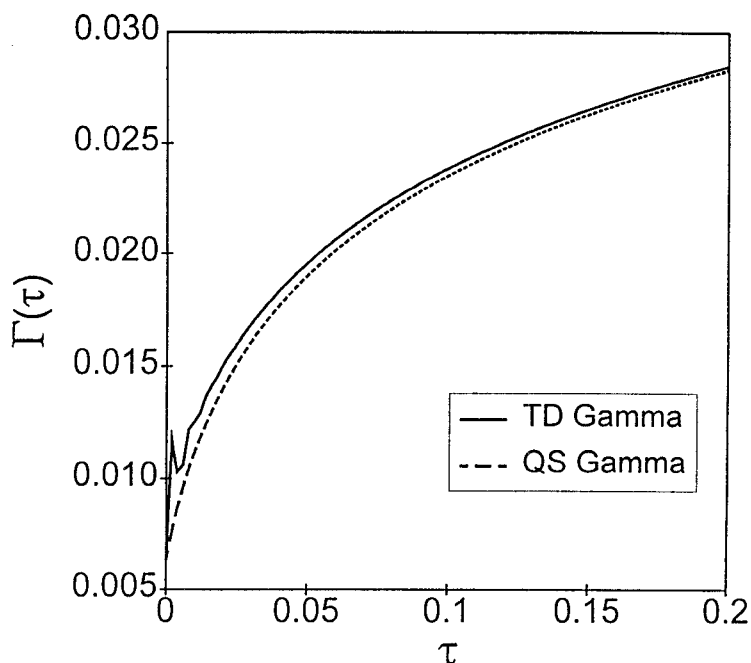
Figure 3. Time variation of electron energy comparing the time-dependent and quasistatic models for the conditions of Fig. 2.

time $\tau = 0.2$, at which the two models agree to a fraction of 1%, corresponds to about $0.5v_e^{-1}$ for the average electron energy during the period. On the longer time scale over which the energy asymptotes, the two models are indistinguishable.

The long-term quasistatic variation in energy is summarized in Fig. 4 for $(\Omega_c / \Omega_s) = 1000$, $Y = 2$, and a variety of initial energies. For initial energy values below the lower branch of Fig. 2, the energy rapidly decays monotonically to zero. For initial energies above the lower branch, the energy asymptotes to the upper branch on a time scale that increases with initial energy. Thus, the behavior summarized by Fig. 1 is demonstrated and Eqs. (12) and (13) are sufficient to characterize nonthermal-electron energy gain for cases of interest.

IPROP Calculations

The 3-dimensional electromagnetic IPROP code[2] has been modified to include a Monte Carlo model of a highly-ionized, high-atomic-number plasma. Typically, the code splits the plasma electron distribution into a thermal component (treated with fluid equations) and a high-energy, nonthermal component (treated as macro-particles interacting with an ambient ionized gas). To perform electron swarm calculations for the plasmas of interest here, all electrons are treated as macroparticles. These macroparticles undergo both elastic and inelastic collisions with plasma ions. Due to the large number of small-angle collisions,
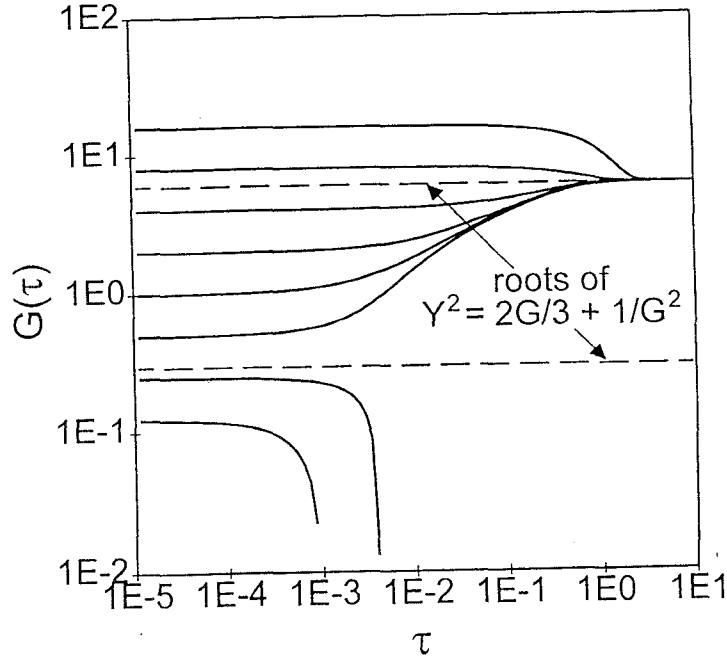
Figure 4.   Quasistatic variation of electron energy with time for $Y = 2$, $(\Omega_c / \Omega_s) = 1000$, and various initial energy values.

elastic scattering of electrons by plasma ions is separated into large-angle and small-angle components. A large-angle-scattering collision is treated as a single event with a probability of unity for each time step. This is accomplished by choosing the cutoff angle such that the integral of the Rutherford-scattering probability from that angle χ_c to π is unity. The Rutherford differential cross section is then sampled to determine the scattering angle. For $\chi < \chi_c$, scattering is treated with the Rossi-Greisen multiple scattering formalism[3] where scattering angles from a Gaussian distribution have a $1/e$ fall-off angle described in Hughes and Godfrey.[4] For a given electron traveling a distance ζ, the distribution function for scattering angles χ is given by,

$$f(\chi,\varsigma) = exp\left(-\frac{\chi^2}{\delta\chi^2\varsigma} \right) ,$$ (14)

where,

$$\delta\chi^2 = 2\pi n_i \sigma(\chi)\chi^4 ln\left(\frac{\chi_c}{\chi_m} \right) ,$$ (15)

82

and σ is the Rutherford scattering cross section. The minimum scattering angle from the Thomas-Fermi atomic model is[5] $\chi_m = \lambda / 2\pi a$ where λ is the deBroglie wavelength and a is the atomic radius. The large and small scattering angles are added in quadrature and then used to modify the electron velocity.

The electron energy loss rate used in IPROP calculations is determined from a simple electron-drag term similar to the right-hand-side of Eq. (2) with the electron momentum loss due to slowing down taken parallel to the electron velocity. Because it is assumed that energetic electrons interact with only cold electrons (either bound or free), this method of incorporating energy loss is only accurate for the case where runaway electrons represent a small fraction of the total.

The swarm simulations consist of pushing plasma electron velocities in the high-atomic-number plasma with embedded, crossed spatially and temporally uniform electric and magnetic fields. The IPROP electro-magnetic field algorithm is not used so as to more closely follow the above fluid calculations. Time steps are chosen to accurately model electrons with energies down to $0.1T_e$. In the results presented here, a background electron temperature of 200 eV is chosen. The simulations are carried out with field quantities and time normalized to ν_{s0}, the momentum-transfer frequency corresponding to a 300-eV $(3kT_e / 2)$ electron. Results presented here renormalize the these quantities to the forms employed in the fluid analysis for easy comparison. Calculations for $\Omega_c / \Omega_s = 3730$, corresponding to a low-mass Saturn load, are discussed.

Figure 5 shows the initial, $T_e = 200$ eV electron macroparticle distribution and the corresponding evolved distributions for three electric field values given by Y = 1.5, 4.1, and 9.4. The evolved distributions show zero-energy (within the energy resolution of the code) and high-energy, nonthermal components separated by an energy gap containing no electrons. This behavior mimics Figs. 1 and 4 in that electrons with low initial energies quickly loose energy to the background, while higher-initial-energy electrons with reduced stopping power can gain energy by scattering along the electric field. The highest electron energies scale with the electric field and are consistent with the corresponding fluid-model values of 4, 33, and 177 keV from Eqs. (12) and (13).

In order to compare the time variation of IPROP results with the fluid model, the nonthermal-electron mean energy <K> is determined from the distribution functions $f_i(K_i, t)$ exemplified by Fig. 5 using

$$< K > \; = \; \sum_{K_i=100}^{\infty} f_i K_i \; \bigg/ \; \sum_{K_i=100}^{\infty} f_i \; . \tag{16}$$

The 100-eV lower limit is arbitrary and is chosen to eliminate contributions from the zero-energy group and count all contributions from the "nonthermal" group. The variations of <K> with time are shown in Fig. 6 for $\Omega_c / \Omega_s = 3730$ and Y = 1.1, 3.0, and 6.8, where the IPROP calculations are compared to the corresponding quasistatic solutions of Eq. (10) for
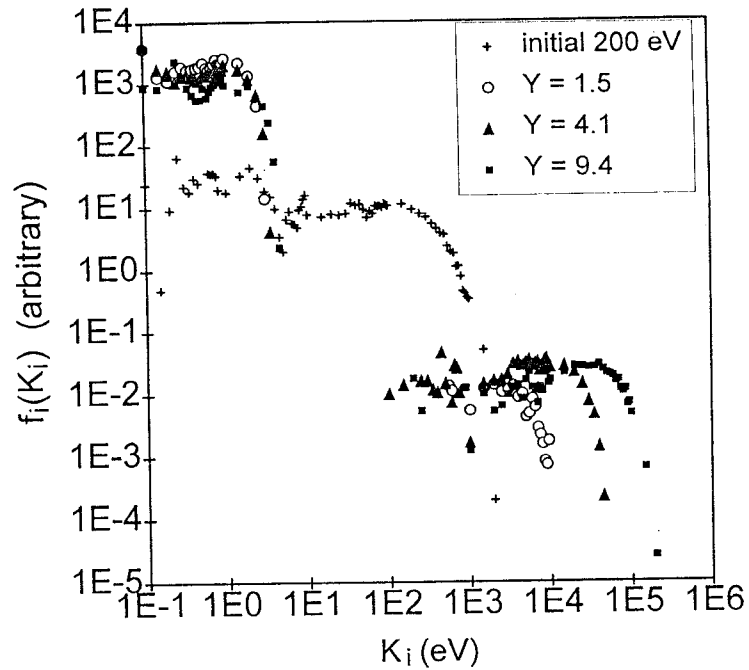
Figure 5. The initial $T_e = 200$ eV electron macroparticle distribution used in IPROP calculations and the resulting evolved distributions for three electric field values.
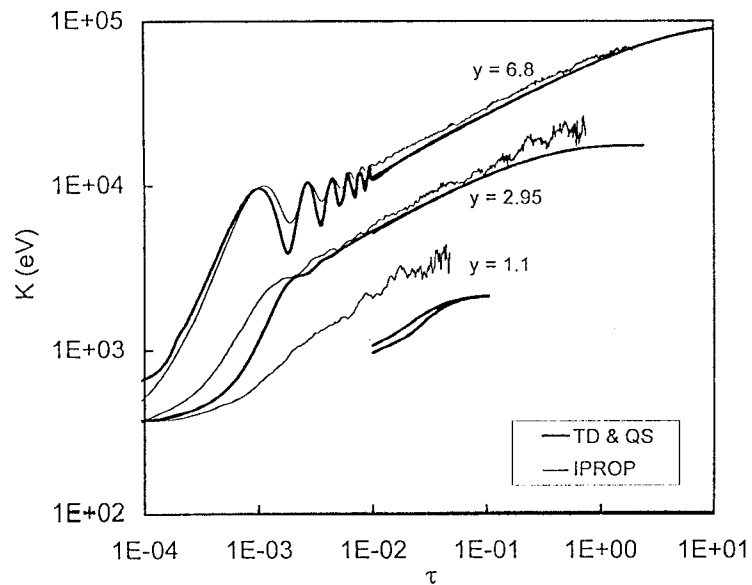
Figure 6. The variations of mean electron energy averaged over IPROP nonthermal distributions with time for $\Omega_c / \Omega_s = 3730$ and three electric field values. Corresponding predictions from the time-dependent (TD) and quasistatic (QS) fluid models are shown for comparison.

late times and the time-dependent fluid solutions from Eqs. (6) - (8) at early times. For the fluid models, an initial mean electron energy of 300 eV ($3kT_e/2$) has been chosen for the two larger electric field values. A higher initial energy was required for $Y = 1.1$ in order to exceed the minimum energy specified by the lower root of Eq. (13). Good agreement between IPROP and the fluid models is seen for the two larger electric field values. Lack of agreement for the electric field close to E_c can be traced to sensitivity of this case on electron energy distributions, since the evolved IPROP distributions are different from those assumed to truncate the fluid-model moment equations.[1]

The above results give confidence that the fluid-model scaling summarized by Eqs. (12) and (13) represents a reasonable predictor of crossed-field energy gain of electrons in high-atomic-number z-pinch plasmas provided that the electric field is substantially above E_c. Equation (13) shows that for $Y \geq 1.2$, the lower and upper branches of the energy curve are well represented by

$$\Gamma_1 = \frac{1}{3^{1/2}2^{2/3}}\left(\frac{\Omega_s}{\Omega_c}\right)^{2/3}\frac{1}{Y} \quad , \tag{17}$$

$$\Gamma_2 = \frac{3}{2^{4/3}}\left(\frac{\Omega_s}{\Omega_c}\right)^{2/3}Y^2 \quad . \tag{18}$$

Electrons with initial energies greater than Γ_1 will be accelerated to a final energy Γ_2. Those with energies less than Γ_1 will decay in energy to the thermal background energy

Substituting numerical values into the definition of F and using Eq. (12) for F_c leads to

$$E_c(V/cm) = 3.23\times10^{-5}\varepsilon^{1/2}\Omega_c^{2/3}\Omega_s^{1/3} \quad , \tag{19}$$

which, when substituted into Eq. (18), results in

$$\Gamma_2 = \frac{1.14\times10^9 E^2(V/cm)}{\varepsilon\Omega_c^2} \quad . \tag{20}$$

Identifying K_0 with $mc^2\Gamma_1$ and K_f with $mc^2\Gamma_2$ yields Eqs. (10) - (12) in Section III.

References

1. D. Mosher, *Phys. Fluids* **18**, 846 (1975).

2. D. R. Welch, C. L. Olson and T. W. L. Sanford, *Phys. Plasmas* **1**, 768 (1994).

3. B. Rossi and K. Greisen, *Rev. Mod. Phys.* **13**,240 (1941).

4. T. P. Hughes and B. B. Godfrey, *Phys. Fluids* **27**,1531(1984).

5. H. A. Bethe, *Phys. Rev.* **89**, 1256 (1953).

Distribution

3   University of New Mexico
Dept. of Chemistry & Nuclear Eng.
Attn: Prof. G. Cooper
       Prof. S. Humphries
       Prof. N. F. Roderick
Albuquerque, NM 87131

2   Ktech Corp.
Attn: T. Smith
       T. Roemer
901 Pennsylvania NE
Albuquerque, NM 87110

5   Los Alamos National Laboratory
Attn: R. J. Macek
       R. Stringfield
       H. A. Thiessen
       R. Fehl
       D. L. Peterson
P. O. Box 1663
Los Alamos, NM 87545

1   W. J. Schafer Assoc., Inc.
Attn: D. C. Straw
2000 Randolph Road SE, Suite 205
Albuquerque, NM 87106

2   Mission Research Corporation
Attn: D. R. Welch
       K. Struve
1720 Randolph Road SE
Albuquerque, NM 87106

1   North Star Research Corp.
Attn: R. J. Adler
5555 Zuni SE, Suite 345
Albuquerque, NM 87108

2   Titan Industries
Attn: R. B. Miller
       J. Smith
P. O. Box 9254
Albuquerque, NM 87119

5   Fermilab
Attn: Prof. L. M. Lederman,
       Director Emeritus
       J. H. Christenson
       H. B. Jensen
       T. E. Nash
       M. Month
P. O. Box 500
Batavia, IL 60510

1   University of California Davis
Attn: Prof. John deGroot
Department of Applied Science
228 Walker Hall
Davis, CA 95616

7   Harry Diamond Laboratories
Aurora Facility
Attn: J. Corrigan, Director
       M. Bushell
       R. Fleetwood
       K. G. Kerris
       J. McGarrity
       G. Merkel
       M. Smith
2800 Powder Mill Road
Adelphi, MD 20783

1   Center for Radiation Research
Attn: S. M. Seltzer
National Bureau of Standards
Gaithersburg, MD 20899

Distribution (continued)

23	Naval Research Laboratory Attn: G. Cooperstein D. Hinshelwood D. Mosher (10 copies) J. M. Neri P. Ottinger F. C. Young R. Commisso J. Davis K. G. Whitney J. P. Apruzese P. E. Pulsifer J. L. Giuliani W. Thornhill Washington, DC 20375

1   Stanford Linear Accelerator Center
Attn: W. R. Nelson
P. O. Box 4349
Stanford, CA 94305

1   Air Force Institute of Technology
Dept. of Engineering Physics
Attn: Prof. D. E. Beller
Wright-Patterson AFB, OH
45433-6583

1   Auburn University
Office of the Vice President for
Research
Attn: Prof. A. K. Hyder
Associate Vice President
202 Samford Hall
Auburn, AL 36849-5112

1   Columbia University
Physics Department
Attn: Prof. W. Lee
538 W. 120 Street
New York, NY 10027

2   Cornell University
Laboratory of Plasma Sciences
Attn: Prof. J. B. Greenly
Prof. D. A. Hammer
369 Upson Hall
Ithaca, NY 14853-7501

1   Massachusetts Institute of
Technology
Plasma Fusion Center
Attn: Prof. R. D. Petrasso
167 Albany St.
Cambridge, MA 01239

1   George Washington University
Department of Physics
Attn: Prof. B. L. Berman
211 Samson Hall
Washington, DC 20052

1   New York University
Physics Department
Attn: Prof. J. Sculli
4 Washington Place
New York, NY 10003

2   University of Maryland
Laboratory for Plasma and
Fusion Energy Studies
Attn: Prof. Moon-Jhong Rhee
Prof. M. Reiser
College Park, MD 20742

1   Imperial College
Blackett Laboratory
Attn: Prof. M. Haines
London SW7 2BZ
ENGLAND

Distribution (continued)

2	Berkeley Research Associates		M. Tabak
	Attn: N. R. Pereira		J. H. Hammer
	J. Golden		J. L. Eddleman
	P. O. Box 852		G. B. Zimmerman
	Springfield, VA 22150		R. S. Thoe
			J. Emig
1	Mission Research Corporation		C. Bruns
	Attn: V. A. J. van Lint		J. Hernandez
	P. O. Drawer 719		P. O. Box 808
	Santa Barbara, CA 03102		Livermore, CA 94550
6	Physics International Co.	6	Atomic Weapons Research
	Attn: H. Helava		Establishment
	J. Creedon		Attn: M. Goodman
	C. Gilman		N. Fenner
	Sik-Lam Wong		M. Gunerson
	J. C. Riordan		B. Harris
	P. Sincerny		J. C. Martin
	2700 Merced Street		G. Wilson
	San Leandro, CA 94577		Aldermaston, Reading RG7 4PR
			Berkshire
4	Pulse Science Inc.		ENGLAND
	Attn: V. Bailey		
	I. Smith	1	Culham Laboratory
	J. Fockler		Culham Lightning Studies Unit
	P. Spence		Attn: C. J. Hardwick
	600 McCormick St.		Abingdon, Oxfordshire OX14 3DB
	San Leandro, CA 94577		ENGLAND
3	Science Applications, Inc.	3	Rutherford Appleton Laboratory
	Attn: A. A. Mondelli		Attn: T. G. Walker, Director
	D. Bacon		T. Broome
	A. Manofsky		C. Damerell
	1710 Goodridge Drive		Chilton, Didcot
	P. O. Box 1303		Oxon. OX11 OQx
	McLean, VA 22101		ENGLAND
12	Lawrence Livermore National	1	University des Sciences et
	Laboratory		Techniques du Languedoc
	Attn: P. T.Springer		Centre d'Elecronique de Montpellier
	A. Toor		Attn: Prof. J. Gasiot
	S. Maxon		Place E. Battaillon
	M. D. Rosen		F-34 060 Montpellier Cedex
			FRANCE

Distribution (continued)

1			Weizmann Institute	1	MS	1170	G. A. Zawadzkas, 9302
			Department of Nuclear Physics	1	MS	1155	W. Beezhold, 9303
			Attn: Y. Maron	1	MS	1165	P. S. Raglin, 9304
			Rehovot 76100 Israel	1	MS	1170	P. Nelson, 9305
				1	MS	1178	J. J. Ramirez, 9310
4			Kernforshungszentrum Karlsruhe	1	MS	1159	M. A. Hedemann, 9311
			Gmbh.	1	MS	1159	G. J. Lockwood, 9311
			Attn: W. Bauer	1	MS	1160	K. Gilbert, 9312
			H. Bluhm	1	MS	1160	J. W. Schwarz, 9312
			P. Hoppe	1	MS	1153	M. T. Buttram, 9323
			H. U. Karow	1	MS	1179	W. P. Ballard, 9341
			Postfach 3640, D-7500 Karlsruhe 1	1	MS	1179	D. E. Beutler, 9341
			FEDERAL REPUBLIC OF	1	MS	1179	R. S. Klingler, 9341
			GERMANY	1	MS	1179	N. E. Counts, 9341
				1	MS	1179	R. E. Craven, 9341
6			C. E. R. N.	1	MS	1179	J. A. Halbleib, 9341
			CH-1211	1	MS	1179	R. P. Kensek, 9341
			Attn: W. Blum	1	MS	1179	J. R. Lee, 9341
			V. Chabaud	1	MS	1179	L. J. Lorence, 9341
			G. Jarlskog	1	MS	1179	T. F. Wrobel, 9341
			G. Lutz	1	MS	1106	A. W. Sharpe, 9342
			W. Manner	1	MS	1106	R. Pepping, 9342
			P. Weilhammer	1	MS	1106	B. Peyton, 9342
			Geneva 23	1	MS	1106	P. Reilly, 9342
			SWITZERLAND	1	MS	1106	R. Broyles, 9342
				1	MS	1106	B. Henderson, 9342
1	MS	0321	E. H. Barsis, 1400	1	MS	1166	G. J. Scrivner, 9352
1	MS	1188	F. McNamara, 1815	1	MS	1190	D. L. Cook, 9500
1	MS	0952	D. J. Miller, 2161	1	MS	1195	J. P. Quintenz, 9502
1	MS	1180	J. P. VanDevender, 4700	1	MS	1181	K. R. Prestwich, 9503
1	MS	0463	R. L. Hagengruber, 5000	1	MS	1193	T. H. Martin, 9511
1	MS	0479	L. M. Choate, 5151	1	MS	1178	R. Hamil, 9512
1	MS	1393	D. L. Johnson, 5209	1	MS	1178	J. P. Corley, 9512
1	MS	0457	R. J. Eagan, 5600	1	MS	1178	S. Drennan, 9512
1	MS	0458	J. S. Rottler, 5607	1	MS	1182	B. N. Turman, 9521
1	MS	1143	J. K. Rice, 6500	1	MS	1193	J. E. Maenchen, 9531
1	MS	1141	T. R. Schmidt, 6502	1	MS	1193	M. T. Crawford, 9531
1	MS	1145	R. J. Lipinski, 6514	1	MS	1193	M. E. Cuneo, 9531
1	MS	1145	R. L. Coats, 6514	1	MS	1193	W. E. Fowler, 9531
1	MS	1183	K. W. Hanks, 6911	1	MS	1193	D. L. Hanson, 9531
1	MS	0151	G. Yonas, 9000	1	MS	1193	D. J. Johnson, 9531
1	MS	1165	J. E. Powell, 9300	1	MS	1193	M. G. Mazarakis, 9531
1	MS	1158	J. H. Renken, 9301	1	MS	1193	P. R. Menge, 9531

Distribution (continued)

1	MS	1193	R. C. Mock, 9531		1	MS	1196	M. Derzon, 9577
1	MS	1193	T. J. Renk, 9531		1	MS	1196	G. Chandler, 9577
1	MS	1193	D. C. Rovang, 9531		1	MS	1196	D. L. Fehl, 9577
16	MS	1193	T. W. L. Sanford, 9531		1	MS	1196	W. A. Stygar, 9577
1	MS	1187	T. A. Mehlhorn, 9533		1	MS	1196	C. L. Ruiz, 9577
1	MS	1187	T. R. Lockner, 9533		1	MS	1431	A.R.C. Westwood, 16000
1	MS	1193	D. D. Bloomquist, 9536		5	MS	0899	Technical Library, 4414
1	MS	1184	J. Boyes, 9539		1	MS	0619	Print Media, 12615
1	MS	1186	C. L. Olson, 9541		2	MS	0100	Document Processing,7613-2
1	MS	1186	J. W. Poukey, 9541					for DOE/OSTI
1	MS	1186	S. E. Rosenthal, 9541		1	MS	9018	CTF, 8523-2

1	MS	1186	M. A. Sweeney, 9541
1	MS	1186	B. D. Marder, 9541
1	MS	1186	D. B. Seidel, 9542
1	MS	1187	G. A. Allshouse, 9571
1	MS	1187	M. K. Matzen, 9571
1	MS	1187	D. R. Humphreys, 9571
1	MS	1187	E. McGuire, 9571
1	MS	1187	R. Olson, 9571
1	MS	1187	M. Douglas, 9571
1	MS	1194	D. H. McDaniel, 9573
1	MS	1194	C. Deeney, 9573
1	MS	1194	D. Zagar, 9573
1	MS	1194	C. W. Mendel, 9573
1	MS	1194	S. M. Cameron, 9573
1	MS	1194	J. T. Crow, 9573
1	MS	1194	W. Moore, 9573
1	MS	1194	T. Nash, 9573
1	MS	1194	J. Porter, 9573
1	MS	1194	M. Savage, 9573
1	MS	1194	J. Seamen, 9573
1	MS	1194	R. B. Spielman, 9573
1	MS	1194	S. Breeze, 9573
1	MS	1194	T. Gilliland, 9573
1	MS	1194	D. Jobe, 9573
1	MS	1194	J. McGurn, 9573
1	MS	1194	L. Ruggles, 9573
1	MS	1194	D. Sparks, 9573
1	MS	1194	K. Struve, 9573
1	MS	1194	M. Vargas, 9573
1	MS	1194	K. Ward, 9573
1	MS	1196	R. J. Leeper, 9577
1	MS	1196	T. Wagoner, 9577